H I Gas Cycles and Lyman Continuum Optical Depth in Low-Redshift Starbursts

by

Anne Elizabeth Jaskot

A dissertation submitted in partial fulfillment
of the requirements for the degree of
Doctor of Philosophy
(Astronomy and Astrophysics)
in The University of Michigan
2014

Doctoral Committee:

Professor Sally Oey, Chair
Associate Professor Eric F. Bell
Professor August E. Evrard
Professor Lee W. Hartmann
Professor John J. Salzer, Indiana University

ACKNOWLEDGMENTS

I am incredibly grateful to the many people who have provided me with support, guidance, and friendship. First and foremost, I would like to thank Sally Oey, who has been a valued mentor and teacher. She truly takes her job as advisor seriously, and in addition to improving my research skills, she has taught me how to be a better writer, reviewer, educator, and leader. I thank Sally for challenging me; by not giving me the answers, she taught me to find them on my own and has helped me grow as an independent researcher. She has made research fun, through her contagious excitement and her openness to letting me investigate the questions that interest me. While aiding my growth as a researcher, Sally has also encouraged me to pursue my interest in teaching. In particular, she gave me the fantastic opportunity to accompany her as teaching assistant for an off-campus class in Arizona, where I learned more than I taught. Finally, I thank Sally for always being there for me when I needed reassurance and for her generosity and hospitality towards all of us in the FANG group.

My dissertation committee members, Eric Bell, Gus Evrard, Lee Hartmann, and John Salzer, have been instrumental in shaping my research, and I thank them for their advice, encouragement, and insight. I am particularly grateful to John for letting me join the ALFALFA-Hα team and sharing his data, and I thank Eric for numerous helpful conversations and suggestions that have given my research direction. The ALFALFA team have also been a great resource, and I particularly thank Martha Haynes and Angie Van Sistine for getting me up to speed, answering my questions,

and providing excellent feedback.

I thank all of the past and present members of the FANG research group for giving me new perspectives and ideas, flagging useful papers, and providing help and advice. I especially thank my fellow grad students Jordan Zastrow and Joel Lamb for their friendship, leadership, and grammar lessons, and I thank Eric Pellegrini for teaching me to use CLOUDY. Thank you to Jesse Golden-Marx and Jesus Lopez-Hernandez for patiently reading many thesis drafts.

I appreciate the work of the department's administrative staff, especially Brian Cox and Jan Malaikal, who ensured that my years at Michigan went smoothly. They always greeted me with a smile, were quick to respond to any question, and made complications disappear. Roy Bonser provided crucial computer support, and I am exceedingly grateful to him for salvaging my data from a now defunct computer.

Prior to graduate school, many teachers and researchers inspired me and encouraged me in my astronomy career. Karen Kwitter, Jay Pasachoff, Steve Souza, Arsen Hajian, Lee Ann Hennig, and Kevin Bundy introduced me to astronomy, graciously shared their expertise, provided me with research opportunities, and were patient mentors. I especially thank Arsen for convincing me to make the very wise decision to go to the University of Michigan the day before the response deadline. I am also grateful to Eric Richardson, whose writing lessons have been on my mind throughout this dissertation.

To all of my friends in Ann Arbor, thank you for making the past five years so enjoyable. I will miss all of the Astrograds, who are some of the friendliest people I've ever met and one of the main reasons I came to Michigan. You made grad school laughter-filled, even when it was stressful. To Ilse, my office mate throughout grad school, thank you for accompanying me on coffee expeditions, listening when I need to talk, distracting me even when I'm hyper-focused, making me laugh, accidentally slingshotting the toy monkey out of the tenth floor window, and sharing the secrets

of your scrabble wizardry (wizardry=24 points). To Colin, our office's grinding salon resident, thank you for your sense of humor, for your brilliant almost-scrabble words, for your aviation updates, and for finally identifying the location of the mystery water tower, which would have bothered me for years. To Jeb, thank you for your outgoing nature, for instituting Bread Tuesdays, for organizing department outings, and for introducing me to the indescribable weirdness of the short film on grasses. Outside of the department, I thank, in no particular order, Aron, Jessie, Julie, Matt, Chad, Aaron, Elizabeth G., Elizabeth S., Andrea, and Bryan for sharing good food and adventures. I am also grateful to the welcoming congregation at Trinity Lutheran, especially Lori, Sara, and the Uncorked group, for providing support when I needed it and creating a community that felt like home.

The love of my friends and family has encouraged me, and I am lucky to have so many people in my life cheering me on. I thank my family members and the friends who have become like family for welcoming me into their homes, sending kind words my way, and celebrating the good times with me. In particular, I thank Kitt for reading my superbubble paper in its entirety, for bragging about me to all her friends, and for braving Michigan's cold to visit me. Thank you for your patience with my hectic schedule for always being willing to talk. I also thank my grandparents; to a large extent, I owe my astronomy career to them. To Granddad, thank you for sharing your interest in astronomy with me and forwarding your copies of *Astronomy* magazine to me throughout my childhood. I thank Opa for supporting me through college and showing me how to live life to the fullest. To my parents, I am thankful that you encouraged all my early interests, even when you didn't share them. You have instilled in me a love of learning, and I admire and strive to emulate your curiosity and fascination with the world. Thank you for helping me through stressful times and helping me keep the right perspective on life. Last but not least, I thank my husband, Alex, who has been my constant companion through all my years at

Michigan, my belayer, and the unofficial third member of my office. He is also the only reason I had food in the weeks leading up to the defense. Alex, thank you for your constant love, for believing in me, and for keeping me calm. You instinctively know when I need support and remind me of what really matters. I thank God for blessing me with friends and family, for sustaining me, and for creating a wondrous universe to study.

I acknowledge support from an NSF Graduate Research Fellowship. Chapter 2 of this thesis is based on work to be published in *The Astrophysical Journal* (Jaskot et. al. in preparation). This research was supported by NSF grant AST-0823801, by The College of Arts and Sciences at Indiana University, and by NOAO through their Surveys program. It was also supported by fellowships from the Indiana Space Grant Consortium to Angie Van Sistine. In addition, the ALFALFA team at Cornell University is supported by NSF grant AST-1100968 and by the Brinson Foundation. Chapter 3 is published in *The Astrophysical Journal*, Vol. 766, page 91 (Jaskot & Oey, 2013) and is reproduced here with permission and minor modifications. NSF grant AST-0806476 to M. S. Oey provided additional support for this research. Chapter 4 is published in *The Astrophysical Journal Letters*, Vol. 791, page L19 (Jaskot & Oey, 2014), and is reproduced here with permission and minor modifications. Support for this research was provided by NASA through grant HST GO-13293 from the Space Telescope Science Institute, which is operated by the Association of Universities for Research in Astronomy, Inc., under NASA contract NAS 5-26555. I also acknowledge travel grants from Rackham Graduate School, which enabled me to present this thesis work at conferences.

TABLE OF CONTENTS

LIST OF FIGURES

Figure

ABSTRACT

Neutral gas both fuels star formation and determines the propagation of ionizing photons. In this work, we reveal the interactions between H I, star formation, and radiative feedback in two samples of low-redshift starbursts. Using the ALFALFA-Hα sample, we present the first comparison of starbursts and non-starbursts within a statistically uniform, H I-selected sample. The moderate H I gas fractions of the starbursts relative to non-starbursts indicate efficient H I to H_2 conversion and show that the H I supply is largely unaffected by ionizing radiation. Mergers may trigger the more massive starbursts, while the absence of obvious kinematical disturbances in dwarf starbursts may indicate periodic starburst activity, triggered by cycles of gas expulsion and re-accretion. While the ALFALFA-Hα galaxies demonstrate that starbursts may maintain large H I reservoirs, the more powerful starbursts in the Green Pea (GP) galaxies illustrate the effects of extreme radiative feedback on neutral gas. To investigate whether the enormous [O III]/[O II] ratios in the most extreme GPs indicate LyC escape, we use photoionization modeling to constrain their ionizing sources and optical depths. Radiation from Wolf-Rayet stars or unusually hot O stars reproduces the observed [O III]/[O II] ratios, but no clear signatures of these stars are present. The GP spectra do suggest the presence of shocks, however, and accounting for shock emission necessitates a low optical depth. We therefore suggest that the GPs may be a new class of low-redshift LyC Emitters (LCEs), and we evaluate this scenario using *Hubble Space Telescope* COS spectra of four GPs. With these spectra, we develop a simple physical picture of the neutral gas optical depth and geometry that explains the previously enigmatic link between Lyα, Si II, and Si II* lines observed

in high-redshift Lyα Emitters. Two GPs are likely optically thin along the line of sight, and their strong, narrow Lyα emission, weak C II absorption, and clear C II* emission may be characteristic of LCE spectra. We also note a striking similarity of the Lyα emission in these GPs to Balmer line emission from stellar ejecta, which further supports a low column density scenario. From our analysis of the ALFALFA-Hα and GP samples, we suggest that particular burst ages, low halo masses, and extreme, concentrated starbursts may facilitate LyC escape.

CHAPTER I

Introduction

1.1 H I and Galaxy Evolution

Neutral, atomic hydrogen (H I) plays an integral role in the gas and energy cycles of star-forming galaxies by both providing the fuel for star formation and responding to the resulting stellar feedback. On galaxy-wide scales, the total surface density of atomic and molecular gas and the surface density of star formation scale almost linearly, a relation known as the Kennicutt-Schmidt Law (Schmidt, 1959; Kennicutt, 1989, 1998b). However, recent observations show that the star formation in galaxies correlates most strongly with the local molecular gas content, rather than with H I (e.g., Bigiel et al., 2008; Schruba et al., 2011). While molecular gas (H_2) is the immediate precursor of star formation, H I cooling sets a galaxy's molecular gas supply, and H I content therefore indicates the potential for future star formation. H_2 formation requires a sufficiently high column density of H I to shield H_2 molecules from dissociation by the interstellar radiation field (e.g., McKee, 1989; Krumholz et al., 2009). When H I gas reaches this column density threshold, gas cools to form both H_2 and stars (Krumholz et al., 2011). Observations of spiral and dwarf galaxies confirm the existence of a maximum H I column density of $\sim 10\,M_\odot\ pc^{-2}$ (e.g., Wong & Blitz, 2002; Bigiel et al., 2008), although the value of this threshold density may depend on metallicity (e.g., Krumholz et al., 2009; Bolatto et al., 2011). Below the

threshold, H I column density regulates the formation of molecular clouds and thus the star formation rate (SFR), while above the threshold, only molecular gas controls the SFR (Schruba et al., 2011). The formation of molecular clouds from H I must be an ongoing process in galaxies; the 1-2 Gyr molecular gas consumption timescales at low redshift, $z < 2$, (e.g., Kennicutt, 1998b; Daddi et al., 2008; Schruba et al., 2011) indicate that H I must continually replenish the H_2 supply. Flows of H I into and within galaxies and the processes that regulate H I-to-H_2 conversion are therefore key drivers of galactic star formation.

In addition to tracing the fuel of future star formation, a galaxy's H I gas content reflects the effects of stellar feedback. High-energy radiation from newly formed massive stars may create H I through the photodissociation of molecular gas (e.g., Phillips & Huggins, 1981; Allen et al., 1986; Tielens et al., 1993) or destroy H I through photoionization. Expanding, photoionized H II regions surround young massive stars and may trigger future star formation by compressing interstellar gas clouds (e.g., Elmegreen & Lada, 1977; McCray & Kafatos, 1987). In addition to radiative feedback, stellar winds and supernovae inject turbulence and control the spatial distribution of H I gas by blowing hot, low-density bubbles in the interstellar medium (ISM). These feedback mechanisms may maintain an equilibrium between energy injection and energy losses, thereby regulating the SFR. Different mechanisms may dominate in different density regimes, with ultraviolet (UV) heating balancing H I cooling, supernova-driven turbulence balancing gravity, or radiation pressure balancing the weight of the ISM (e.g., Silk, 1997; Parravano & Mantilla, 1991; Thompson et al., 2005; Ostriker et al., 2010; Ostriker & Shetty, 2011). Supernova feedback also alters a galaxy's global H I content by driving neutral gas outflows (e.g., Chevalier & Clegg, 1985; Heckman et al., 1990; Strickland & Stevens, 2000) that may suppress star formation (e.g., Dekel & Silk, 1986; Meurer et al., 1997; Davé et al., 2011b). Resolved observations of dwarf galaxies often reveal large H I holes, where supernova feedback

may have ejected the H I gas (e.g., Sargent et al., 1983; Ott et al., 2001; Cannon et al., 2011). These low-density cavities may facilitate the transport of ionizing photons, allowing radiative feedback from stellar clusters to penetrate to outer regions of galaxies or to escape into the intergalactic medium (IGM; e.g., Clarke & Oey, 2002; Wood et al., 2010). Escaping UV photons from star-forming galaxies may inhibit halo gas cooling, thereby stifling the accretion of additional H I gas (Cantalupo, 2010). Furthermore, at $z > 6$, the escape of Lyman continuum (LyC) radiation from star-forming galaxies into the IGM likely reionized the universe (e.g., Willott et al., 2010; Bouwens et al., 2012). Low-mass starburst galaxies may dominate the ionizing photon input into the IGM during reionization (e.g., Wise & Cen, 2009; Ferrara & Loeb, 2013), but factors such as the star formation efficiency, galaxy structure, and the neutral hydrogen distribution will control LyC escape from an individual galaxy (e.g., Fernandez & Shull, 2011). By fueling star formation and regulating LyC transport, the H I content of galaxies has a considerable effect on the evolution of the IGM.

The complex interplay between H I gas, star formation, and feedback shapes galaxy evolution and may explain the history of star formation in galaxies. Cosmological hydrodynamical simulations predict a decreasing gas accretion rate onto galaxies from the IGM with time due to the expansion of the universe, which may explain the overall decrease in the cosmic SFR since $z = 2$ (e.g., Kereš et al., 2005; van de Voort et al., 2011). In low-mass halos, variable gas accretion rates may account for their higher frequencies of starburst episodes (Lee et al., 2009b). Supernova feedback may also drive episodic star formation in low-mass galaxies by quickly expelling their neutral gas supply following a starburst (e.g., Gerola et al., 1980; Stinson et al., 2007; Lee et al., 2009b). By lowering the efficiency of star formation, feedback may also lead to the accumulation of H I reservoirs and a delay in gas consumption (Hopkins et al., 2013).

Although simulations indicate that H I gas flows may fuel cosmic star formation, direct detections of H I accretion are lacking. Nevertheless, observations suggest that accretion of IGM gas maintains galaxies' H I supplies. The primary observational tracers of H I are Lyα absorption from H I atoms in the ground state and the 21 cm emission line from the ground-state electron spin-flip transition (e.g., Wolfe et al., 1986; Ewen & Purcell, 1951). Lyα absorption of UV emission from a background quasar probes the H I column density of the foreground galaxy, and these absorption studies provide evidence for H I accretion and outflows in both low- and high-redshift galaxies. At $z < 1$, absorbing gas in the circumgalactic medium (CGM) of galaxies shows a bimodal metallicity distribution that likely represents metal-poor inflows and metal-rich outflows (Lehner et al., 2013). The mass density of H I galactic gas in the universe decreases from $z = 4$ to $z = 2$ and remains constant or decreases further from $z = 2$ to $z = 0$ (Prochaska & Wolfe, 2009; Noterdaeme et al., 2009). Feedback or gas consumption may decrease the H I content of galaxies at high redshift, while the fresh accretion of H I appears necessary to balance its consumption at low redshift (Prochaska & Wolfe, 2009; Noterdaeme et al., 2009). Observing accreting filaments directly via 21 cm emission at low redshift is challenging, however. Infalling H I gas may have low column density, and may be difficult to distinguish from minor merger activity (e.g., Sancisi et al., 2008; de Blok et al., 2014). Moran et al. (2012) suggest that a drop in metallicity observed in the outer regions of some spiral galaxies may be caused by the recent accretion of metal-poor gas. Galaxies with an outer metallicity drop have higher total H I masses and inner SFRs, suggesting that the total H I content of galaxies traces recent accretion and that accretion can fuel inner star formation. Observations also point to the role of H I in regulating the metallicity of galaxies, with the balance between metal-poor inflows and metal-rich outflows determining both H I content and galaxy metallicity (Bothwell et al., 2013). Nevertheless, the accumulation of H I, its transport within galaxies to fuel star formation, and the

processes regulating the H I supply in galaxies are still not well understood.

1.2 Starburst Galaxies

Starburst galaxies represent an important regime in which to test our understanding of H I gas cycles and their roles in driving star formation and controlling LyC escape. Weedman et al. (1981) first coined the term "starburst" to describe galaxies with intense nuclear star formation. Different studies employ different observational definitions of starbursts, identifying them as galaxies with high specific SFRs (sSFRs), high SFRs per unit area, or short gas consumption timescales (e.g., Kennicutt & Evans, 2012). In general, starbursts are experiencing a short-lived burst of star formation that dominates their energy output. The high levels of star formation in starbursts are unsustainable; at their current rate of star formation, starbursts will consume their available molecular gas in less than 100 Myr (e.g., Combes et al., 2013; Bauermeister et al., 2013). Due to their high sSFRs and young stellar population ages, starburst galaxies contain large numbers of short-lived massive stars and provide an excellent probe of the effects of stellar feedback. Observations of starburst galaxies reveal powerful outflows, some of which have mass-loss rates of several solar masses per year (e.g., Della Ceca et al., 1999; Strickland & Heckman, 2009).

Perhaps most importantly, while starbursts are rare in the local universe, they may represent a normal mode of star formation at high redshift. The high sSFRs of starburst galaxies, their short inferred star formation timescales, and their clumpy morphologies resemble the properties of star-forming galaxies at $z > 2$ (e.g., Cowie et al., 1995; Dickinson et al., 2003; Stark et al., 2009; Karim et al., 2011; Fumagalli et al., 2012; Wyithe et al., 2014). The SFR density of the universe reaches a maximum near $z = 2$ (e.g., Hopkins & Beacom, 2006; Bouwens et al., 2010), with the star formation in individual halos peaking between $z = 0.5 - 2.5$ (Behroozi et al., 2013). Low-mass galaxies may dominate the universe's star formation at the $z = 2$ peak

(e.g., Alavi et al., 2014), and may form stars in short-duration starburst episodes. Indeed, the fraction of starbursting galaxies appears to increase with both redshift and decreasing galaxy stellar mass (e.g., Fumagalli et al., 2012; Atek et al., 2014). At even higher redshifts, $z > 3$, brief, intense starbursts may be a common mode of galaxy star formation (e.g., Lee et al., 2009b; Stark et al., 2009; de Barros et al., 2014; Wyithe et al., 2014). Furthermore, the spectra of compact, $z = 0$ dwarf starbursts are similar to spectra of galaxies at the time of reionization (e.g., Boone et al., 2007; Smit et al., 2014). Low-redshift starbursts may therefore provide critical insight into the connection between H I content, star formation, and ionizing radiation in high-redshift galaxies.

1.2.1 H I in Starbursts

Few studies address the H I properties of starburst galaxies, and the existing works focus on optically selected samples or observations of individual galaxies. Observations of molecular gas in starbursts show that starbursts may not follow the same relation between gas content and star formation as non-starbursts (Daddi et al., 2010); these differences in star formation efficiency may extend to H I gas as well. Studies of optically selected samples suggest that dwarf galaxies have more scatter in sSFR than in H I content (Bothwell et al., 2009). Some samples indicate that starbursts may have extended H I halos supplying their star formation (e.g., Gordon & Gottesman, 1981), while others show that starbursts may be H I-deficient due to their high ionizing luminosities (Oey et al., 2007). The triggering mechanisms of low-redshift starbursts are also unclear, particularly at the low mass end. While many starbursts appear to be merger-driven (e.g., Larson & Tinsley, 1978; Cui et al., 2001; Luo et al., 2014), gas infall may trigger some low-mass starbursts (e.g., Gordon & Gottesman, 1981; Meier et al., 2002; López-Sánchez et al., 2012b; Verbeke et al., 2014). Merger-driven starbursts may be important contributors to reionization (Muñoz & Loeb,

2011), while accretion-driven star formation may dominate at intermediate redshift (e.g., Kereš et al., 2005). A systematic survey of the H I properties of starbursts is necessary to clarify the role of H I gas in fueling starbursts and reveal the effects of extreme feedback on the H I supply.

1.2.2 LyC Escape from Starbursts

The joint evolution of the H I content and the ionizing photon production rate in starbursts also has important implications for our understanding of radiative feedback in galaxies and its effect on the IGM. One of the main uncertainties in models of reionization is the escape fraction of LyC from star-forming galaxies. Model estimates for the average LyC escape fraction at the epoch of reionization range from 0.01-1 (Fernandez & Shull, 2011). The average LyC escape fraction may evolve with time and may decrease by more than a factor of two over the course of reionization (Mitra et al., 2013). Although no detections of LyC emission exist at $z > 4$, Lyman-break galaxies and Lyα-emitters (LAEs) at $z \approx 3$ have direct detections of LyC (e.g., Steidel et al., 2001; Iwata et al., 2009; Nestor et al., 2013). Unfortunately, possible confusion with low-redshift galaxies along the line of sight make many of these detections suspect (Vanzella et al., 2010, 2012). Observations of LAEs provide additional circumstantial evidence for LyC escape. Strong LAEs are more abundant at high redshift (Zheng et al., 2014) and appear to have lower H I column densities or covering fractions (e.g., Shapley et al., 2003; Hashimoto et al., 2013; Shibuya et al., 2014), due to ionization of their neutral gas or outflows. LyC escape from $z \approx 3$ LAEs is therefore plausible.

In contrast to the successful LyC detections at $z \sim 3$, however, the first searches for LyC emission from low-redshift starburst galaxies found upper limits to the LyC escape fraction of only a few percent (e.g., Leitherer et al., 1995; Heckman et al., 2001). Currently, only two low-redshift starbursts have positive detections of LyC radiation (Leitet et al., 2013). The reason for the low LyC escape fractions in low-

redshift starbursts is unclear. Most low-redshift starbursts may have SFRs too low to fully expel or ionize their H I gas, or LyC radiation may escape through a narrow opening angle that hinders its detection (e.g., Zastrow et al., 2011).

Whether LyC radiation escapes a starburst will depend on the competition between H I inflow and stellar feedback throughout the starburst episode. A large H I supply may power a starburst for a more extended period of time; however, it may also prevent ionizing radiation from escaping. The distribution of H I gas and the balance between H I content and ionization may vary as a starburst progresses or may depend on galaxy properties, such as halo mass, morphology, or star formation efficiency (e.g., Wise & Cen, 2009; Ferrara & Loeb, 2013). To analyze the processes that enhance LyC escape and determine accurate LyC escape fractions from galaxies, we need to identify optically thin starbursts at low redshift. Understanding the H I distribution and optical depth in starbursts is necessary to determine how LyC radiation escapes and whether star-forming galaxies can reionize the universe.

1.3 This Work

Thus, H I cycles and radiative feedback in starbursts are critical to the evolution of galaxies and the reionization of the IGM. In this thesis, we use multiwavelength spectral and imaging observations to investigate how H I gas fuels starburst events, how the H I supply evolves during a starburst, and whether and how LyC radiation escapes low-redshift starbursts. In Chapter 2, we illuminate the relationship between H I content and extreme star formation by comparing the H I properties of starburst and non-starburst galaxies in the H I-selected, volume-limited ALFALFA-Hα survey. We discuss how starburst mass and age affect their H I supply and explore the factors that enhance the star formation efficiencies of starbursts and non-starbursts. In Chapter 3, we investigate whether extreme low-redshift starbursts are optically thin to the LyC and identify a new population of LyC emitter (LCE) candidates. We

analyze the unusual emission-line spectra of the Green Pea (GP) galaxies, rare, low-redshift starbursts whose morphologies, sSFRs, and emission line spectra resemble those of high-redshift galaxies (Cardamone et al., 2009). Through photoionization modeling of the GPs' emission, we constrain the ionizing sources and LyC optical depths in these starbursts and demonstrate that the GPs may be a class of optically thin galaxies. Finally, in Chapter 4, we use UV spectra of four GPs from the *Hubble Space Telescope* to determine the optical depth and geometry of their neutral ISM. We highlight a newfound connection between Lyα emission, low-ionization emission and absorption lines, and H I optical depth and geometry, and we describe a characteristic UV spectral pattern that may identify LCEs at high and low redshift. Our analysis of the H I content and LyC optical depth of low-redshift starbursts offers insight into the processes that may promote or prevent LyC escape.

CHAPTER II

The H I Properties of ALFALFA-Hα Starbursts

2.1 Introduction

Gas inflows and outflows drive galaxy evolution by controlling the raw material from which stars form. The star formation history of the Universe may reflect the history of gas accretion onto dark matter halos (e.g., Kereš et al., 2005; Prochaska & Wolfe, 2009), and observed galaxy scaling relations may likewise trace the history of gas flows. For instance, the observed relations between galaxy stellar masses, star formation rates (SFRs), and metallicities may stem from variations in the efficiency with which galaxies accrete and expel gas (e.g., Dalcanton, 2007; Mannucci et al., 2010; Davé et al., 2011b,a; Lilly et al., 2013).

The connection between gas content and star formation is a well-established result. Individual stars form from dense cores within molecular clouds (e.g., Myers & Benson, 1983; Motte et al., 1998). On kiloparsec scales, a galaxy's SFR surface density, $\Sigma_{\rm SFR}$, increases with H I+H_2 gas surface density, $\Sigma_{\rm H_I+H_2}$, as parameterized by the Kennicutt-Schmidt Law (Kennicutt, 1998b). More recent work shows that $\Sigma_{\rm H_2}$, rather than $\Sigma_{\rm H_I}$, drives the Kennicutt-Schmidt law, even in H I-dominated regimes (Schruba et al., 2011). Above a threshold density of $\sim$10 $M_\odot/pc^2$, H I "saturates"; this column density is sufficient to shield molecular gas from photodissociation. Most gas above this threshold is molecular (e.g., Wong & Blitz, 2002; Bigiel et al., 2008), resulting in

no trend between SFR and H I in this density regime. Below this threshold, however, $\Sigma_{\rm SFR}$ and $\Sigma_{\rm H_I}$ correlate, albeit with a large scatter, due to the relation between $\Sigma_{\rm H_I}$ and $\Sigma_{\rm H_2}$ (Schruba et al., 2011).

Compared to the link between H_2 content and SFR, the relationship between galaxies' H I content and star formation is less straightforward. Galaxies' H I typically extends to much larger radii than the stellar distribution (e.g., Broeils & Rhee, 1997) and may constitute a gas reservoir for fueling future star formation. Accretion of gas from the intergalactic medium may replenish this reservoir, and gas flows may bring H I inward, leading to star formation in the inner regions of galaxies. Prochaska & Wolfe (2009) suggest that galaxies' H I disks exist at a constant, unstable density, with any subsequent accretion leading to the creation of stars and resulting in an SFR that traces the accretion rate. In massive galaxies, the total H I gas fraction correlates with signs of recent accretion, such as an outer metallicity drop, and this accretion appears to power star formation throughout the galaxy disk (Moran et al., 2012). The H I in low-mass galaxies, on the other hand, may not signify recent accretion. Low-mass galaxies tend to be more gas-rich than high-mass galaxies, and H I constitutes the dominant component of their interstellar medium (ISM). The long gas consumption times in such systems may indicate that star formation proceeds inefficiently. Alternatively, Kannappan et al. (2013) argue that star formation cannot keep pace with the rate of gas accretion. The relationship between H I and star formation may also change in dwarf galaxies due to their lower metallicities. At low metallicities and, consequently, low dust content, the formation of a given $\Sigma_{\rm H_2}$ requires a higher H I column density (Krumholz et al., 2009). As a result, the relationship between H I density and H_2 formation differs for low-metallicity galaxies, with galaxies such as the Small Magellanic Cloud exhibiting a higher threshold density for H I saturation (Bolatto et al., 2011).

The advent of large H I surveys capable of resolving individual galaxies has clarified

the connection between H I mass and galaxy properties. In particular, the Arecibo Legacy Fast ALFA (ALFALFA) survey is a blind, volume-limited, 21 cm survey, which covers 7000 deg^2 and has detected ∼30,000 galaxies out to $z = 0.06$ (Giovanelli et al., 2005b,a; Haynes et al., 2011). In conjunction with ALFALFA, the *GALEX* Arecibo SDSS (GASS) survey examines the H I content of massive galaxies ($M_* > 10^{10}$ M$_\odot$) using additional Arecibo observations for galaxies undetected in ALFALFA (Catinella et al., 2010). These surveys have established scaling relations between H I gas fraction and galaxy stellar mass, stellar surface density, color, SFR, and specific SFR (sSFR; e.g., Catinella et al., 2010; Huang et al., 2012). The positive correlations found between H I gas fraction and blue color or sSFR imply a link between galaxies' H I content and their current global star formation.

Starburst galaxies may depart from the typical relations between H I content and star formation, however. The Kennicutt-Schmidt Law differs for starburst galaxies, with starburst galaxies forming stars more efficiently from a given molecular gas mass (Daddi et al., 2010). One possible explanation for this increased efficiency is merger activity (e.g., Young et al., 1986; Sanders et al., 1986; Combes et al., 1994), and many starbursts appear to be interacting systems. If starbursts gain H I gas via major mergers instead of accretion, they may differ from non-starbursts in both their H I gas consumption times and H I gas fractions. In addition, due to their young stellar populations, mechanical and radiative feedback will have a stronger effect on the ISM of starbursts. This feedback may decrease the H I gas fractions of starbursts by driving outflows or ionizing the neutral gas. Oey et al. (2007) suggest the latter scenario as an explanation for the lower H I gas fractions in starburst galaxies in the Survey for Ionization in Neutral Gas Galaxies (SINGG). The SINGG result contrasts with the ALFALFA and GASS trends of higher H I gas fractions in more highly star forming galaxies and may indicate that starbursts do not follow the same H I trends as normal galaxies.

Starburst galaxies present an opportunity to study the relations between neutral gas content, star formation, and feedback in extreme conditions. The H I gas fractions and kinematics of starbursts may reveal the mechanisms for triggering extreme star formation episodes and the impact of feedback on global gas content. Previous studies of H I in starbursts have focused on individual galaxies or optically selected samples (e.g., Yun et al., 1993; Huchtmeier et al., 2007; Oey et al., 2007; López-Sánchez et al., 2012b). To systematically compare H I in starbursts and non-starbursts, we use the fall-sky portion of the ALFALFA-Hα survey. ALFALFA-Hα is a volume-limited subset of the ALFALFA survey consisting of 1555 galaxies with follow-up Hα and R-band imaging (Van Sistine et al., in prep.). With the 565 galaxies in the "fall-sky" ALFALFA-Hα dataset, we investigate the regulation of the H I gas supply throughout the star formation process.

2.2 Data and Methods

2.2.1 The ALFALFA-Hα Survey

The recently-completed ALFALFA survey is a blind, volume-limited, 21 cm survey with Arecibo[1] that covers 7000 deg^2 of sky. The H I-selected ALFALFA-Hα survey consists of all ALFALFA-detected galaxies within two designated areas, a fall-sky region and a spring-sky region (Van Sistine et al., in prep.). The sample only includes galaxies with reliable H I detections (i.e., ALFALFA codes 1 and 2) and with recession velocities $v = 1460 - 7600$ km s^{-1}. These velocities correspond to distances of $\sim$20-100 Mpc, and the sample is volume-limited for $M_{\rm HI} > 10^{9.5}\,{\rm M}_\odot$. H I masses, 21 cm velocity widths, and distances come from the ALFALFA catalog (Haynes et al., 2011). In this work, we consider the complete, fall-sky ALFALFA-Hα sample, which contains

[1]The Arecibo Observatory is operated by SRI International under a cooperative agreement with the National Science Foundation (AST-1100968), and in alliance with Ana G. Méndez-Universidad Metropolitana, and the Universities Space Research Association.

565 galaxies; the full sample will be described in a later work (Van Sistine et al., in prep.). R-band and Hα imaging for the fall-sky ALFALFA-Hα galaxies were obtained with the WIYN[2] 0.9 m and the Kitt Peak National Observatory (KPNO[3]) 2.1 m telescopes between Sept. 2006 and Oct. 2012. The parameters of the ALFALFA-Hα survey, observations, and data reduction are described in detail in Van Sistine et al. (in prep.).

Hα and R-band fluxes were measured for each galaxy individually using aperture photometry; the Hα images were continuum-subtracted prior to flux measurement. 542 galaxies are detected in Hα. To facilitate comparison with the literature, the quoted Hα equivalent widths are an observed quantity and are not corrected for extinction or [N II] emission. For derived parameters, such as SFRs, the Hα fluxes were corrected for Galactic absorption using the Schlegel et al. (1998) extinction maps and for [N II] contamination and internal absorption using the R-band absolute magnitudes (M_R) and scaling relations derived from the KPNO International Spectroscopic Survey (KISS; Salzer et al. 2000, 2005). In § 2.2.4, we compare these extinction corrections to corrections derived from *Wide-field Infrared Survey Explorer* (*WISE*[4]; Wright et al. 2010) photometry. After correcting the Hα emission for extinction, we convert the Hα luminosities to SFRs using the Kennicutt (1998a) calibration:

$$\mathrm{SFR} = 7.9 \times 10^{-42} L(\mathrm{H}\alpha), \tag{2.1}$$

where $L(\mathrm{H}\alpha)$ is the Hα luminosity in $\mathrm{ergs\,s^{-1}}$ and the SFR has units of $\mathrm{M_\odot\ year^{-1}}$.

[2]The WIYN Observatory is a joint facility of the University of Wisconsin-Madison, Indiana University, Yale University, and the National Optical Astronomy Observatory.

[3]The Kitt Peak National Observatory, National Optical Astronomy Observatory, is operated by the Association of Universities for Research in Astronomy (AURA) under cooperative agreement with the National Science Foundation.

[4]The *Wide-field Infrared Survey Explorer* is a joint project of the University of California, Los Angeles, and the Jet Propulsion Laboratory/California Institute of Technology, funded by the National Aeronautics and Space Administration

2.2.2 Stellar Mass Estimation

In estimating stellar masses for our sample, we need to account for galaxy-to-galaxy variations in the stellar mass-to-light ratio (M/L). Bell & de Jong (2001) demonstrate that galaxy M/L ratios should vary systematically with star formation history and enrichment history, leading to a dependence of M/L on galaxy color. Accounting for the correlation between M/L ratio and color is particularly important for mass estimates of starburst galaxies, whose young stellar populations amplify the luminosities of all UV-NIR bands.

To correct for this effect, we obtain galaxy colors from the Sloan Digital Sky Survey (SDSS[5]) Ninth Data Release (Ahn et al., 2012). SDSS data are available for 513 of the 565 galaxies in the fall-sky sample. SDSS photometry can be problematic, particularly for low surface brightness or irregular galaxies. The SDSS de-blending pipeline separates overlapping objects and sometimes incorrectly shreds one "parent" galaxy into multiple "children" (e.g., Abazajian et al., 2004; West et al., 2010). To determine whether shredding is a concern for our sample, we examine the SDSS data by eye for 10% of the ALFALFA-Hα galaxies. For 90% of these galaxies, the g and r photometry of the brightest de-blended child and the parent object agree to within 0.2 mag. We therefore select the brightest de-blended child for each ALFALFA-Hα galaxy from the SDSS catalog. As an additional check, we compare the SDSS r-band magnitudes with the R-band photometry for the full fall-sky ALFALFA-Hα sample. The photometric data from SDSS and the ALFALFA-Hα R-band data show a tight, linear relationship (Figure 2.1), although noticeable outliers exist. An examination of the outliers shows that they are caused by SDSS de-blending errors, overlapping or nearby bright stars, and incorrectly separated mergers. We treat the SDSS photometry as unreliable if it differs from a least-squares fit to the R-band data by more than 1 mag (Figure 2.1).

[5]Funding for SDSS-III has been provided by the Alfred P. Sloan Foundation, the Participating Institutions, the National Science Foundation, and the U.S. Department of Energy Office of Science.

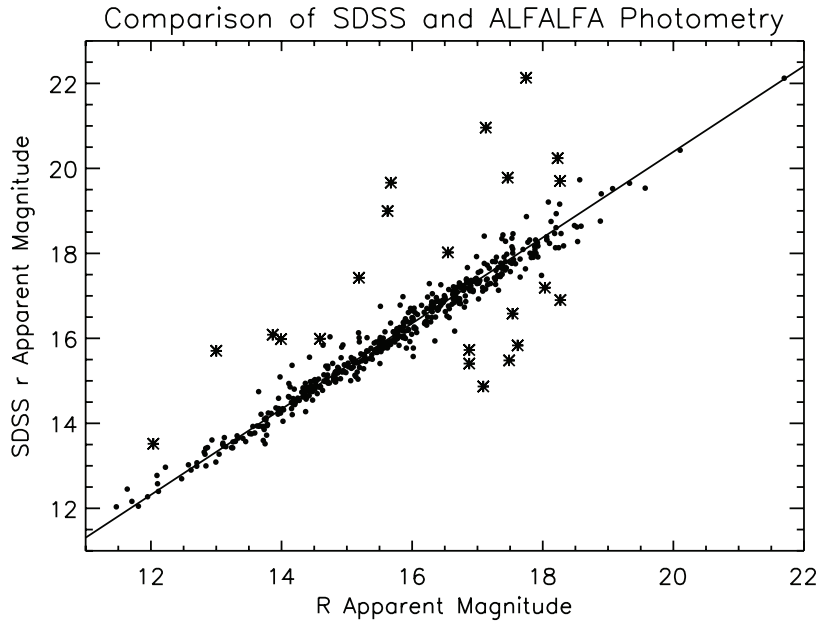

Figure 2.1: A comparison of the SDSS r-band and the ALFALFA-Hα R-band photometry for galaxies in the fall sample. The line represents a least-squares fit to all data points. Statistical errors are typically smaller than the symbol size. Asterisks indicate galaxies with r-band magnitudes that differ from the fitted line by more than 1 mag.

We also eliminate the SDSS photometry for one additional galaxy with a discrepant g-band magnitude that results in an unrealistically red $g-r$ color. We do not include these galaxies in any analyses that rely on SDSS-derived parameters, such as stellar masses or galaxy radii. These cuts lead to a sample of 489 ALFALFA-Hα galaxies with SDSS photometry. Including the galaxies with uncertain SDSS photometry does not affect any of our conclusions in the following sections.

We calculate stellar masses using the SDSS r-band luminosities and the relationship between M/L ratio and $g-r$ color from Table 7 of Bell et al. (2003). We first subtract the observed Hα fluxes from the r-band fluxes to ensure that nebular emission does not affect the galaxy colors or magnitudes. In addition, we subtract 0.093 dex from the Bell et al. (2003) M/L ratios to convert from a "diet" Salpeter (1955) initial mass function (see Bell & de Jong, 2001) to a Chabrier (2003) initial mass function (Gallazzi et al., 2008; Zibetti et al., 2009). We also compare the stellar

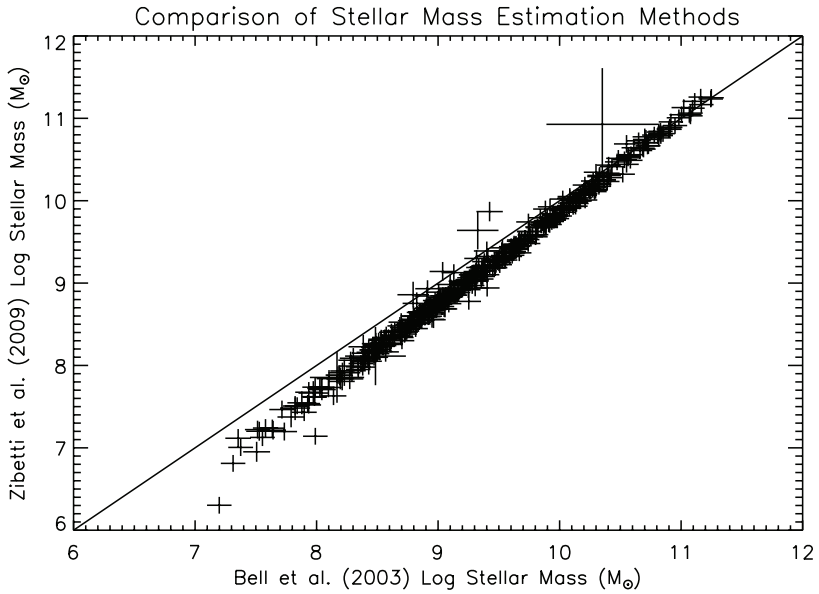

Figure 2.2: A comparison of the stellar masses estimated following Bell et al. (2003) and Zibetti et al. (2009). The solid line indicates a one-to-one relation. All masses were estimated using r-band luminosities and $g-r$ colors. The errors shown include the statistical photometric errors and the 0.1 dex scatter in the M/L-color relation (Bell et al., 2003). The Zibetti et al. (2009) stellar masses are lower, particularly at the low-mass end, due to their adoption of bursty star formation histories.

mass estimates with the alternative prescription of Zibetti et al. (2009). While Bell et al. (2003) model galaxy colors by assuming a smooth star formation history, Zibetti et al. (2009) consider the effect of bursts. As a result, masses obtained following Zibetti et al. (2009) are generally lower than the Bell et al. (2003) mass estimates (Figure 2.2). In particular, at the low-mass end, the stellar masses differ by about a factor of three. However, the relative stellar masses of the galaxies in the sample are only weakly affected. We use the Bell et al. (2003) stellar mass estimates for the rest of our analysis, but we note that using the Zibetti et al. (2009) mass estimates does not change our conclusions.

2.2.3 Selection of Starbursts

We define starbursts as galaxies with Hα equivalent widths (EWs) greater than 80 Å. This EW corresponds to a birth rate parameter of $\sim$2, i.e., the starbursts have SFRs greater than or equal to twice their past average SFR (Lee et al., 2009a). Since dust in starburst galaxies may attenuate the ionizing continuum radiation more than the optical stellar continuum, dust effects may lower the observed Hα EWs in starbursts (e.g., Calzetti, 1997; Charlot & Fall, 2000). The Hα EWs of the starbursts may therefore underestimate their ratios of current to past star formation. Eight galaxies (1.4% of the sample) have EWs above the 80 Å cut (Figure 2.3), which is equivalent to an sSFR cut of approximately 10^{-9} yr^{-1}. We list the EWs, SFRs, and H I and stellar masses of the starbursts in Table 2.1.

Since we are incomplete below $M_{\rm HI}$= $10^{9.5}$ M$_\odot$, we may not detect all the starbursts in the fall-sky volume. For a rough estimate of our completeness, we examine the larger, optically-selected sample of Bothwell et al. (2009), which contains 1110 galaxies at distances less than $\sim$43 Mpc. While the Bothwell et al. (2009) sample selection is less uniform than the ALFALFA-Hα sample, it does contain a higher fraction of low-mass galaxies. Assuming the lowest ratios of $M_{\rm HI}$/SFR observed in the Bothwell et al. (2009) sample, we should detect all starbursts with $M_* = 10^8$ M$_\odot$ and sSFR$\gtrsim 10^{-7}$ yr^{-1} and all starbursts with $M_* = 10^9$ M$_\odot$ and sSFR$\gtrsim 10^{-8}$ yr^{-1}. However, we may miss low-mass starburst galaxies whose gas is predominantly molecular. Although the few low-mass starbursts with CO measurements generally appear to have larger H I masses than H_2 masses (e.g., Kobulnicky et al., 1995; Stil & Israel, 2002; Bravo-Alfaro et al., 2004; Israel, 2005; Nidever et al., 2013), we caution that we may not detect the most extreme, low-mass starbursts with the highest H_2/H I ratios.

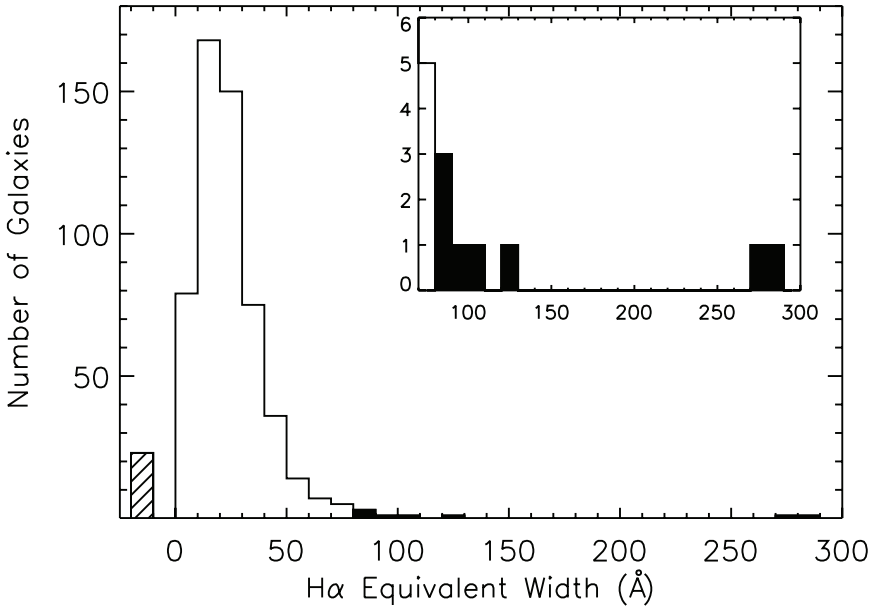

Figure 2.3: The distribution of the Hα EWs in the fall ALFALFA-Hα sample. The solid region of the histogram indicates starburst galaxies. The hatched bin at negative EWs represents galaxies without Hα detections. The inset shows a zoomed-in view of the high-EW section of the histogram.

2.2.4 WISE Data

Dust extinction may substantially affect the observed star formation properties of the ALFALFA-Hα galaxies. Using infrared measurements from *WISE*, we examine the accuracy of the ALFALFA-Hα extinction corrections. Later, in § 2.3.1.2, we consider the relationship between dust and H I content.

We obtain 3.4, 4.6, 12, and 22 μm fluxes for the sample from the *WISE* All-Sky Release Source Catalog (Wright et al., 2010; Cutri & et al., 2012). We use the elliptical aperture photometry for objects flagged as extended in the catalog and the profile fit magnitudes for all other sources. We then match each ALFALFA-Hα galaxy to its closest *WISE* counterpart within 6″, the resolution at 3.4 μm. Following Jarrett et al. (2013), we apply the necessary color and magnitude corrections to the *WISE* photometry. Of the 565 ALFALFA-Hα fall galaxies, 358 have 3.4, 4.6 and 12 μm detections and 263 galaxies have 22 μm detections.

The extinction corrections adopted for the ALFALFA-Hα galaxies in (§ 2.2.1) are

based on the galaxies' R-band luminosities. To verify this extinction correction, we use the *WISE* and Hα observations to estimate extinction-corrected SFRs. Wen et al. (2014) calibrate the WISE 12μm and 24μm bands as extinction indicators using the Hα/Hβ ratios from SDSS spectra of low-redshift star-forming galaxies. Following Wen et al. (2014), we calculate

$$\mathrm{SFR} = 1.473 \times 10^{-41.27} L_{\mathrm{H}\alpha,\mathrm{obs}} + \alpha \nu L_{\nu}, \tag{2.2}$$

where $L_{\mathrm{H}\alpha,\mathrm{obs}}$ is the Hα luminosity without an internal extinction correction, νL_{ν} is the appropriate *WISE* band luminosity, and α is a coefficient that depends on the *WISE* band and extinction law adopted and which ranges from $\sim$0.02-0.04. The factor of 1.473 in the equation converts from the Kennicutt & Evans (2012) SFR calibration to the Kennicutt (1998a) calibration. We calculate extinction-corrected SFRs using the *WISE* 12 μm and 22 μm luminosities and assuming a Calzetti et al. (2000) extinction law. We compare these SFRs with the ALFALFA-Hα SFRs in Figure 2.4. A few galaxies show higher SFRs using the *WISE* extinction correction than the original ALFALFA-Hα extinction correction. These galaxies show prominent dust lanes or appear reddened in SDSS images. For these particular objects, the original extinction correction used to derive the ALFALFA-Hα SFRs is likely insufficient. The *WISE*-derived SFRs appear systematically lower than the ALFALFA-Hα SFRs by $\sim$0.1 dex for several galaxies, mostly point-source *WISE* detections. The *WISE* profile-fit fluxes for these sources may be underestimated, as discussed in Cutri et al. (2012). Overall, however, the *WISE*-derived SFRs and ALFALFA-Hα SFRs show reasonable agreement.

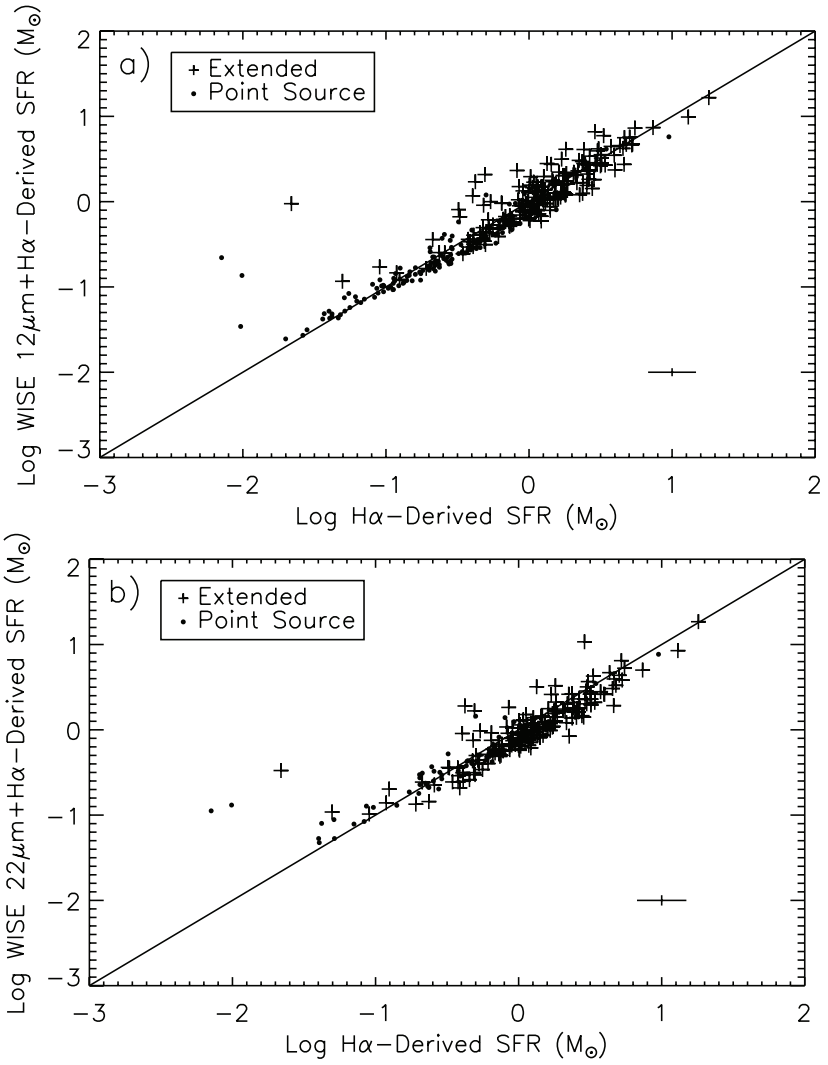

Figure 2.4: A comparison of the ALFALFA-Hα SFRs with SFRs corrected for extinction using (a) *WISE* 12 μm luminosities and (b) 22 μm luminosities. Circles indicate galaxies detected as point sources in the *WISE* catalog, and crosses indicate galaxies detected as extended objects in the catalog. The solid line shows a one-to-one relation. Representative error bars are shown in the lower right corner.

2.3 Results

2.3.1 H I Gas Content

2.3.1.1 The H I Gas Supply of Starbursts

Star formation is intimately linked with the cold gas content of galaxies. A large H I supply may be necessary to fuel high SFRs, but the resulting feedback may expel or ionize much of the H I gas. Given the extreme levels of star formation and feedback in starburst galaxies, we consider whether their H I content differs from the other galaxies in the ALFALFA-Hα sample. High starburst H I gas fractions may suggest that a large gas reservoir is a key precondition for triggering a starburst, while H I-deficiencies might indicate that radiative feedback plays the dominant role in shaping starbursts' ISM.

In non-starbursts, larger H I reservoirs do appear to lead to enhanced star formation. As shown by Huang et al. (2012) for ALFALFA galaxies, SFR correlates with $M_{\rm HI}$, indicating a link between atomic gas and star formation. Since part of this trend may result from the tight relation between SFR and stellar mass, we examine whether highly star-forming galaxies have more H I than galaxies of a similar mass. In Figure 2.5, we show the ratio of $M_{\rm HI}$ to stellar mass (M_*) as a function of SFR and M_*. Previous studies have found that at a given stellar mass, galaxies with higher SFRs tend to be more H I-rich (e.g., Catinella et al., 2010; Huang et al., 2012), and the ALFALFA-Hα sample also exhibits this trend. However, while some of the starbursts' SFRs are at least an order of magnitude higher than other galaxies of the same mass, their H I gas fractions do not show a comparable increase. In fact, the starburst H I gas fractions are similar to those of star-forming galaxies with much lower SFRs. In the starburst regime, H I content and star formation do not appear to be closely coupled.

The starbursts are H I-rich relative to the ALFALFA-Hα sample as a whole, but

this H I-richness results from their lower-than-average stellar masses. Low-mass galaxies in general tend to be more H I-rich (e.g., Gavazzi et al., 1996; Huang et al., 2012), and in most cases, the H I gas fractions of the starbursts are similar to other low-mass, gas-rich galaxies. The relatively high $M_{\rm HI}$ limit of the ALFALFA-Hα survey leads to a tight relation between $M_{\rm HI}/M_*$ and M_*; Figure 2.6 displays the least-squares fit to this relation for the non-starbursts in the sample. Most of the starbursts have $M_{\rm HI}/M_*$ values that are within 1σ of the best-fit line. Only two of the starbursts have $M_{\rm HI}/M_*$ ratios that appear high for their stellar mass, deviating by $> 2\sigma$ from the main trend (Figure 2.6). One starburst even has a lower-than-average H I gas fraction. This fact suggests that the high SFRs of the starbursts are not caused by an excess of H I, but rather by an enhanced efficiency of converting H I into H_2 gas and stars.

Although the starbursts are not excessively H I-rich for their stellar masses, they are also not H I-deficient. This conclusion contrasts with the results of Oey et al. (2007) for starbursts in the SINGG sample and may indicate that radiative feedback in the ALFALFA-Hα starbursts does not significantly affect their total gas content. However, Oey et al. (2007) use R-band magnitude as a proxy for stellar mass and identify starbursts based on star formation intensity (SFI), rather than EW. To compare with the SINGG results, we calculate the SFI for a flat disk morphology as

$$\mathrm{SFI} = \frac{\mathrm{SFR}_{50}}{2\pi R_{50}^2}, \tag{2.3}$$

where R_{50} is the R-band half-light radius and SFR_{50} is the SFR within that radius. We show the relation between SFI and the ratio of $M_{\rm HI}$ to R-band luminosity, $M_{\rm HI}/L_R$, in Figure 2.7a. Galaxies with higher SFI do appear to have lower ratios of $M_{\rm HI}/L_R$. On the other hand, as discussed in § 2.2.2, R-band luminosities may overestimate the stellar masses of starbursts, leading to underestimates of their H I gas fractions.

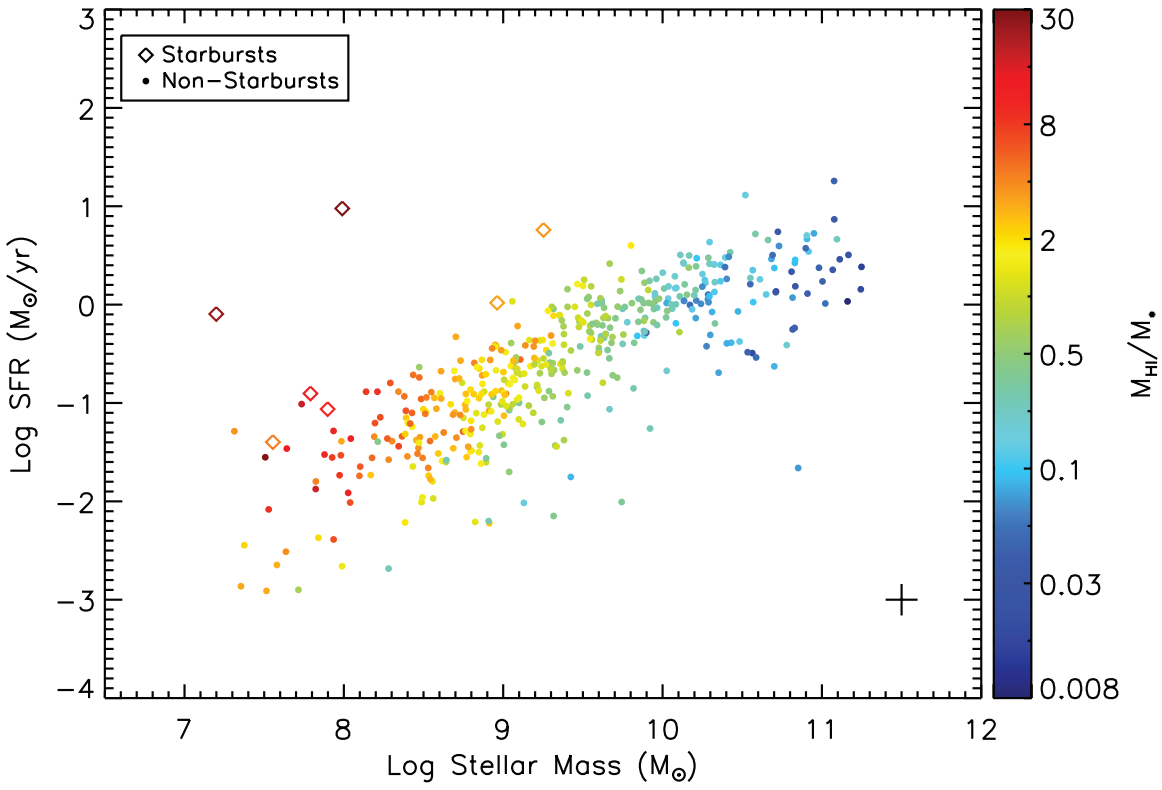

Figure 2.5: SFR and M_* for the fall ALFALFA-Hα sample. Color shows M_{HI}/M_*, and diamonds indicate starburst galaxies, as identified by Hα EW. The black cross at the lower right shows representative error bars. At a given M_*, galaxies with higher SFRs tend to have slightly higher H I gas fractions.

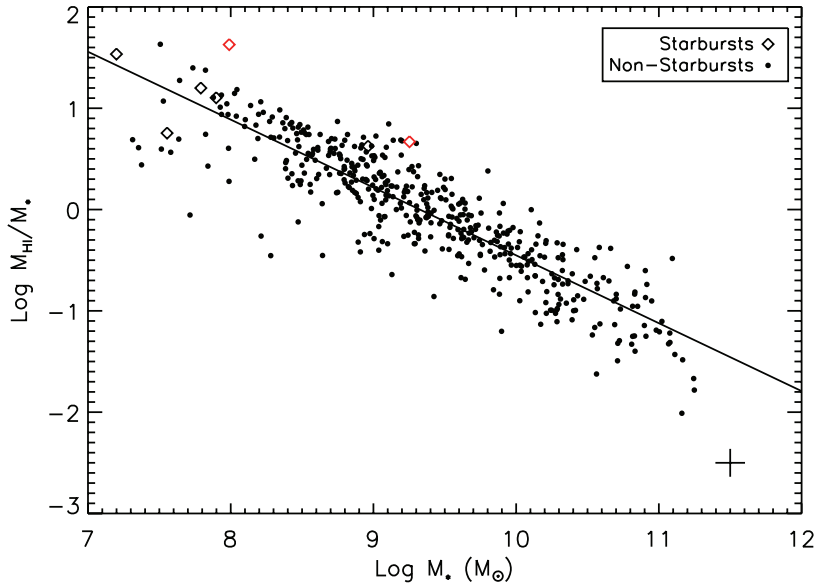

Figure 2.6: $M_{\rm HI}/M_*$ and M_* for the fall ALFALFA-Hα sample. Symbols are described in Figure 2.5. The solid line shows a least-squares fit to the non-starburst galaxies. Two starbursts, shown in red, have $M_{\rm HI}/M_*$ values 2σ higher than the best-fit line.

In Figure 2.7b we replace L_R with M_*, calculated as described in § 2.2.2. The trend between H I content and SFI now appears weaker, and even at the highest SFI end, galaxies span a range of H I gas fractions. The residual negative correlation between $M_{\rm HI}/M_*$ and SFI is due to the scalings of H I gas fraction, SFR, and half-light radius with M_* in the ALFALFA-Hα mass regime (e.g., Catinella et al., 2010; Huang et al., 2012; Brinchmann et al., 2004; Shen et al., 2003). Feedback from starbursts at high SFI does not necessarily result in a reduced H I content.

The H I-richness of the starbursts indicates that they are not able to completely ionize or consume their neutral gas. Radiative feedback in high SFI galaxies does not appear to significantly affect their global H I gas fractions, perhaps because most of the H I gas mass resides at radii well outside the star-forming regions. The gas column near the starburst may be thick enough to prevent the escape of ionizing photons, and in addition, any decrease in H I from photoionization may be offset by an increase in H I from H_2 photodissociation.

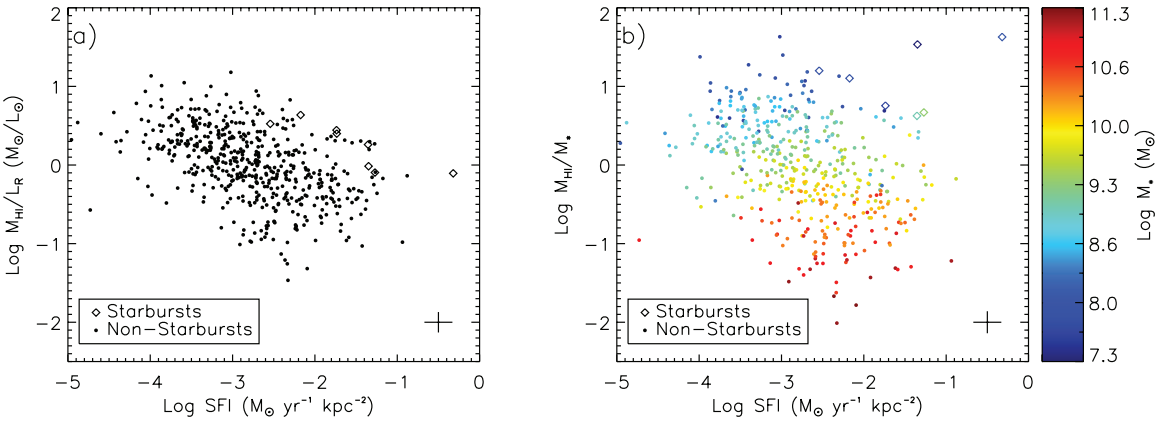

Figure 2.7: (*a*) $M_{\rm HI}/L_R$ vs. SFI, with symbols as in Figure 2.5. Galaxies with higher SFI have lower $M_{\rm HI}/L_R$. (*b*) When we substitute M_* estimates from SDSS photometry for L_R, $M_{\rm HI}/M_*$ shows a weaker negative correlation with SFI, and high SFI galaxies span a wide range of $M_{\rm HI}/M_*$. Color shows M_*.

2.3.1.2 The Connection Between H I Gas Fraction and Specific Star Formation Rate

The ALFALFA-Hα galaxies indicate that H I gas fraction generally increases with sSFR, although this trend may flatten in the starburst regime and the data show substantial scatter. The relatively weak connection between sSFR and H I gas fraction (Figure 2.8) is seemingly at odds with the well-established tight correlation between H I gas fraction and NUV-r color (e.g., Catinella et al., 2010; Huang et al., 2012). The GASS sample shows that the best predictors of a galaxy's H I gas fraction are NUV-r and stellar mass surface density (Catinella et al., 2010). Similarly, we observe a tight trend between H I gas fraction and SDSS $g-r$ color (Figure 2.9a). The weaker trend with Hα-derived sSFR and strong trend with $g-r$ suggest two possible explanations: (1) dust extinction drives the close correlation between $g-r$ color and H I or (2) galaxies' global H I content is more closely linked with the SFR averaged over long timescales than with instantaneous star formation (e.g., Kannappan et al., 2013).

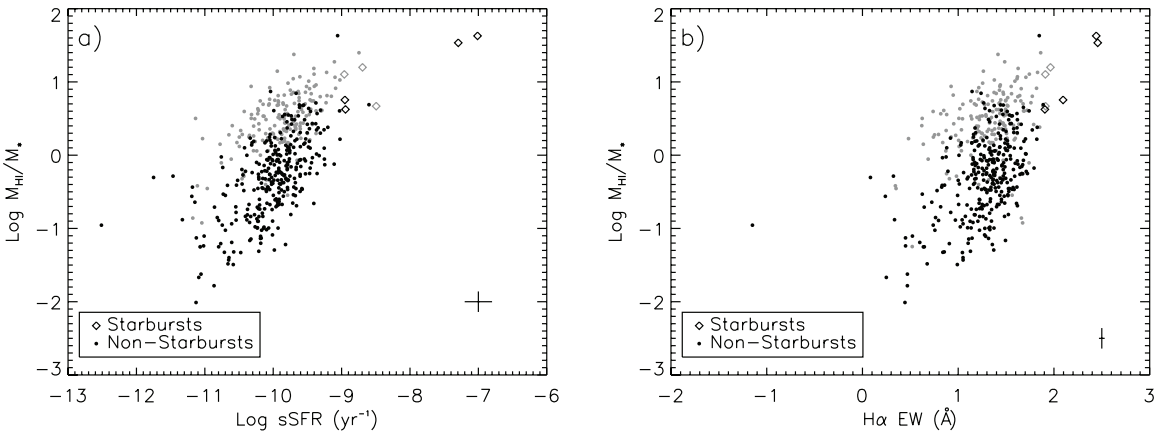

Figure 2.8: $(a) M_{\rm HI}/M_*$ vs. sSFR, with symbols as in Figure 2.5. To compare with Figure 2.9b, we show ALFALFA-Hα galaxies detected in *WISE* in black and non-detections in gray. (b) $M_{\rm HI}/M_*$ vs. Hα EW.

To estimate the effect of dust extinction on SDSS color, we use the *WISE* 12 μm and 22 μm luminosities to derive the $E(g-r)$ color excess. Following Wen et al. (2014), we calculate $E(B-V)$ using

$$\frac{\nu L_\nu}{L_{\rm H\alpha(obs)}} = \frac{10^{0.4 k_{\rm H\alpha} \times E(B-V)} - 1}{\alpha} \tag{2.4}$$

where νL_ν is the 12 μm or 22 μm luminosity, $L_{\rm H\alpha(obs)}$ is the Hα luminosity with no correction for internal extinction, $k_{\rm H\alpha}$ is the reddening curve at Hα, and α is a coefficient that depends on the extinction law and *WISE* band used (Wen et al., 2014). We then convert $E(B-V)$ to $E(g-r)$, using the conversion in Yuan et al. (2013). The median A_V values inferred for the ALFALFA-Hα sample using the Calzetti et al. (2000) and Cardelli et al. (1989) extinction laws are in the range of 0.5-0.6. These values are comparable to the face-on A_V values calculated from radiative transfer models of spiral galaxies (Xilouris et al., 1999; Bianchi, 2007; De Geyter et al., 2014). After correcting the SDSS $g-r$ colors for extinction, the trend with H I gas fraction weakens substantially (Figure 2.9).

We run Bruzual & Charlot (2003) stellar population synthesis (SPS) models to

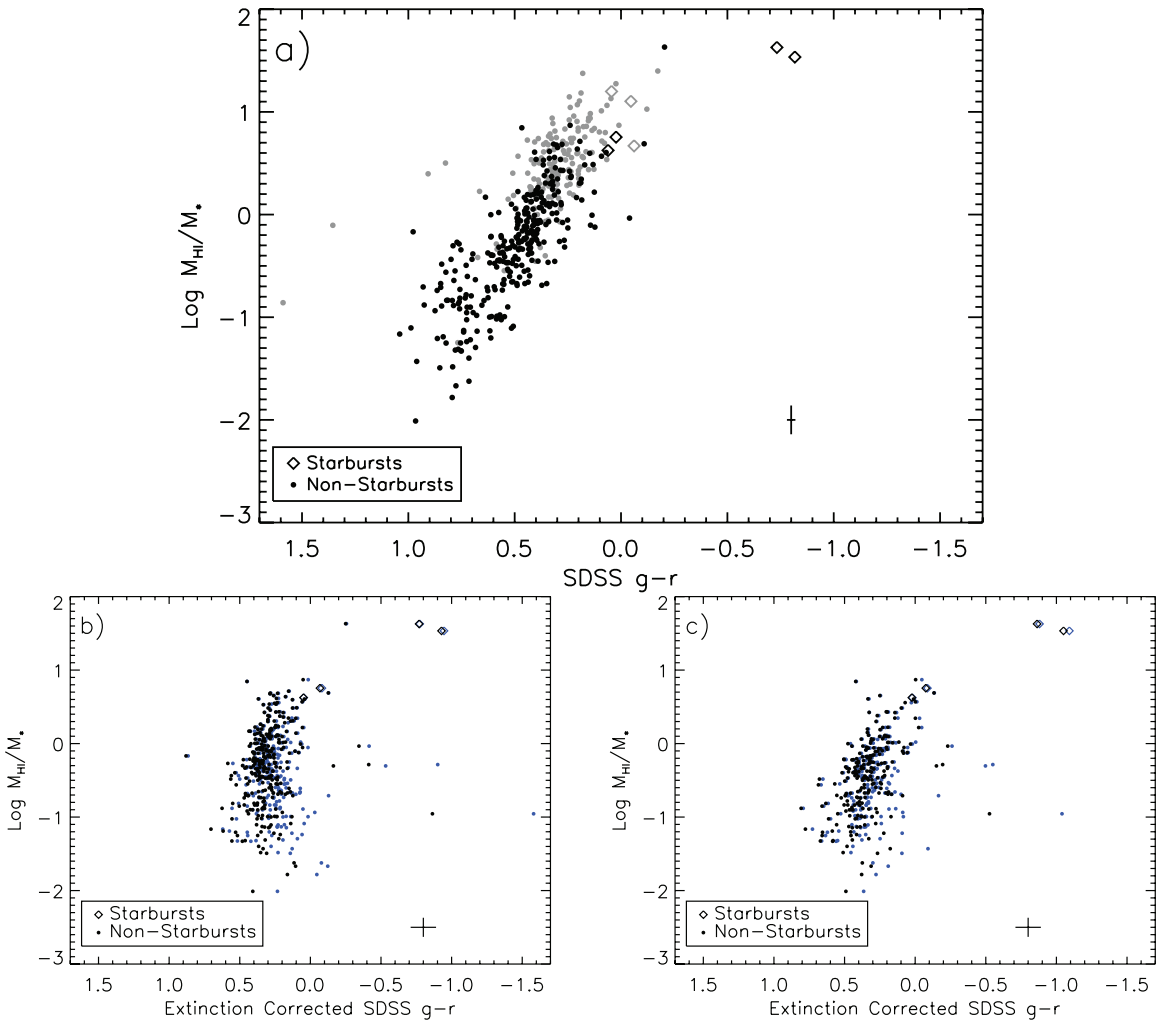

Figure 2.9: (*a*) SDSS $g-r$ color and $M_{\rm HI}/M_*$ show a tight correlation. Symbols and colors are the same as in Figures 2.5 and 2.8. The x-axis is flipped to match the orientation of Figure 2.8. (*b*) $M_{\rm HI}/M_*$ vs. SDSS $g-r$ color, after correcting for extinction using the *WISE* 12 μm luminosities. Black points indicate extinctions derived assuming a Calzetti et al. (2000) extinction law, and blue points indicate extinctions derived with the Cardelli et al. (1989) extinction law. The calculated errors include photometric uncertainties, the uncertainties in the coefficients in Equation 2.4 due to adopting different extinction laws, and the uncertainty in the $E(B-V)$ to $E(g-r)$ conversion. (*c*) $M_{\rm HI}/M_*$ vs. SDSS $g-r$ color, after correcting for extinction using the *WISE* 22 μm luminosities.

confirm whether the above dust extinction corrections are realistic for the low sSFR galaxies in our sample. We use the Padova 1994 isochrones at metallicities of 0.2 and 1 $Z_{\odot}$ (Bressan et al., 1993; Fagotto et al., 1994) and the Chabrier (2003) initial mass function. To estimate the expected colors of the low sSFR galaxies, we adopt a log-normal star formation history, as recommended by Gladders et al. (2013) for field galaxies. For present-day sSFRs of $10^{-12} - 10^{-11}$ yr^{-1} and peak star formation at $z = 0.7 - 3$, the intrinsic $g - r$ colors range from 0.5 to 0.8. While not exhaustive, these models hint at the range of colors we should expect for the reddest galaxies in the absence of dust.

The SPS models cannot reproduce the reddest observed $g-r$ colors, $(g-r) > 0.8$, even assuming peak star formation at $z \geq 6$. In fact, as suggested by the extinction-corrected colors in Figure 2.9, a wide range of star formation histories produces a relatively narrow range of stellar population colors. The extinction-corrected colors in Figure 2.9 do appear more blue than predicted by the SPS models, with median $g-r$ colors of 0.2-0.3 using the 12μm band and 0.4-0.5 using the 22μm band. Although *WISE* is less sensitive at 22μm than at 12μm, the warm dust traced by the 22μm band (Jarrett et al., 2013) may be a better indicator of the total stellar extinction than the polycyclic aromatic hydrocarbons (PAHs) traced by the 12μm band. Adopting a more realistic, bursty star formation history in the models could also lead to better agreement with the *WISE* extinction-corrected colors. Regardless, the *WISE* data and SPS models suggest that dust extinction could be responsible for the tight correlation between $g - r$ color and H I gas fraction.

Figures 2.8 and 2.9 show that, in star-forming galaxies, H I gas fraction correlates weakly with sSFR; the tight connection between H I and $g - r$ color may stem almost entirely from a link between extinction and H I gas fraction. Nevertheless, we caution that ALFALFA misses most galaxies on the red sequence (Huang et al., 2012), and including this population may result in a clearer trend between color and H I gas

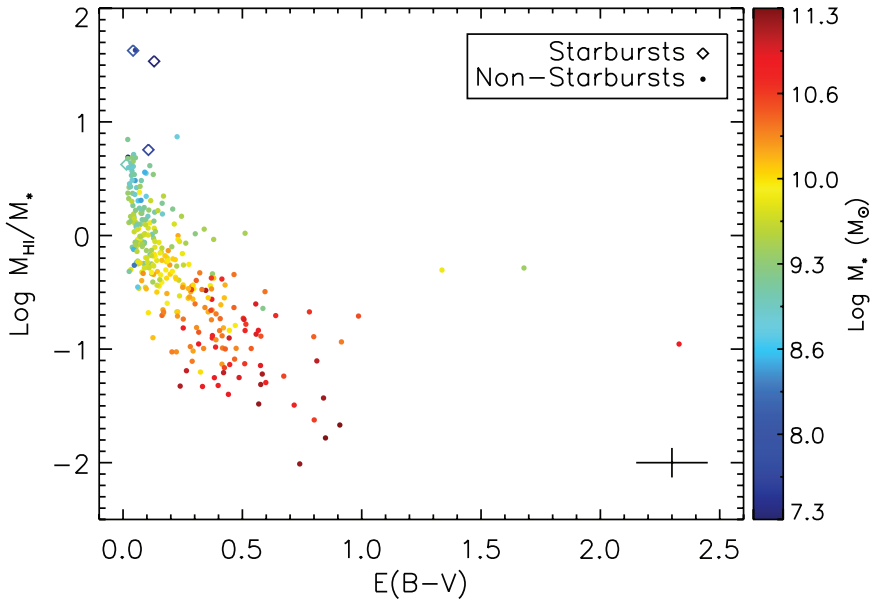

Figure 2.10: $M_{\rm HI}/M_*$ vs. $E(B-V)$ derived using the *WISE* 12μm luminosities and Cardelli et al. (1989) extinction law. Color indicates stellar mass. Symbols are described in Figure 2.5.

fraction. For our sample, the correlation between H I gas fraction and color may reflect an underlying trend between dust content and stellar mass. Figure 2.10 illustrates that the *WISE*-derived extinctions, from the 12μm luminosities and Cardelli et al. (1989) extinction law, correlate with stellar mass and anti-correlate with H I gas fraction. The results for the *WISE* 22 μm data and for the Calzetti et al. (2000) extinction law are similar. The outlier at the highest $E(B-V)$ in Figure 2.10 is UGC 1488, which has a high inclination, prominent dust lane, and signs of morphological disturbance. Higher mass, star-forming galaxies have both higher dust masses and higher dust-to-gas ratios, possibly due to the galaxies' higher average metallicities. Conversely, these same high-mass, dusty galaxies have low H I gas fractions, due to a higher star formation efficiency or a lower gas accretion rate (e.g., Davé et al., 2011a; Kannappan et al., 2013).

The metallicities of galaxies may set their dust content and may ultimately drive the observed trend between $g-r$ color and H I gas fraction. Bothwell et al. (2013) show that the mass-metallicity relation of galaxies depends strongly on H I gas fraction. As

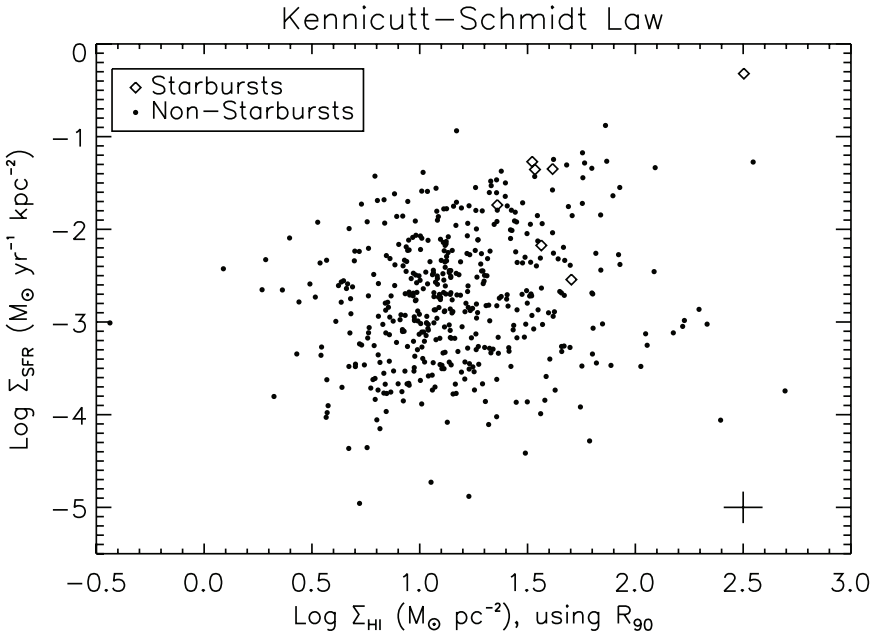

Figure 2.11: $\Sigma_{\rm SFR}$ vs. $\Sigma_{\rm HI}$, calculated from Equations 2.3 and 2.5. Since H I radii are typically more extended than R_{90}, $\Sigma_{\rm HI}$ is likely overestimated. The error bars account for statistical uncertainties only.

a galaxy evolves, the balance of H I inflows, star formation, and outflows determines both its metallicity and its H I gas fraction. The tight trend between color and H I gas fraction is therefore a manifestation of the key role of H I gas in regulating galaxy metallicities.

2.3.1.3 Kennicutt-Schmidt Law

Although H I gas fraction and sSFR do not appear strongly correlated, gas surface density may be the more relevant parameter for star formation. According to the Kennicutt-Schmidt Law (Kennicutt, 1998b), galaxies with a higher SFR surface density should have a higher gas surface density. We set $\Sigma_{\rm SFR}$ equal to the SFI calculated in Equation 2.3. Due to the $3.5'$ resolution of the Arecibo beam, we do not have radii for the H I gas. However, since H I diameters are observed to scale with galaxy optical diameters (e.g., Broeils & Rhee, 1997; Swaters et al., 2002), we use the SDSS radius containing 90% of the r-band light, R_{90}, as an estimate for H I radius and calculate

$\Sigma_{\rm HI}$ as

$$\Sigma_{\rm HI} = \frac{M_{\rm HI}}{2\pi R_{90}^2}. \tag{2.5}$$

H I diameters are typically larger than optical diameters, so these $\Sigma_{\rm HI}$ values are likely overestimates.

We plot $\Sigma_{\rm SFR}$ and $\Sigma_{\rm HI}$ for the sample in Figure 2.11. We find no correlation between the H I and SFR surface densities, consistent with results that show that molecular gas primarily sets the Kennicutt-Schmidt Law (Schruba et al., 2011). Although most galaxies lie near the threshold density of $\sim$10 $M_\odot$ pc^{-2} for conversion to molecular gas, we expect their actual $\Sigma_{\rm HI}$ values to be below this threshold, due to our underestimate of the H I radii. On average, the starbursts tend to have elevated $\Sigma_{\rm HI}$ relative to the rest of the sample, with an average $\Sigma_{\rm HI}$ more than 3 times higher than the non-starbursts. Higher surface densities may aid the conversion of atomic gas to molecular gas and fuel star formation. Alternatively, the starbursts may have more spatially extended H I than the other galaxies, or they may have lower metallicities and higher H I saturation thresholds (e.g., Bolatto et al., 2011). As with H I gas fraction, the starbursts' $\Sigma_{\rm HI}$ tend to be high, but they do not differ dramatically from the non-starbursts in the sample.

Whether we consider sSFR, Hα EW, extinction-corrected $g-r$ color, or SFI, the H I content of galaxies shows only a weak connection with star formation. The starbursts have high H I gas fractions compared to the full ALFALFA-Hα sample but show little to no increase in H I gas fraction relative to similar mass galaxies. These observations suggest that the H I content of gas-rich galaxies remains relatively constant, even during a starburst episode. Any excess H I is efficiently converted into H_2, and photodissociation of H_2 may balance the consumption or ionization of H I.

2.3.2 Star Formation Efficiency

Since the starbursts have slightly high, but not unusual, H I content for their masses, their SFRs imply a high star formation efficiency (SFE). We calculate the inverse of the SFE, the H I gas depletion timescale, as

$$t_{\rm dep} = \frac{M_{\rm HI}}{\rm SFR}, \tag{2.6}$$

and we show the relation between $t_{\rm dep}$ and sSFR in Figure 2.12. The starburst H I depletion times are listed in Table 2.1. Most of the sample shows no correlation between sSFR or EW and H I depletion time. However, the starbursts tend to have short H I depletion times, despite the fact that they are H I-rich. All the starbursts have H I gas fractions above the sample median, and all but one have depletion times below the sample median. In particular, the two strongest or youngest starbursts, as measured by EW, have both the highest H I gas fractions and the highest SFE. Saintonge et al. (2011b) suggest that weak starbursts in the high mass GASS sample may not be able to access H I easily, since they have the same H I $t_{\rm dep}$ as non-starbursts. In contrast, our starbursts do show lower $t_{\rm dep}$, which may indicate that lower mass starbursts are efficiently converting H I to H_2 and stars.

In general, $t_{\rm dep}$ decreases slightly with M_* (Figure 2.13a), for masses below $10^{10}\,{\rm M}_\odot$ (e.g., Bothwell et al., 2009; Huang et al., 2012). The high H I gas fractions and low SFE observed for the lowest mass galaxies imply that their accretion rate exceeds their rate of H I-H_2 conversion (e.g., Huang et al., 2012; Kannappan et al., 2013). However, the low-mass end also contains several galaxies with $t_{\rm dep}$ an order of magnitude lower than the average for their stellar mass. When we bin the sample galaxies into equally spaced stellar mass bins, the lowest mass bin shows the highest scatter, a standard deviation of 0.64 dex, compared to deviations of $\sim$0.4 dex for the next three mass bins (Figure 2.13a). This lowest mass bin also exhibits the largest scatter (0.88 dex)

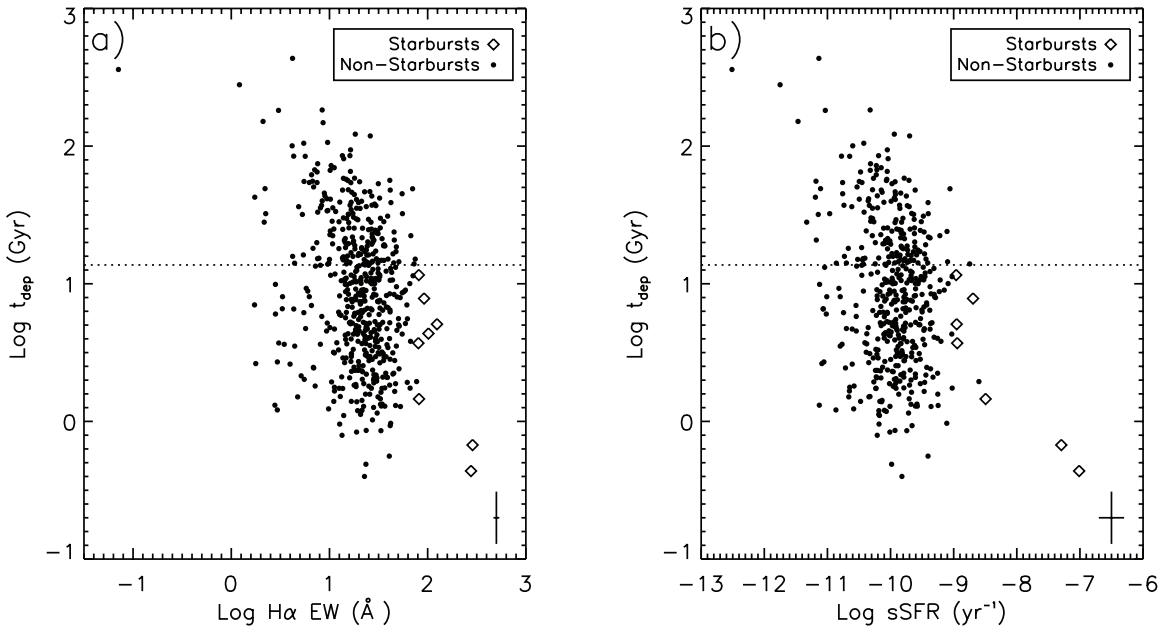

Figure 2.12: The relation between $t_{\rm dep}$ and Hα EW (left panel) and $t_{\rm dep}$ and sSFR (right panel). The right panel only includes galaxies with reliable SDSS photometry. The dashed line in both panels indicates the Hubble time. Despite their high H I content, most starbursts have shorter $t_{\rm dep}$ than the rest of the sample.

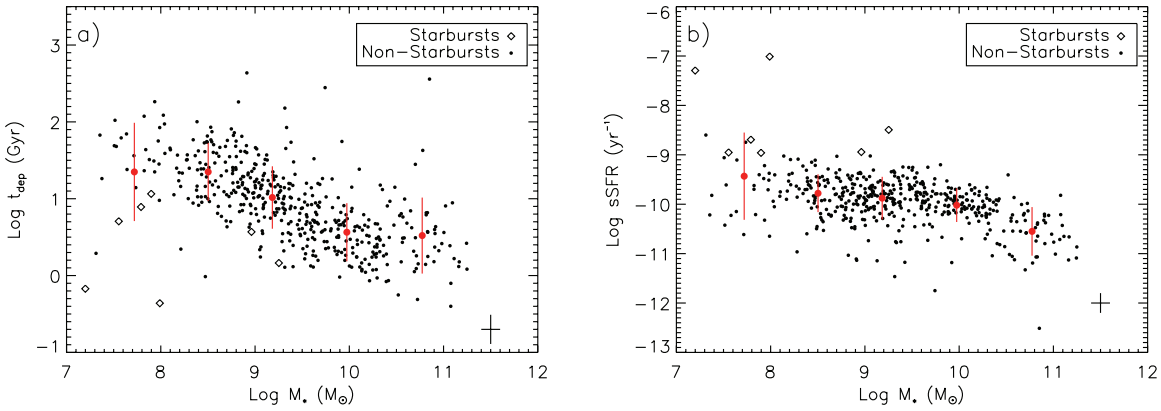

Figure 2.13: $t_{\rm dep}$ (left panel) and sSFR (right panel) as a function of M_*. The red points indicate the mean values for evenly spaced bins of M_* and the red error bars denote the standard deviation in each bin.

in sSFR (Figure 2.13b). Lee et al. (2007) explain the scatter in sSFR as an increase in"burstiness" at low stellar masses. The gas-richness of star-forming dwarf galaxies, combined with their wide-ranging star formation efficiencies, suggest that H I gas may accumulate until a dynamical disturbance triggers gas inflows and compression.

Galaxy structure may also play a role in determining H I to H_2 conversion efficiency. Blitz & Rosolowsky (2006) argue that in disk galaxies, the midplane pressure sets the H_2/H I ratio and hence the SFE. Since the midplane pressure should scale with stellar mass surface density, Σ_* (e.g., Blitz & Rosolowsky, 2004), we plot $t_{\rm dep}$ as a function of Σ_* in Figure 2.14. We calculate

$$\Sigma_* = \frac{M_*}{2\pi R_{50,r}^2} \tag{2.7}$$

where $R_{50,r}$ is the SDSS r-band Petrosian (1976) half-light radius. Figure 2.14 shows that for the ALFALFA-Hα galaxies, $t_{\rm dep}$ decreases with Σ_*, as expected if higher surface density disks convert H I to stars more efficiently.

However, this trend is the exact opposite of that found by Saintonge et al. (2012) for the COLD GASS survey, where the mean H I $t_{\rm dep}$ increases with Σ_*. The COLD GASS sample (Saintonge et al., 2011a,b; Catinella et al., 2012) is a random sub-

set of the optically-selected massive galaxies from the GASS sample. We show the H I $t_{\rm dep}$ and Σ_* of the COLD GASS galaxies, calculated following Equations 2.6 and 2.7, in Figure 2.14. The COLD GASS stellar masses and SFRs are calculated from SDSS and *GALEX* photometry (Saintonge et al., 2011a,b). We removed nine COLD GASS galaxies whose SDSS DR9 r-band magnitudes differed from the quoted r-band magnitudes in the COLD GASS catalog by more than 1 magnitude.

The discrepancy between the ALFALFA-Hα galaxies and the COLD GASS galaxies is likely due to the quenching of star formation in more massive galaxies. Figure 2.14 shows that the scatter in $t_{\rm dep}$ increases dramatically above a Σ_* of $10^{8.7}$ $M_\odot$ kpc^{-2}, identified as a "quenching threshold" by Catinella et al. (2010) and Saintonge et al. (2011a). The H I depletion times of the few ALFALFA-Hα galaxies in this high stellar surface density regime are consistent with those of the COLD GASS population. Saintonge et al. (2012) suggest that galaxies with high stellar surface densities may be more stable to fragmentation due to their bulge-dominated morphologies (e.g., Ostriker & Peebles, 1973) or may no longer have access to their H I reservoir.

We use the SDSS surface brightness profile fits of Simard et al. (2011) to quantify the morphologies of the COLD GASS galaxies. These fits are not available for the ALFALFA-Hα galaxies, which fall in the more recent, SDSS DR9 sky coverage. Following Simard et al. (2011), we adopt a bulge+disk model if the probability that the bulge+disk model is not required is below 0.32; if the probability is higher, we use a pure Sérsic model. Figure 2.15 shows that the COLD GASS disk galaxies continue the trend of decreasing $t_{\rm dep}$ with Σ_* seen in the ALFALFA-Hα sample, while spheroid-dominated galaxies deviate to higher $t_{\rm dep}$. Although all the offset galaxies appear to be bulge-dominated, they show no discernible trend between bulge-to-disk ratio and $t_{\rm dep}$.

The spheroidal galaxies also appear offset to lower sSFRs (Figure 2.16a) compared

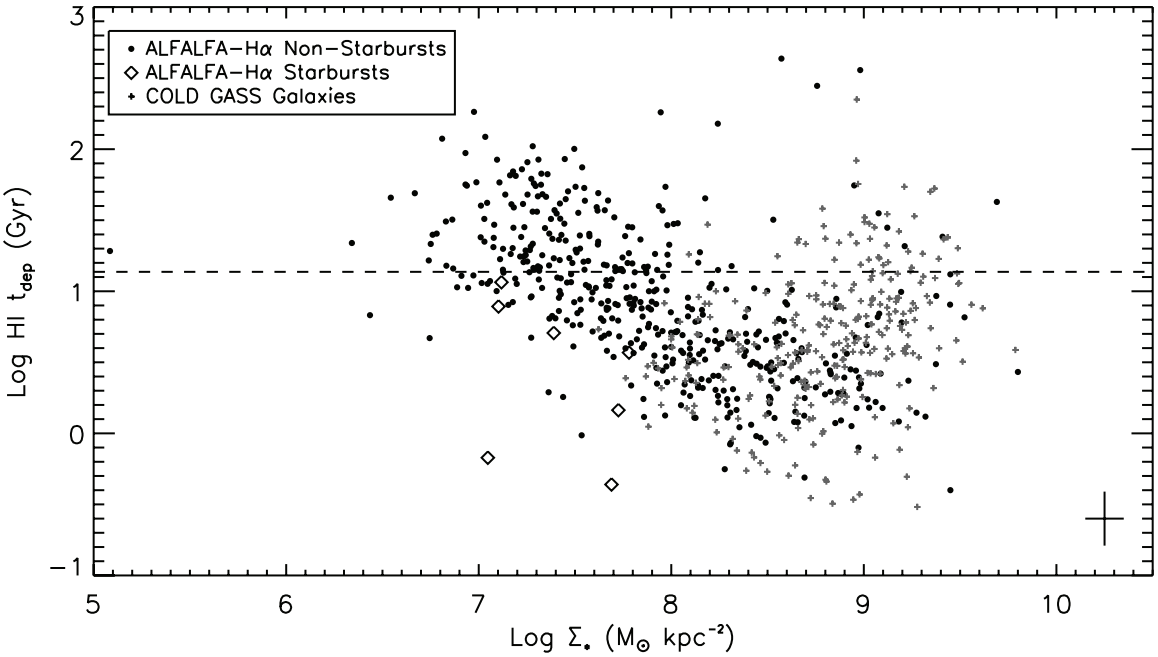

Figure 2.14: $t_{\rm dep}$ as a function of Σ_* for the ALFALFA-Hα sample (black circles and diamonds) and the COLD GASS sample (gray crosses). Below the "quenching threshold" of $\Sigma_* = 10^{8.7}$ $\rm M_\odot kpc^{-2}$ (Catinella et al., 2010; Saintonge et al., 2011a), $t_{\rm dep}$ decreases with increasing Σ_*. The black cross indicates the average statistical errors for the ALFALFA-Hα sample, and the dashed line indicates the Hubble time.

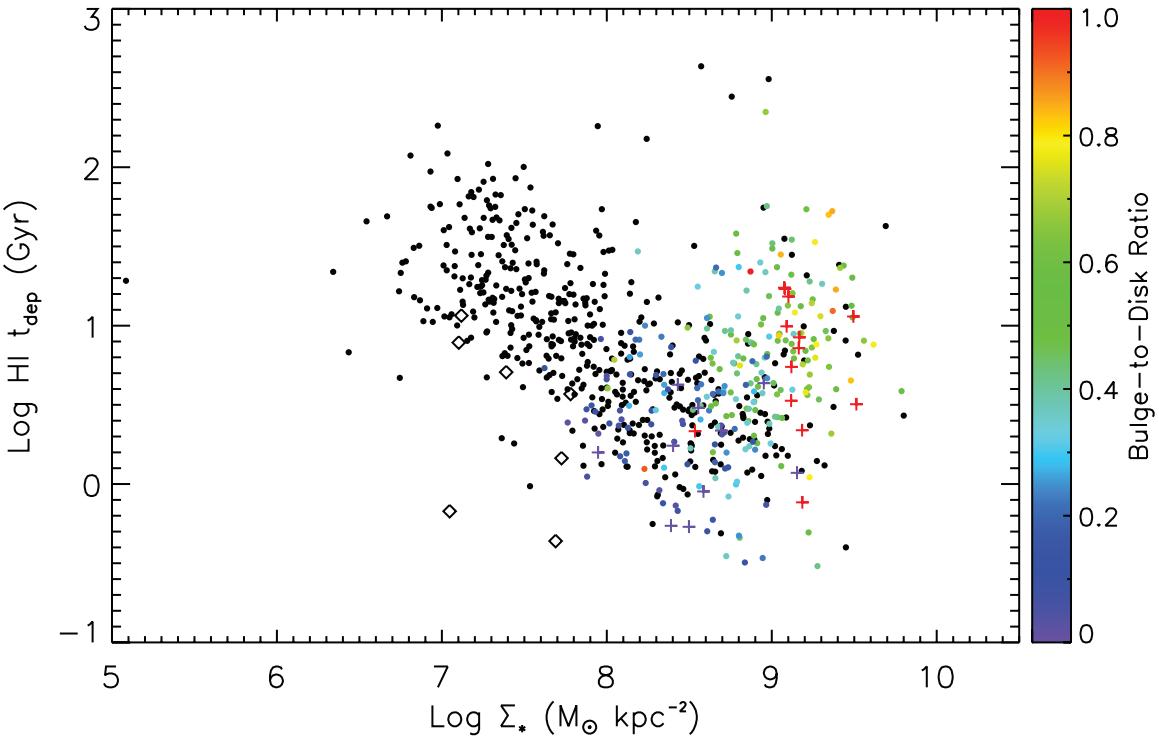

Figure 2.15: $t_{\rm dep}$ as a function of Σ_* for the ALFALFA-Hα non-starbursts (black circles) and starbursts (diamonds) and the COLD GASS sample (colored circles and crosses). The COLD GASS galaxies are colored by bulge-to-disk ratio from the Simard et al. (2011) SDSS fits. The crosses indicate COLD GASS galaxies for which a pure Sérsic profile is preferable; red crosses indicate a Sérsic index ≥ 2, and purple crosses indicate a Sérsic index < 2.

to the COLD GASS and ALFALFA-Hα galaxies, supporting the idea that they have quenched their star formation. Interestingly, at a given Σ_*, the $M_{\rm HI}/M_*$ values of spheroidal galaxies are independent of sSFR (Figure 2.16b), indicating that the dispersion in $t_{\rm dep}$ at the high Σ_* end is not the result of a wide range in H I content. Instead, the low sSFR galaxies appear unable to use their H I efficiently. In terms of absolute $M_{\rm HI}$, galaxies with the highest H I masses tend to live just below the quenching threshold (Figure 2.16c); galaxies with higher Σ_* must have lost or consumed their H I gas during the quenching process. The lack of a trend with bulge-to-disk ratio or $M_{\rm HI}/M_*$ among the quenched galaxies suggests that the spatial distribution of H I gas may account for their variation in SFE.

While the spheroidal galaxies exhibit the highest $t_{\rm dep}$ for their Σ_*, starbursts have low $t_{\rm dep}$ relative to galaxies of a similar M_* or Σ_* (Figures 2.13-2.16). Many studies have pointed out the role mergers may play in enhancing SFE (e.g., Solomon & Sage, 1988; Combes et al., 1994; Bouché et al., 2007; Di Matteo et al., 2007; Bournaud et al., 2011). Turbulence and gas flows during major mergers can lead to the efficient formation of molecular gas, shifting the ISM gas distribution to higher densities (Bournaud et al., 2011; Powell et al., 2013). During a gas-rich merger, the total gas fraction of a galaxy may increase due to the addition of new gas; however, if the distribution of gas becomes skewed to higher gas densities, the H_2 gas fraction may increase more strongly than the H I gas fraction. This scenario could potentially explain the moderately high H I gas fractions and short $t_{\rm dep}$ of the ALFALFA-Hα starbursts.

2.3.3 Morphology and Mergers

The starbursts' morphologies and kinematics may demonstrate whether dynamical disturbances are enhancing the SFE. One measure of morphological disturbance is the 180° rotational asymmetry. We calculate the R-band asymmetry, A_R, following

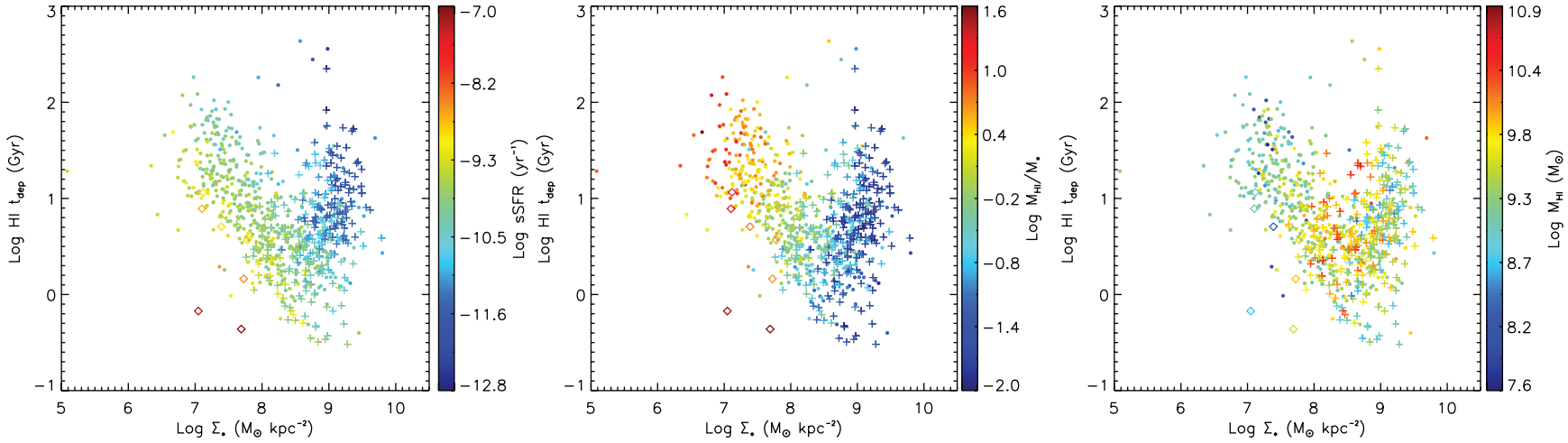

Figure 2.16: $t_{\rm dep}$ as a function of Σ_* for the ALFALFA-Hα non-starbursts (circles) and starbursts (diamonds) and the COLD GASS sample (crosses). Color indicates sSFR (left panel), $M_{\rm HI}/M_*$ (center panel), and $M_{\rm HI}$ (right panel).

Conselice et al. (2000b), as

$$A_R = \min(\frac{\sum |I_0 - I_{180}|}{\sum |I_0|}) - \min(\frac{\sum |B_0 - B_{180}|}{\sum |I_0|}), \quad (2.8)$$

where I_0 is the original image, I_{180} is the image rotated by 180°, B_0 is a background region, and B_{180} is a background region rotated by 180°. We sum over all the image pixels within the Petrosian radius (Petrosian, 1976) at the $\eta = 0.2$ surface brightness level, and we scale the background region to the same size. The minimization finds the rotational center that produces the lowest asymmetry value. Prior to the calculation, all images are background-subtracted, and we mask all stars within approximately five galaxy radii using the IRAF[6] task `imedit`. As recommended by Conselice et al. (2000b), we adopt a signal-to-noise (S/N) cut of 100. Below this value, the scatter in A_R dramatically increases and 41% of the ALFALFA-Hα galaxies have unphysical negative A_R values.

We show images of the eight ALFALFA-Hα starbursts and their calculated asymmetries in Figure 2.17 and list the asymmetry values in Table 2.1. The five starbursts with S/N > 100 have asymmetries ranging from 0.18-0.68, higher than the median sample asymmetry of 0.14. Conselice (2003) suggests that asymmetries above ∼0.35 may indicate major mergers. Figure 2.18 shows the asymmetries of the sample as a function of Hα EW. All the starbursts have slightly elevated asymmetries, and two (AGC 330517 and AGC 330500) are clearly major mergers. However, we find equally disturbed galaxies at lower values of Hα EW, indicating that not all the H I-rich mergers are starbursts.

If the starbursts are merging systems, they appear to be near coalescence. Simulations of major mergers also indicate that the peak star formation activity should occur at this time (e.g., Mihos & Hernquist, 1994; Cox et al., 2008; Lotz et al., 2010b).

[6]IRAF is distributed by the National Optical Astronomy Observatories, which are operated by the Association of Universities for Research in Astronomy, Inc., under cooperative agreement with the National Science Foundation.

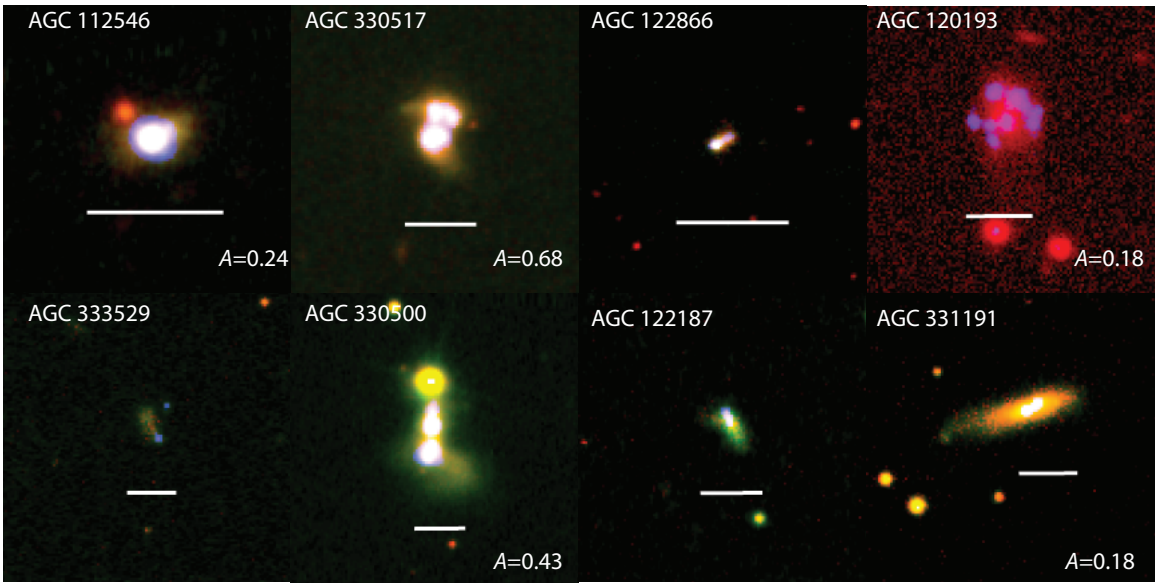

Figure 2.17: Morphologies of the eight ALFALFA-Hα starbursts, organized in order of Hα EW (see Table 2.1). The highest EW starburst is at the upper left, and the lowest EW starburst is at the lower right. The ALFALFA-Hα R-band images appear in red, SDSS g-band images appear in green, and the continuum-subtracted Hα emission is shown in blue. All images have a logarithmic brightness scale. AGC 120193 does not have SDSS images. The solid white line in each panel corresponds to 5 kpc. The R-band asymmetries are indicated for the five starbursts with S/N$>$ 100. The yellow region above AGC 330500 is a bright star.

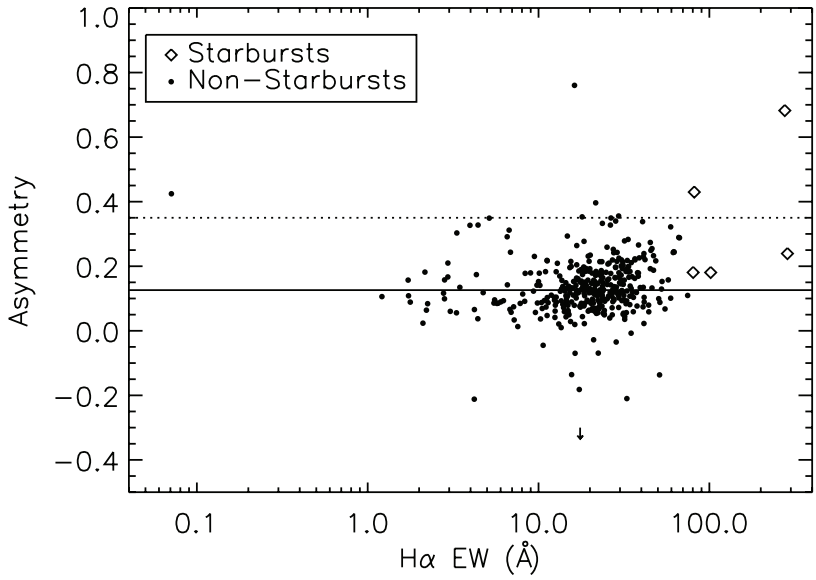

Figure 2.18: The R-band asymmetries and Hα EWs for galaxies with S/N$>$ 100. The solid line shows the median asymmetry and the dotted line shows the $A_R > 0.35$ criterion for identifying major mergers. The downward arrow indicates an outlier with unphysical negative asymmetry.

The two most asymmetric starbursts, AGC 330517 and AGC 330500, are also the starbursts with the highest offsets from the H I gas fraction and stellar mass relation for the sample (see Figure 2.6). High gas-fraction mergers experience more extended star formation, which causes them to appear asymmetric over a longer timescale (Lotz et al., 2010a). Alternatively, these two starbursts may be in an earlier merger stage than the other starbursts, prior to coalescence, when they have not yet consumed or expelled much of their H I gas. The individual merging galaxies in AGC 330517 and AGC 330500 are still distinguishable in Figure 2.17, which supports this possibility. The other three starbursts with asymmetry measurements have $A_R \sim 0.2$, only slightly higher than the average asymmetry of the full sample. These lower asymmetries could simply reflect the clumpy star formation in these galaxies, or they could indicate a mild dynamical disturbance. The asymmetries could also be consistent with a later merger stage; the simulations of Lotz et al. (2010b) show that the peak star formation in major mergers may occur a few hundred Myr after the peak

asymmetry. Mild asymmetries of $A_R \sim 0.2$ correspond to this peak star-forming, coalescence stage. The asymmetries of the starbursts suggest that dynamical disturbances are triggering the efficient conversion of H I into H_2 throughout the merger. Earlier stage mergers may still exhibit excess H I, which is consumed or ionized by the end of the starburst phase.

Disturbed gas kinematics may also be a sign of galaxy interactions. The H I velocity profiles of merging galaxies often exhibit asymmetries or wide, high-velocity wings due to an excess of high-velocity gas (e.g., Gallagher et al., 1981; Mirabel & Sanders, 1988). To quantify this high-velocity excess, we calculate the ratio of the H I velocity width at 20% of the peak flux to the width at 50% of the peak, W_{20}/W_{50}, as suggested by Conselice et al. (2000a). Since the ALFALFA velocity resolution is 10 $\mathrm{km\,s^{-1}}$, we calculate an upper limit to W_{20}/W_{50} for galaxies with $W_{20}/2 - W_{50}/2 < 10$ $\mathrm{km\,s^{-1}}$. We show the H I width ratios and Hα EWs of the sample in Figure 2.19 and Table 2.1. All of the starbursts have H I width ratios greater than the sample median, although as with morphological asymmetry, high H I width ratios occur in non-starbursts as well. In simulations of merging galaxies, Powell et al. (2013) find that interaction-driven turbulence, rather than supernova feedback, creates the high gas velocity dispersions observed in mergers. They argue that this enhanced turbulence increases the SFR by shifting the gas distribution to higher densities. The observed H I gas disturbances are therefore a possible cause of the high star formation efficiencies in the starbursts.

Non-interacting dwarf galaxies may also show broad wings in their H I profiles, however, and the high W_{20}/W_{50} ratios of the starbursts do not necessarily prove they are interacting (e.g., Gallagher et al., 1981). We display the H I velocity profiles of the starbursts in Figure 2.20. While the H I profiles of several starbursts appear broad or irregular, the profiles of some of the lower-mass starbursts, especially AGC 112546 and AGC 122866, appear quite narrow and only have upper limits on W_{20}/W_{50}. For comparison, we show examples of non-starburst H I profiles in Figure 2.21. For

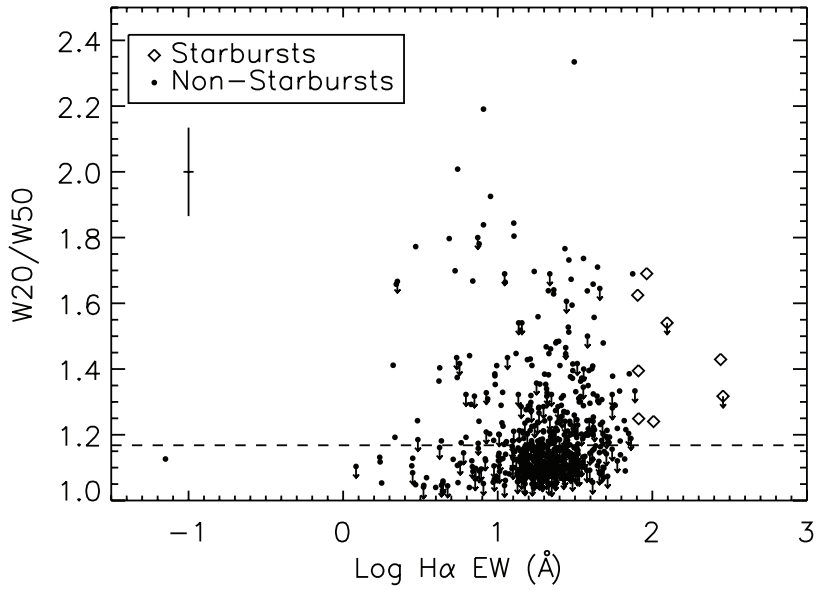

Figure 2.19: H I velocity width ratios, W_{20}/W_{50}, and Hα EWs of the ALFALFA-Hα sample. The dashed line shows the median W_{20}/W_{50}; this median includes galaxies with only upper limits on W_{20}/W_{50}, and therefore may be overestimated. The starbursts tend to have higher than average H I width ratios. Representative error bars are shown at the upper left of the plot.

each starburst, we randomly selected a non-starburst counterpart with M_* within 0.5 dex and with a similar S/N H I spectrum. Since one starburst, AGC 120193, does not have SDSS photometry, we selected a non-starburst with $M_{\rm HI}$ within 0.5 dex. The H I velocity profiles of the four most massive starbursts, AGC 330517, AGC 120193, AGC 330500, and AGC 331191, do appear to have broader wings than the straight-sided profiles of the non-starbursts. However, the profiles of the four lower mass starbursts ($M_* < 10^8\,{\rm M}_\odot$) are indistinguishable from non-starburst profiles of similar mass galaxies. We caution that the resolution of the H I spectra may be too low to accurately probe the profile shapes of these galaxies. Nevertheless, as discussed in § 2.3.1.1, the low mass starbursts also have H I gas fractions comparable to those of low mass non-starbursts. Their global H I gas may therefore be unrelated to their star formation. Infalling gas clouds are one possible trigger of star formation in dwarf galaxies (e.g., Gordon & Gottesman, 1981; López-Sánchez et al., 2012b;

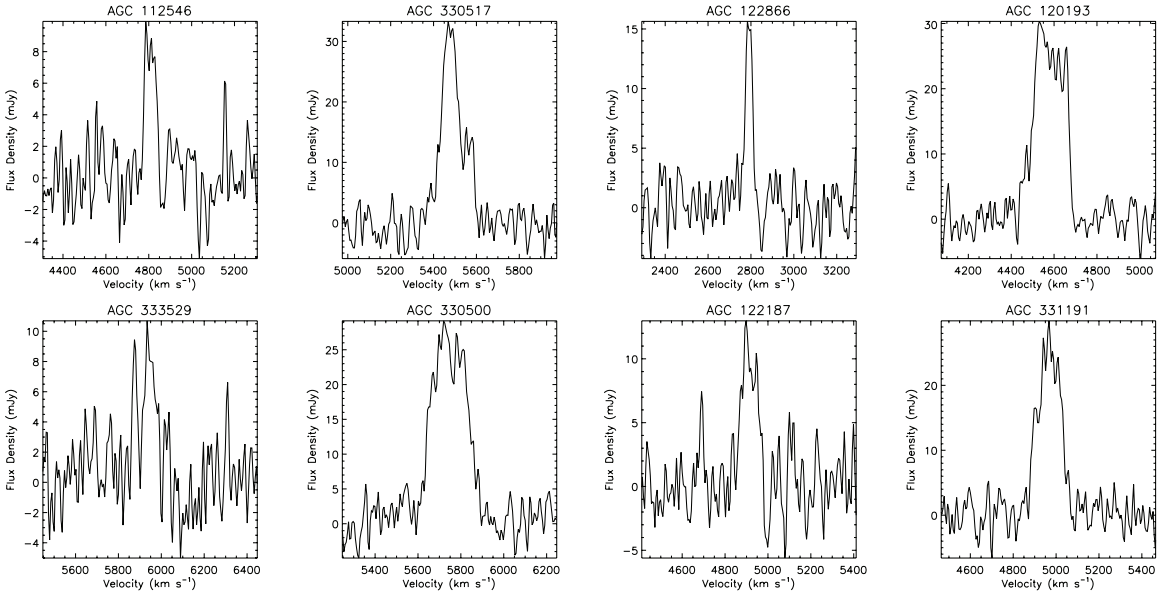

Figure 2.20: The H I velocity profiles of the starbursts, ordered as in Figure 2.17.

Verbeke et al., 2014). Verbeke et al. (2014) show that this type of interaction may generate multiple starburst episodes; disturbed gas kinematics may only be observable during the initial starburst and with favorable viewing orientations. These low-mass starbursts may therefore no longer show H I disturbances and may have consumed some of their H I during a prior burst.

Although the traditional picture of merger-driven star formation emphasizes nuclear starbursts, recent studies have suggested that mergers may also cause a substantial increase in extended star formation (e.g., Ellison et al., 2013; Powell et al., 2013). In Figure 2.22, we show the fraction of star formation within R_{50} for starbursts and non-starbursts. We only include galaxies with a S/N$>$ 10 in the Hα image. Three starbursts (AGC 112546, AGC 122866, and AGC 331191) show highly concentrated star formation, with more than 80% of their Hα emission contained within R_{50}. However, other starbursts, particularly AGC 120193 and AGC 333529, show H II regions offset from the main R-band center of the galaxy. The majority of the star formation in these two starbursts is outside R_{50}. Gas flows in starbursts fuel nuclear star

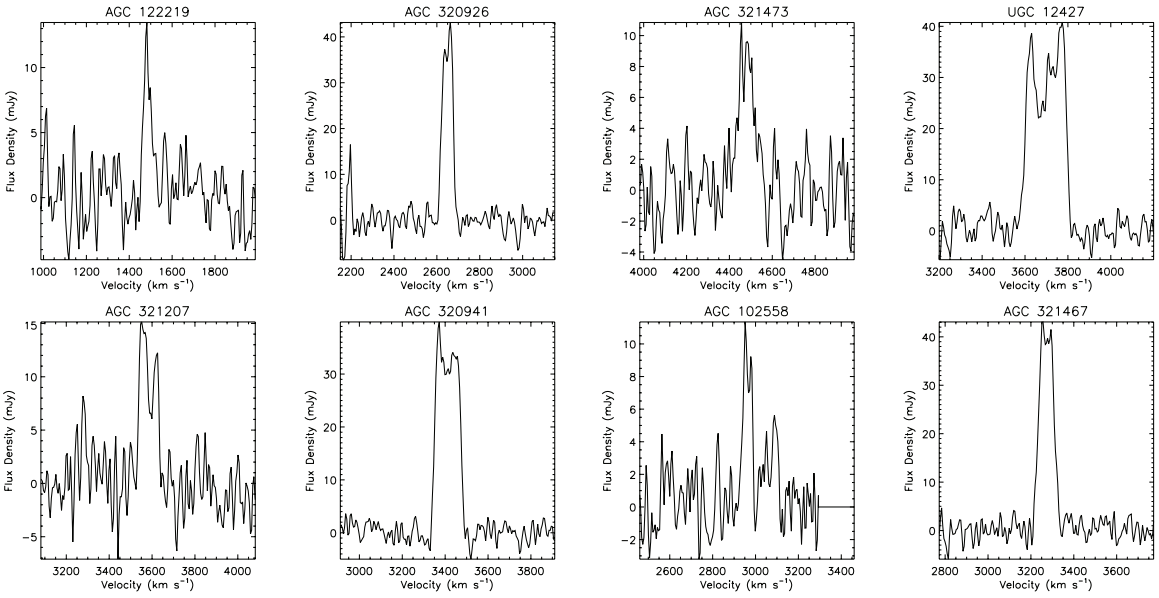

Figure 2.21: The H I velocity profiles of eight non-starbursts, selected to have similar stellar masses and S/N spectra as the corresponding starbursts in Figure 2.20. Since one starburst (AGC 120193) does not have a stellar mass estimate, we select the corresponding galaxy (UGC 12427) on the basis of H I mass. The double-peaked profile of UGC 12427 is typical of spiral galaxies.

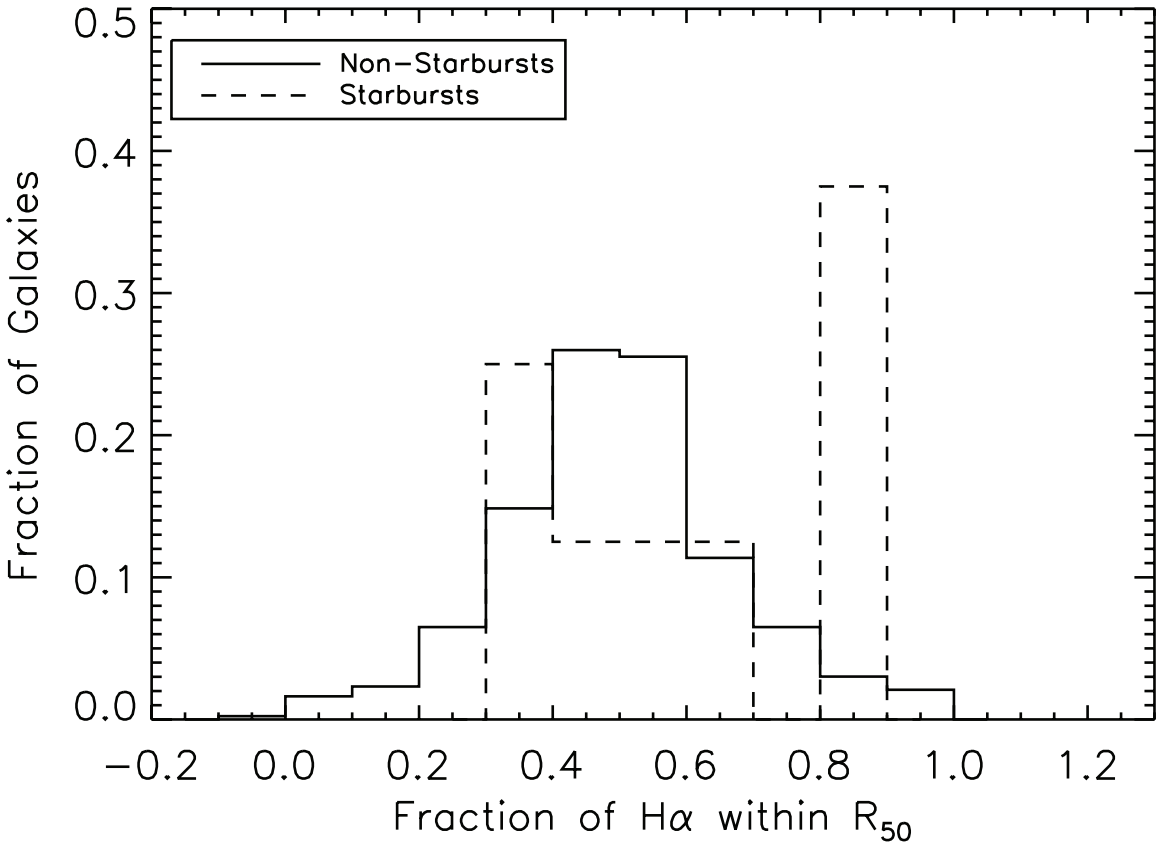

Figure 2.22: The fraction of Hα emission within the R-band half-light radius for non-starbursts (solid lines) and starbursts (dashed lines). Only galaxies with an Hα S/N$>$ 10 are shown.

formation in many, but not all, cases.

The starbursts generally appear more morphologically and kinematically disturbed than gas-rich non-starbursts. These disturbances may allow the starbursts to use their H I gas more efficiently by triggering H I inflows that raise the gas column density. Several of the starbursts appear to be major mergers near coalescence. The evidence for interaction is less clear among the lower mass starbursts; these galaxies may be experiencing periodic starbursts, possibly due to previous interactions with H I gas clouds. The low potential wells of these starbursts may contribute to cyclical bursts (e.g., Lee et al., 2007; Verbeke et al., 2014). By expelling the inner gas, supernova feedback may temporarily quench the starburst. This gas may later fall back onto the

galaxy to trigger a later starburst. The large H I gas fractions of the dwarf starbursts provide a plentiful neutral gas supply capable of fueling multiple starburst episodes.

The balance between infall and feedback may lead to a relatively stable H I supply in gas-rich starbursts. Addition of H I gas through interaction with a gas cloud or gas-rich galaxy may initially raise the H I gas fraction. This excess H I quickly disappears, however, as gas compression or turbulence resulting from these interactions efficiently converts the H I gas to H_2 and stars. As the starburst progresses, the H I gas fraction may stabilize instead of continuing its decrease. The starburst may not affect H I gas in the outer galaxy, and photodissociation of molecular gas may replenish H I in the inner regions. Indeed, previous observations have demonstrated that photodissociated gas may be a significant component of the ISM in the inner regions of starburst galaxies (e.g., Stacey et al., 1991). Radiative feedback does not appear sufficient to deplete the H I gas in the starbursts through ionization, and the starbursts with the highest ratios of Hα luminosity to H I mass (i.e., the shortest $t_{\rm dep}$) also show the highest H I gas fractions. After the starburst, the remaining H I reservoir may continue to fuel star formation, or additional feedback mechanisms, such as supernovae, may ultimately quench the burst.

2.4 Conclusion

The ALFALFA-Hα survey illuminates the roles of gas accretion and feedback in determining the H I content of starburst galaxies and in triggering and sustaining star formation. We use Hα EW to identify eight starbursts within the 565 galaxies of the fall-sky ALFALFA-Hα sample, a volume-limited subset of the H I-selected ALFALFA survey. With this statistical, H I-selected sample we compare the properties of gas-rich starbursts and non-starbursts.

We find that gas-rich starbursts are able to maintain a relatively constant H I supply. Most of the eight starbursts show little to no increase in $M_{\rm HI}/M_*$ relative to

galaxies of a similar mass, which suggests that by the time of the starburst episode, any excess atomic gas has already been converted into H_2. Starbursts that appear to be in a pre-coalescent merger stage do show some evidence for enhanced H I gas fractions, indicating that the conversion of excess H I to H_2 is not yet complete. These two starbursts have the most asymmetric optical morphologies and show the largest deviations from the main $M_{\rm HI}/M_*$ vs. M_* relation for the sample. Their high H I gas fractions may indicate that H I-to-H_2 conversion is an ongoing process during mergers.

As star formation continues, the H I gas fraction may stabilize, with photodissociation of H_2 likely compensating for decreases in H I due to consumption and ionization. Although we do not find that starbursts are unusually H I-rich, we also do not find that starbursts are H I-deficient, as suggested for starbursts in the SINGG sample (Oey et al., 2007). The trend of lower $M_{\rm HI}/L_R$ in higher SFI galaxies results from the lower M_*/L_R ratios of the starbursts, rather than low $M_{\rm HI}$ values, and high SFI galaxies span a wide range of H I gas fractions. Ionization does not appear to substantially deplete the starbursts' H I gas. In fact, the starbursts with the highest ratios of Hα luminosity to H I mass also have the highest H I gas fractions. The similarity of the H I gas fractions of starbursts and non-starbursts may indicate that the intense ionizing radiation of the starbursts does not penetrate to the outermost regions hosting much of the H I mass. Near the starburst, photodissociation of molecular gas may largely balance photoionization of H I.

On average, ALFALFA-Hα galaxies with higher instantaneous sSFRs tend to have higher H I gas fractions, but this trend shows substantial scatter. In contrast, we observe a tight trend between H I gas fraction and $g-r$ color. However, this correlation does not reflect a connection between H I content and the SFR averaged over long timescales, but rather an anticorrelation between dust extinction and H I gas fraction. Massive, star-forming galaxies with low H I gas fractions tend to have higher dust-to-gas ratios and hence, redder colors, leading to the observed trend.

In examining the factors that enhance the SFE of galaxies, we find that disk galaxies lie on a sequence of decreasing H I depletion time with increasing stellar surface density. The observed trend is consistent with the idea that higher midplane pressures encourage the formation of H_2 from H I (Blitz & Rosolowsky, 2006). Disk galaxies from the COLD GASS sample (Saintonge et al., 2011a,b) also fall on this sequence, while spheroid-dominated systems are offset to higher $t_{\rm dep}$. The spread in the H I depletion times of the spheroids reflects a spread in sSFR, but shows no trend with either H I gas fraction or bulge-to-disk ratio. Instead, the spatial distribution of H I in early-type galaxies likely determines whether gas clouds can reach the necessary densities to form molecular gas.

The starbursts appear to be more efficient star-formers than the rest of the sample, as indicated by their lower H I depletion times. Major mergers may cause these high efficiencies, as suggested by the starbursts' asymmetric optical morphologies and wide H I velocity profile wings. The asymmetries and morphologies of the starbursts are consistent with mergers near coalescence, the merger phase predicted to cause the largest enhancement in SFR. Finally, consistent with recent merger simulations (e.g., Powell et al., 2013), we find that extended, rather than nuclear, star formation may dominate the morphologies of some starbursts.

While some of the starbursts are clear mergers, major mergers may not cause the high SFEs of the lowest mass starbursts. The lowest mass starbursts do not show more disturbed H I kinematics than other dwarf galaxies, which may suggest a different mechanism is driving their star formation. These dwarf starbursts may undergo periodic bursts, possibly triggered by interactions with a gas cloud, in which case unusual gas kinematics might not be apparent (Verbeke et al., 2014). Large fluctuations in SFR appear characteristic of dwarf galaxies (e.g., Lee et al., 2007), and the dwarf galaxies in our sample also show a larger scatter in SFE than more massive galaxies. Starbursts in dwarf galaxies may therefore represent a recurrent mode of star

formation, whereas the more massive starbursts are unusual, merger-driven events. The large, apparently sustainable H I gas fractions of the dwarf starbursts may provide ample fuel for multiple generations of starbursts.

Table 2.1: Properties of the ALFALFA-Hα Starbursts

ID	RA[a,b]	Dec[a,b]	Distance[b] (Mpc)	Hα EW (Å)	SFR ($M_\odot yr^{-1}$)	Log (M_{HI})[b] ($M_\odot$)	Log (M_*)[c] ($M_\odot$)	t_{dep} (Gyr)	A_R^d	W_{20}/W_{50}^a
AGC 112546	01:31:20.6	28:48:29	66.4	286.6±4.8	0.80±0.26	8.7±0.1	7.2±0.1	0.67±0.27	0.24	≤1.3
AGC 330517	23:32:04.7	28:57:21	78.4	276.4±4.8	9.5±3.6	9.6±0.1	8.0±0.1	0.44±0.19	0.68	1.4±0.4
AGC 122866	02:11:31.4	24:12:51	37.3	124.5±4.3	0.04±0.01	8.3±0.1	7.6±0.1	5.1±2.0	...	≤1.5
AGC 120193	02:22:55.0	25:18:53	62.7	101.9±2.0	1.0±0.3	9.6±0.1	...	4.4±1.7	0.18	1.2±0.2
AGC 333529	23:22:39.8	28:57:18	85.2	92.0±10.0	0.12±0.04	9.0±0.1	7.8±0.1	7.8±3.1	...	1.7±0.3
AGC 330500	23:30:10.0	25:32:01	82.2	81.6±1.3	5.7±2.6	9.9±0.1	9.3±0.1	1.5±0.7	0.43	1.2±0.1
AGC 122187	02:09:55.7	27:32:25	67.6	81.3±6.1	0.09±0.03	9.0±0.1	7.9±0.1	11.6±4.5	...	1.4±0.1
AGC 331191	23:28:48.9	24:52:10	71.2	80.4±2.3	1.0±0.3	9.6±0.1	9.0±0.1	3.7±1.4	0.18	1.6±0.3

[a]Coordinates of the detected H I source.
[b]Values from the ALFALFA catalog (Haynes et al., 2011).
[c]The errors listed include the statistical photometric errors and the 0.1 dex scatter in the M/L-color relation.
[d]R-band asymmetry.

CHAPTER III

The Origin and Optical Depth of Ionizing Radiation in Extreme Starbursts

3.1 Introduction

Radiative feedback from young stellar clusters has powerful effects on both the neutral interstellar medium (ISM) and intergalactic medium (IGM). In the early Universe, massive stars in star-forming galaxies likely produced most of the ionizing radiation responsible for reionization (e.g., Bolton et al., 2005; Bouwens et al., 2012; Fontanot et al., 2012). In addition, high-energy radiation from massive stars is a key component of galactic energy budgets and has important consequences for the neutral ISM. This radiation may suppress or trigger additional star formation (Elmegreen & Lada, 1977; Haiman et al., 1997) and may escape from H II regions to generate the diffuse, warm ionized medium (e.g., Reynolds, 1984; Oey & Kennicutt, 1997).

The fraction of ionizing radiation that escapes H II regions and galaxies and the ionizing spectra of massive stars are highly uncertain, however. Near the redshift of reionization, the low-mass galaxies that may contribute most of the ionizing radiation are unobservable (Finkelstein et al., 2012). Estimates of the galactic escape fraction necessary to sustain reionization range from $< 13\%$ to $\geq 50\%$, depending on the luminosity function and redshift assumed (Finkelstein et al., 2012). At low redshift,

observations of star-forming galaxies give upper limits on the escape fraction of only a few percent (e.g., Leitherer et al., 1995; Heckman et al., 2001; Siana et al., 2010). At intermediate redshift, the incidence of detected Lyman continuum radiation is rare (e.g., Steidel et al., 2001; Shapley et al., 2006) and made uncertain by possible low-redshift contamination (Vanzella et al., 2012). The intrinsic ionizing spectrum of massive stars is likewise poorly known at all redshifts. This uncertainty translates directly to uncertainties in H II region and galactic escape fractions (e.g., Shapley et al., 2006; Voges et al., 2008), nebular conditions, and star formation rates.

Nebular spectra can provide information on both the spectral shape of the incident UV radiation and the optical depth (e.g., Oey et al., 2000; Giammanco et al., 2005; Zastrow et al., 2013a), but these observations are still out of reach for most high redshift galaxies. Instead, many studies have focused on samples of low-redshift galaxies with properties similar to galaxies at high redshift. One such sample is the 'Green Pea' (GP) galaxies (Cardamone et al., 2009), a collection of rare emission-line galaxies at $z = 0.1 - 0.3$ identified in the Sloan Digital Sky Survey (SDSS) through their unusually strong [O III] λ5007 emission. In particular, due to their extremely high [O III]/[O II] ratios, which may indicate a deficit of low-ionization emission, the GPs are an ideal sample to search for optically thin galaxies. The 80 star-forming GPs resemble high-redshift galaxies through their low metallicities, low extinction, high UV luminosities, and enormous specific star formation rates (Cardamone et al., 2009; Izotov et al., 2011; Amorín et al., 2012a; Maseda et al., 2014). *Hubble Space Telescope (HST)* imaging of a handful of the GPs reveals clumpy morphologies and super star clusters (Cardamone et al., 2009), a common mode of star formation at high redshift (e.g., Cowie et al., 1995; Dickinson et al., 2003; Elmegreen et al., 2005). The GP sample therefore represents the best opportunity in the local Universe to study high redshift star-forming conditions and the escape of ionizing radiation.

The precise origin of the GPs' extreme [O III]/[O II] ratios is uncertain. One pos-

sibility is that the high ratios are the result of a high ionization parameter, U. At a given metallicity, [O III]/[O II] increases with U (e.g., Kewley & Dopita, 2002; Martín-Manjón et al., 2010). The dimensionless ionization parameter for photoionized gas is defined as

$$U \equiv \frac{Q}{4\pi n_{\rm H} r_0^2 c}, \tag{3.1}$$

where Q is the hydrogen-ionizing photon emission rate, $n_{\rm H}$ is the total hydrogen density, r_0 is the inner nebular radius, and c is the speed of light (Osterbrock & Ferland, 2006). As powerful starbursts, the GPs likely have compact star forming regions and a hard ionizing radiation field, which may act to increase their ionization parameters and explain their high [O III]/[O II] ratios. Alternatively, Giammanco et al. (2005) and Pellegrini et al. (2012) demonstrate that escaping ionizing radiation decreases the emission contribution of low-ionization species. This suppression would also act to increase the [O III]/[O II] ratios and would lead to overestimates of U. In this paper, we evaluate the possibility that a low optical depth contributes to the GPs' high observed [O III]/[O II] ratios. We specifically examine the GPs with the highest [O III]/[O II] ratios and consider whether extreme ionization parameters alone are sufficient to explain the observed ratios.

Several previous works have investigated the ionization conditions in the GPs. In addition to the GPs' powerful [O III] emission, Hawley (2012) identifies He II λ4686 emission in nine GPs, providing further evidence for high ionization conditions. The presence of He II λ4686 emission in the GPs may indicate that the GPs are in the middle of a short-lived phase dominated by emission from Wolf-Rayet (WR) stars (Hawley, 2012). Additional support for the WR scenario comes from observations by Amorín et al. (2012a), who find broad, WR stellar features in deep spectra of three GPs. However, given the small sample size, it is unclear whether these observations are characteristic of the other GPs.

Studies of the GPs and similar galaxies suggest that the GPs may indeed be opti-

cally thin. Intermediate redshift Lyα emitters (LAEs) have similar [O III]/[O II] ratios and metallicities to the GPs, and fits to the LAEs' spectra imply high escape fractions (Nakajima et al., 2013). The GP sample overlaps with other nearby samples of galaxies, selected on the basis of high Balmer line equivalent widths (Shim & Chary, 2013) or high UV surface brightness (Heckman et al., 2005). Studies of these samples also support a low optical depth. The sample of Hα emitters (HAEs) studied by Shim & Chary (2013) resemble WR galaxies in their UV properties and inferred ionization parameters, although the HAEs are younger and have lower metallicities than the WR galaxies. Shim & Chary (2013) propose that the high ionization parameters inferred in the HAEs may instead indicate a low optical depth and a high escape fraction of ionizing photons. This scenario has also been suggested by Overzier et al. (2009) for a sample of UV-bright Lyman Break Analogs (LBAs), which includes several of the GPs. The LBAs show enhanced [O III]/Hβ ratios, and many of the LBAs have unusually low ratios of Hα/UV (Overzier et al., 2009). Although a low optical depth could explain these properties, Overzier et al. (2009) conclude that an aged starburst ($>$ 10 Myr old), dominated by supernova heating, provides a better explanation for the observed spectral properties of the sample. Heckman et al. (2011) investigated the optically thin scenario by using *HST* observations of C II λ1335 to infer the optical depth of several LBAs, including one GP. Although the C II line in the GP is optically thin, Heckman et al. (2011) point out that the consistency between the galaxy's Hα, UV, and IR luminosities makes the optically thin hypothesis tenuous.

Thus, a variety of ionizing sources and optical depth scenarios may explain the ionization conditions in GP galaxies. In this paper, we consider in particular whether a low optical depth could explain the observed line ratios in the GPs with the highest [O III]/[O II] ratios. We select six extreme GPs from the (Cardamone et al., 2009) sample on the basis of their [O III]/[O II] ratios, as these galaxies are the most likely to be optically thin. We then compare nebular and stellar population models with the

observed line ratios in the six extreme GPs to evaluate the galaxies' optical depths and ionizing sources. We discuss the spectral line measurements and properties of the GPs in §3.2. In §3.3, we analyze the observed line ratios and evaluate the potential ionizing sources. We discuss the results and their consequences for the optical depth of the GPs in §4.3 and summarize our results in §3.5. We assume a cosmology with $H_0 = 70$ km s^{-1} Mpc^{-1}, $\Omega_m = 0.3$, and $\Lambda_0 = 0.7$ throughout.

3.2 Data and Measurements

The GPs are a subset of extreme, compact emission-line galaxies at redshifts between $z = 0.1$ and $z = 0.3$ (Izotov et al., 2011). Cardamone et al. (2009) identify a sample of 103 narrow-line GP galaxies in SDSS Data Release 7 (DR7) through color selection criteria and signal-to-noise (S/N) cuts. The color selection isolates galaxies whose $u - r$, $g - r$, $r - i$, and $r - z$ colors deviate from the normal SDSS galaxy and quasar population due to intense [O III] λ5007 emission in the r band (Cardamone et al., 2009). Using the Baldwin et al. (1981, BPT) diagram to separate active galactic nuclei (AGN) and star-forming galaxies, Cardamone et al. (2009) then identify a sample of 80 starbursting galaxies. Several of these starbursts have high [O III] $\lambda\lambda$5007,4959/[O II] λ3727 ratios, implying unusually high ionization parameters (e.g., Martín-Manjón et al., 2010). The GPs' [O III]/[O II] ratios raise the possibility that the galaxies may be optically thin to Lyman continuum radiation. A low optical depth would suppress the [O II] emission, consistent with the high observed [O III]/[O II] ratios. A less-extreme ionization parameter in combination with a low optical depth could therefore be an alternative explanation for the observed ratios.

We obtained spectra for the 80 starbursting GPs listed in Cardamone et al. (2009) from the SDSS DR7 (Abazajian et al., 2009). We then measured the fluxes and equivalent widths (EWs) of the galaxies' emission lines using the IRAF[1] task `splot`.

[1]IRAF is distributed by the National Optical Astronomy Observatories, which are operated by

As discussed by Amorín et al. (2012b), the GPs' emission line profiles have broad wings, indicating the presence of high velocity gas. When necessary, we deblended the Hα and [N II] lines using a Voigt profile fit, as a Gaussian fit did not capture the emission line wings. The [S II] $\lambda\lambda$6716 and 6731 lines were deblended with a Gaussian fit, if necessary. We calculated errors in the line measurements according to

$$\sigma_{\rm line} = \sigma_{\rm rms}\sqrt{N}, \tag{3.2}$$

where $\sigma_{\rm rms}$ is the average root-mean-square value per pixel measured at either side of the spectral line and N is the number of pixels in the line.

We simultaneously fit the measured ratios of Hα/Hβ, Hγ/Hβ, and Hδ/Hβ for both reddening and stellar absorption. We adopted intrinsic ratios of 2.86, 0.468, and 0.259, respectively (Storey & Hummer, 1995), which are appropriate for $n_{\rm H} = 100$ cm^{-3} and T_e=10,000 K. We then corrected the line fluxes for extinction using the Calzetti et al. (2000) reddening law. In many of the GPs, the [O III] $\lambda\lambda$5007,4959/λ4363 ratio indicates an electron temperature much higher than T_e=10,000 K. As a result, we re-fit the reddening and stellar absorption for these objects, using the Balmer line ratios at T_e=12,500 K or T_e=15,000 K from Storey & Hummer (1995). To estimate the appropriate temperature, we used the IRAF `temden` routine, assuming a density of 100 cm^{-3}. We used the errors in the Hα/Hβ ratios to estimate the uncertainties in the extinction correction. We further assumed an uncertainty of 0.04 in the intrinsic Hα/Hβ ratio, corresponding to the change in the ratio when T_e is varied by 2500 K. The intrinsic ratio is less sensitive to density; increasing the density by an order of magnitude changes the intrinsic Hα/Hβ ratio by only 0.01 or less, depending on the assumed temperature. We then added the reddening uncertainty in quadrature with the flux errors. As noted by Cardamone et al. (2009), the GPs generally have low

the Association of Universities for Research in Astronomy, Inc., under cooperative agreement with the National Science Foundation.

extinction, and our average extinction coefficient $c(\mathrm{H}\beta)= 0.27$. The stellar absorption values are also typically low, with a median absorption of 1.05 Å, indicating that the spectra are dominated by a young population.

While the GPs generally have high [O III]/[O II] ratios, two GPs (J133940.7+552740 and J094347.2+262043) actually have stronger [O II] emission than [O III]. Since we are investigating the causes of high [O III]/[O II] ratios in the GPs, we have excluded these objects from further analysis.

We select the six GPs with the highest [O III]/[O II] ratios for more detailed analysis (Figure 3.1). These extreme GPs have the greatest potential for a low optical depth or unusual ionizing source. Furthermore, five of these extreme GPs have detectable He II λ4686 emission, which improves our constraints on their ionizing sources (§3.3). Line strengths, errors, and EWs for the six extreme GPs, the GPs with the highest [O III]/[O II] ratios, are listed in Tables 3.2 and 3.2.

The GPs have high electron temperatures, as expected for low-metallicity objects. After correcting for reddening and stellar absorption as discussed above, we re-calculated the electron temperature. We then calculated the electron density from the observed [S II] λ6716/λ6731 ratio with `temden` and iterated until both temperature and density converged. The revised temperatures are still consistent with the temperatures assumed in the reddening calculations. Our calculated temperatures and densities and the metallicity measurements of Izotov et al. (2011) are listed in Table 3.3 for the extreme GPs. Izotov et al. (2011) determined abundances using the direct method, which calculates the oxygen abundance, given the observed [O III] and [O II] fluxes and the electron temperature derived from the [O III] (λ4959 + λ5007)/λ4363 ratio. Table 3.3 also lists the SFR, derived from the Hα luminosity according to

$$\log SFR = \log L(H\alpha) - 41.27, \tag{3.3}$$

where SFR is in units of $\mathrm{M}_{\odot}\mathrm{yr}^{-1}$ and $L(H\alpha)$ is in $\mathrm{ergs\,s}^{-1}$ (Kennicutt & Evans,

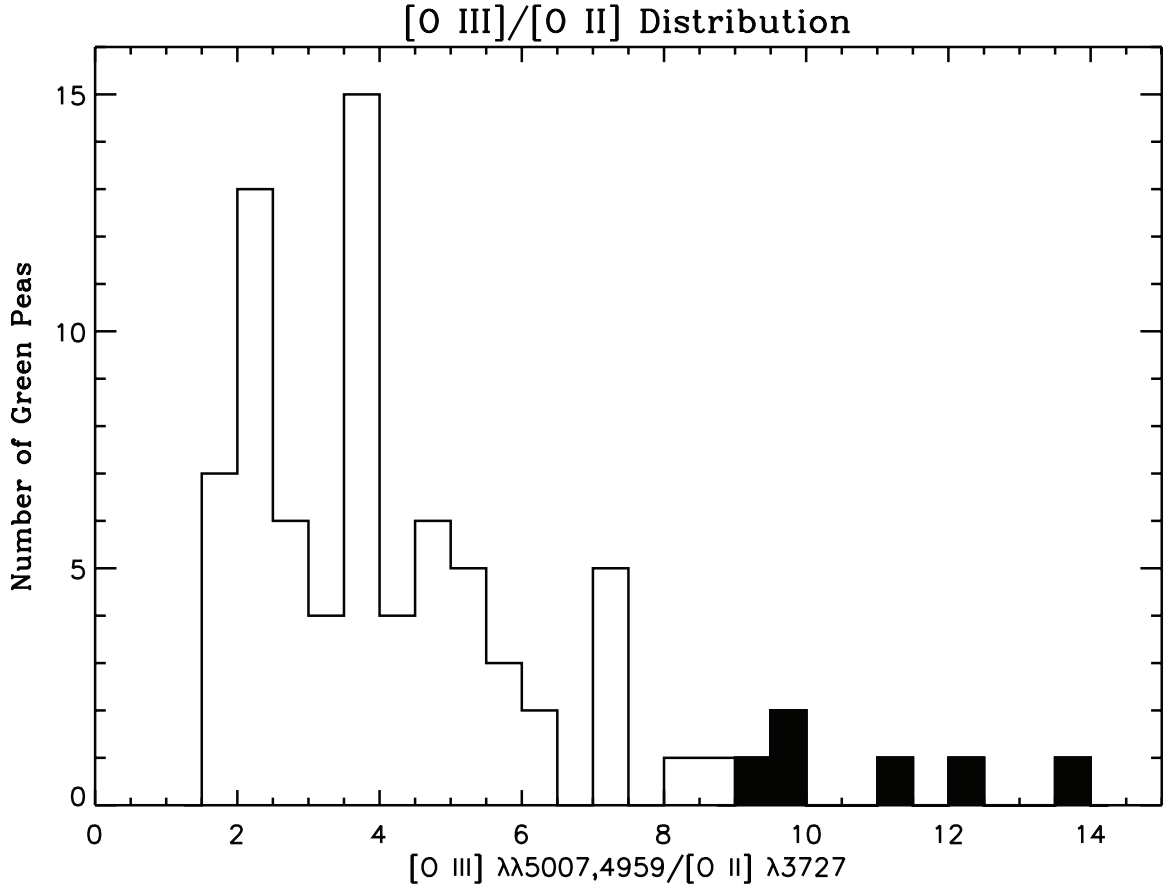

Figure 3.1: A histogram of the [O III] $\lambda\lambda 5007, 4959$/[O II] $\lambda 3727$ ratios in the GPs. The six extreme GPs are shown in black.

Table 3.1: Selected Emission-Line Intensities of the Extreme Green Peas

	J081552.00+215623.6		J121903.98+152608.5		J101157.08+130822.0	
Line	$F(\lambda)/F(\mathrm{H}\beta)$	$I(\lambda)/I(\mathrm{H}\beta)$	$F(\lambda)/F(\mathrm{H}\beta)$	$I(\lambda)/I(\mathrm{H}\beta)$	$F(\lambda)/F(\mathrm{H}\beta)$	$I(\lambda)/I(\mathrm{H}\beta)$
[O II] 3727	0.655 ± 0.010	0.698 ± 0.067	0.622 ± 0.006	0.703 ± 0.063	0.810 ± 0.008	0.872 ± 0.077
He I 3819	...	...	...	...	0.010 ± 0.002	0.010 ± 0.003
[Ne III] 3869	0.504 ± 0.009	0.532 ± 0.050	0.468 ± 0.006	0.520 ± 0.046	0.535 ± 0.006	0.569 ± 0.050
Hδ 4105	0.235 ± 0.007	0.244 ± 0.023	0.246 ± 0.004	0.266 ± 0.023	0.258 ± 0.004	0.270 ± 0.023
Hγ 4340	0.458 ± 0.008	0.468 ± 0.041	0.456 ± 0.005	0.479 ± 0.040	0.463 ± 0.005	0.477 ± 0.039
[O III] 4363	0.134 ± 0.006	0.136 ± 0.013	0.127 ± 0.003	0.133 ± 0.011	0.128 ± 0.003	0.131 ± 0.011
N III,C III 4640	...	...	...	...	0.015 ± 0.004	0.015 ± 0.004
[Fe III],C IV 4658	...	...	...	...	0.009 ± 0.003	0.009 ± 0.003
He II 4686	0.018 ± 0.005	0.018 ± 0.006	0.020 ± 0.003	0.020 ± 0.004	0.011 ± 0.003	0.011 ± 0.003
[Ar IV],He I 4713	0.030 ± 0.006	0.030 ± 0.006	0.019 ± 0.003	0.019 ± 0.003	0.015 ± 0.003	0.015 ± 0.003
[Ar IV] 4740	...	...	0.010 ± 0.003	0.010 ± 0.003	0.006 ± 0.002	0.007 ± 0.002
[O III] 4959	2.335 ± 0.018	2.300 ± 0.188	2.216 ± 0.011	2.197 ± 0.169	2.484 ± 0.012	2.471 ± 0.189
[O III] 5007	7.365 ± 0.053	7.235 ± 0.588	6.620 ± 0.028	6.535 ± 0.499	7.479 ± 0.033	7.420 ± 0.563
[N I] 5200	...	...	...	...	0.006 ± 0.002	0.006 ± 0.002
He I 5876	0.114 ± 0.004	0.107 ± 0.009	0.127 ± 0.003	0.117 ± 0.009	0.118 ± 0.003	0.113 ± 0.008
[O I] 6300	0.014 ± 0.004	0.013 ± 0.004	0.027 ± 0.004	0.025 ± 0.004	0.025 ± 0.002	0.023 ± 0.003
[N II] 6548	...	...	...	...	0.015 ± 0.003	0.014 ± 0.003
Hα 6563	3.031 ± 0.022	2.792 ± 0.201	3.162 ± 0.015	2.795 ± 0.189	3.012 ± 0.014	2.796 ± 0.188
[N II] 6584	0.049 ± 0.005	0.045 ± 0.006	0.077 ± 0.006	0.068 ± 0.007	0.068 ± 0.003	0.064 ± 0.005
[S II] 6716	0.083 ± 0.006	0.075 ± 0.008	0.059 ± 0.004	0.052 ± 0.005	0.070 ± 0.004	0.065 ± 0.006
[S II] 6731	0.057 ± 0.006	0.052 ± 0.007	0.066 ± 0.004	0.058 ± 0.005	0.062 ± 0.004	0.057 ± 0.005
[Ar III] 7135	0.081 ± 0.008	0.073 ± 0.009	0.050 ± 0.007	0.043 ± 0.007	0.061 ± 0.006	0.056 ± 0.006
$c(\mathrm{H}\beta)$ dex	0.12		0.19		0.12	
$F(\mathrm{H}\beta)^a$	4.61 ± 0.03	6.10 ± 0.35	8.11 ± 0.03	12.67 ± 0.69	8.73 ± 0.04	11.42 ± 0.62
EW(abs)^{b}Å	2.23		0.00		0.00	
EW(Hβ)Å	224.0		246.7		334.6	
EW(Hα)Å	964.0		1559.0		1772.0	

The first 22 rows list the fluxes relative to Hβ for the designated emission lines. For each object, we list the observed fluxes ($F(\lambda)$) and the fluxes corrected for reddening and stellar absorption ($I(\lambda)$).

[a]We list both the observed flux and the flux corrected for reddening and stellar absorption. Fluxes are in 10^{-15} erg s^{-1} cm^{-2}.

[b]Best-fit stellar absorption equivalent width.

[c]Includes nebular [Fe III] λ4658 emission and broad C IV emission.

Table 3.2: Selected Emission-Line Intensities of the Extreme Green Peas (Continued)

	J145735.13+223201.8		J100918.99+291621.5		J030321.4-075923	
Line	$F(\lambda)/F(\mathrm{H}\beta)$	$I(\lambda)/I(\mathrm{H}\beta)$	$F(\lambda)/F(\mathrm{H}\beta)$	$I(\lambda)/I(\mathrm{H}\beta)$	$F(\lambda)/F(\mathrm{H}\beta)$	$I(\lambda)/I(\mathrm{H}\beta)$
[O II] 3727	0.869 ± 0.005	0.986 ± 0.086	0.825 ± 0.019	0.930 ± 0.118	0.807 ± 0.008	0.836 ± 0.077
He I 3819	0.016 ± 0.003	0.018 ± 0.003	...	...	...	...
[Ne III] 3869	0.511 ± 0.004	0.569 ± 0.049	0.544 ± 0.017	0.603 ± 0.076	0.376 ± 0.006	0.386 ± 0.035
Hδ 4105	0.241 ± 0.003	0.260 ± 0.022	0.267 ± 0.011	0.288 ± 0.036	0.218 ± 0.004	0.221 ± 0.020
Hγ 4340	0.438 ± 0.003	0.461 ± 0.037	0.475 ± 0.014	0.500 ± 0.059	0.426 ± 0.005	0.423 ± 0.018
[O III] 4363	0.115 ± 0.003	0.120 ± 0.010	0.124 ± 0.010	0.130 ± 0.019	0.115 ± 0.004	0.115 ± 0.010
N III,C III 4640	...	...	...	...	...	...
[Fe III],C IV 4658	0.010 ± 0.003	0.011 ± 0.003	...	...	0.032[c] ± 0.005	0.031[c] ± 0.006
He II 4686	0.007 ± 0.002	0.008 ± 0.002	...	...	0.013 ± 0.003	0.012 ± 0.003
[Ar IV],He I 4713	0.021 ± 0.003	0.022 ± 0.003	...	...	0.017 ± 0.003	0.017 ± 0.003
[Ar IV] 4740	0.013 ± 0.003	0.013 ± 0.003	...	...	...	...
[O III] 4959	2.449 ± 0.010	2.417 ± 0.182	2.236 ± 0.032	2.216 ± 0.241	2.001 ± 0.013	1.927 ± 0.152
[O III] 5007	7.392 ± 0.028	7.264 ± 0.545	6.765 ± 0.090	6.679 ± 0.722	6.168 ± 0.035	5.926 ± 0.464
[N I] 5200	...	...	...	...	...	...
He I 5876	0.127 ± 0.002	0.116 ± 0.008	0.131 ± 0.010	0.121 ± 0.015	0.114 ± 0.004	0.105 ± 0.008
[O I] 6300	0.034 ± 0.002	0.030 ± 0.003	...	...	0.016 ± 0.004	0.015 ± 0.004
[N II] 6548	0.018 ± 0.005	0.016 ± 0.004	...	...	...	...
Hα 6563	3.189 ± 0.013	2.787 ± 0.185	3.193 ± 0.050	2.828 ± 0.272	3.064 ± 0.020	2.786 ± 0.192
[N II] 6584	0.069 ± 0.004	0.060 ± 0.005	0.112 ± 0.024	0.099 ± 0.023	0.078 ± 0.009	0.071 ± 0.009
[S II] 6716	0.097 ± 0.004	0.084 ± 0.007	0.132 ± 0.018	0.116 ± 0.019	0.063 ± 0.010	0.056 ± 0.010
[S II] 6731	0.077 ± 0.004	0.067 ± 0.005	0.079 ± 0.016	0.069 ± 0.015	0.052 ± 0.010	0.047 ± 0.009
[Ar III] 7135	0.058 ± 0.004	0.049 ± 0.005	0.116 ± 0.031	0.099 ± 0.028	0.044 ± 0.016	0.039 ± 0.014
$c(\mathrm{H}\beta)$	0.21		0.19		0.11	
$F(\mathrm{H}\beta)$[a]	9.06 ± 0.03	14.63 ± 0.79	1.74 ± 0.02	2.70 ± 0.21	6.71 ± 0.04	8.87 ± 0.49
EW(abs)[b]Å	0.84		0.00		4.67	
EW(Hβ)Å	228.6		184.9		140.5	
EW(Hα)Å	1158.0		1086.0		812.5	

The first 22 rows list the fluxes relative to Hβ for the designated emission lines. For each object, we list the observed fluxes ($F(\lambda)$) and the fluxes corrected for reddening and stellar absorption ($I(\lambda)$).

[a]We list both the observed flux and the flux corrected for reddening and stellar absorption. Fluxes are in 10^{-15} erg s^{-1} cm^{-2}.

[b]Best-fit stellar absorption equivalent width.

[c]Includes nebular [Fe III] λ4658 emission and broad C IV emission.

Table 3.3: Properties of the Extreme GPs

SDSS ID	z[a]	[O III] λλ4959, 5007/λ4363	[S II] λ6716/λ6731	T_e (K)	n_e (cm^{-3})	Z^b ($Z_\odot$)	SFR[c] ($M_\odot yr^{-1}$)
J0816+22	0.1410	69.901 ± 6.295	1.439[d] ± 0.204	15069[e]	≤206[f]	0.204	4.9 ± 0.2
J1219+15	0.1957	65.473 ± 5.145	0.897 ± 0.096	15507	1088	0.158	21.0 ± 0.8
J1012+13	0.1439	75.320 ± 5.886	1.132 ± 0.110	14566	378	0.209	9.6 ± 0.4
J1457+22	0.1488	80.505 ± 6.121	1.259 ± 0.108	14156	171	0.224	13.2 ± 0.5
J1009+29	0.2219	68.501 ± 9.140	1.680[d] ± 0.433	15209[e]	≤189[f]	0.166	6.0 ± 0.3
J0303-08	0.1650	68.502 ± 5.778	1.193 ± 0.301	15204	272	0.148	10.1 ± 0.4

[a] From SDSS DR7.
[b] From Izotov et al. (2011). We assume a solar metallicity of 12+log(O/H)=8.69 (Allende Prieto et al., 2001).
[c] Using the conversion from Hα luminosity given in Kennicutt & Evans (2012).
[d] The [S II] ratio is at the low-density limit, and we are unable to determine a density.
[e] Calculated assuming a density of 100 cm^{-3}.
[f] The upper limit is calculated from the 1σ errors for the measured [S II] ratio.

2012). Our SFRs are higher than the ones found for these objects by Cardamone et al. (2009), despite our use of the Kennicutt & Evans (2012) relation, which leads to lower SFRs relative to the Kennicutt (1998b) relation. Due to our different treatment of reddening, we find Hα luminosities for the extreme GPs that are typically a factor of 2 greater than found by Cardamone et al. (2009). Cardamone et al. (2009) assume an intrinsic Hα/Hβ ratio appropriate for $T_e = 10^4$ K for all the GPs, whereas the six extreme GPs have temperatures of ∼15000 K (Table 3.3). In addition, Cardamone et al. (2009) use the Cardelli et al. (1989) reddening law, instead of the Calzetti et al. (2000) law we assume.

As evident in Table 3.3, the extreme GPs have an average metallicity near $0.2\,Z_\odot$. At metallicities $Z \leq 0.2\,Z_\odot$, temperature gradients in nebulae can cause the direct method to under- or over-estimate metallicities by 0.2-0.5 dex (López-Sánchez et al., 2012a). [O II] temperature estimates are necessary to correct for this effect, but unfortunately, the [O II] λλ7319 and 7330 lines are dominated by noise in the SDSS spectra. This metallicity uncertainty should be kept in mind for the extreme GPs J1219+15, J1009+29, and J0303-08, which have metallicities $< 0.2\,Z_\odot$.

To identify weak lines in the GPs' spectra, we created stacked spectra for several subsets of the GPs. We first corrected the spectra for redshift using the IRAF task `dopcor`. We then normalized the spectra to the mean flux in the 4200-4300 Å

range, which is free of strong spectral lines. As a check, we also created stacked spectra using the SDSS continuum-subtracted spectra and no normalization. These additional spectra had a flat continuum, making the hydrogen absorption lines more easily visible. Aside from this difference, using the continuum-subtracted spectra does not change our results. Following the normalization, we re-binned the spectra to a dispersion of 1 Å/pixel and averaged the spectra, rejecting pixels that deviated by more than 5σ from the median. We created stacked spectra for the full sample of 78 star-forming GPs with [O III] λ5007 >[O II] λ3727 and for a subset of 53 GPs with the strongest [O III] emission. Although our analysis focuses on the six extreme GPs, we created an additional stacked spectrum of the 15 highest [O III]/[O II] ratio GPs to improve the S/N.

3.2.1 Equivalent Widths and Age Constraints

Although several studies have proposed an 'aged starburst' hypothesis to explain the high ionization conditions in the GPs and similar galaxies (e.g., Overzier et al., 2009), a number of spectral features suggest younger ages for the starbursts, particularly the starbursts in the highest ionization GPs. Tables 3.4 and 3.5 compare the EWs and corresponding age estimates for the extreme GPs. The Balmer line EWs are large; the full sample of 78 GPs has an average redshift-corrected Hα EW of 607 Å, while the high-ionization GPs in Table 3.4 have Hα EWs $\sim$100-1000 Å greater than this average. To estimate the GPs' ages, we ran Starburst99 models (Leitherer et al., 1999) at $Z = 0.2\,Z_{\odot}$ for a $10^6\,M_{\odot}$ instantaneous burst and for continuous star formation with the SFRs in Table 3.3. We used a Kroupa (2001) initial mass function from 0.1-150 $M_{\odot}$, the Padova evolutionary tracks and mass-loss rates with AGB stars (Vázquez & Leitherer, 2005), and the Pauldrach et al. (2001) and Hillier & Miller (1998) stellar atmospheres. For the GPs' Hα EWs, the instantaneous burst model places upper limits on the burst ages of 4.2-5.1 Myr (Table 3.4). The Hβ EWs sug-

gest slightly younger burst ages, with upper limits of 3.7-4.9 Myr. These latter values may be more reliable due to the low continuum levels in the Hα spectral region and blending with the [N II] lines. We note, however, that both the Hβ and Hα EWs give similar ages.

An additional indication of young ages for the GPs' current starburst episodes comes from the detection of the He I λ3819 line. González Delgado et al. (1999) show that this weak line is easily covered up by stellar absorption and is only present for the first 3 Myr following an instantaneous burst of star formation. The He I λ3819 line is evident in the individual spectra of 5 of the 78 GPs, including J1012+13 and J1457+22, which are among the extreme GPs (Figure 3.2). J1219+15 may also exhibit He I λ3819 emission, but the emission is only present at a 2.6σ level. The λ3819 line shows up clearly in each of the stacked spectra as well (Figure 3.2).

The H Balmer lines in the stacked spectra also point to a young age. As with the He I λ3819 line, stellar absorption quickly dominates the higher order Balmer lines (González Delgado et al., 1999). The stacked spectra show the entire Balmer series in emission, which again indicates an upper limit of 3 Myr on the age of an instantaneous burst (González Delgado et al., 1999).

If the star formation is continuous, however, the GPs' starbursts may be older than 3 Myr. For the case of continuous star formation Starburst99 models, the Balmer line EWs give upper age limits of 7-60 Myr (Table 3.5). Similarly, the Balmer emission lines in the stacked spectra give an upper age limit of 20 Myr. The observed He I λ3819 EWs indicate young ages, however, even with continuous star formation. Although He I λ3819 can exist in emission for the first 10 Myr of continuous star formation, the observed He I λ3819 EWs imply ages of 3-6 Myr (González Delgado et al., 1999).

Table 3.4 also lists the stellar mass formed in the burst. To estimate the size of the burst, we compare the observed Hα luminosities with the ionizing photon production rate, Q(H), in the Starburst99 instantaneous burst model. We convert

Table 3.4: Ages of the Extreme GPs (Instantaneous Burst)

Galaxy	Hα		Hβ		HeI λ3819					
	EW[a] (Å)	Age[b] (Myr)	EW[a] (Å)	Age[b] (Myr)	EW[a] (Å)	Age[c] (Myr)	M_{Burst}(3 Myr)[d] (10^6 $M_\odot$)	M_{Burst}(Hβ EW)[e] (10^6 $M_\odot$)	N_{OStars}(3 Myr)[d]	N_{OStars}(Hβ EW)[e]
J0816+22	845	$\leq$ 4.9	196	$\leq$ 4.4	...	...	13.5	39.9	4.54×10^4	1.13×10^5
J1219+15	1304	$\leq$ 4.5	206	$\leq$ 4.4	...	...	57.9	170.7	1.95×10^5	4.86×10^5
J1012+13	1550	$\leq$ 4.2	293	$\leq$ 3.7	1.91	$<$ 2	26.5	42.0	8.91×10^4	1.30×10^5
J1457+22	1008	$\leq$ 4.8	199	$\leq$ 4.4	1.99	$<$ 2	36.4	107.4	1.22×10^5	3.06×10^5
J1009+29	889	$\leq$ 4.9	151	$\leq$ 4.7	...	...	16.6	64.4	5.57×10^4	1.61×10^5
J0303-08	697	$\leq$ 5.1	121	$\leq$ 4.9	...	...	27.7	135.6	9.31×10^4	3.43×10^5

[a] Redshift-corrected.
[b] Age using the instantaneous burst Starburst99 model.
[c] Age using the instantaneous burst model of González Delgado et al. (1999).
[d] From the Hα luminosity, assuming an age of 3 Myr.
[e] From the Hα luminosity, using the Hβ EW-derived age from Column 4.

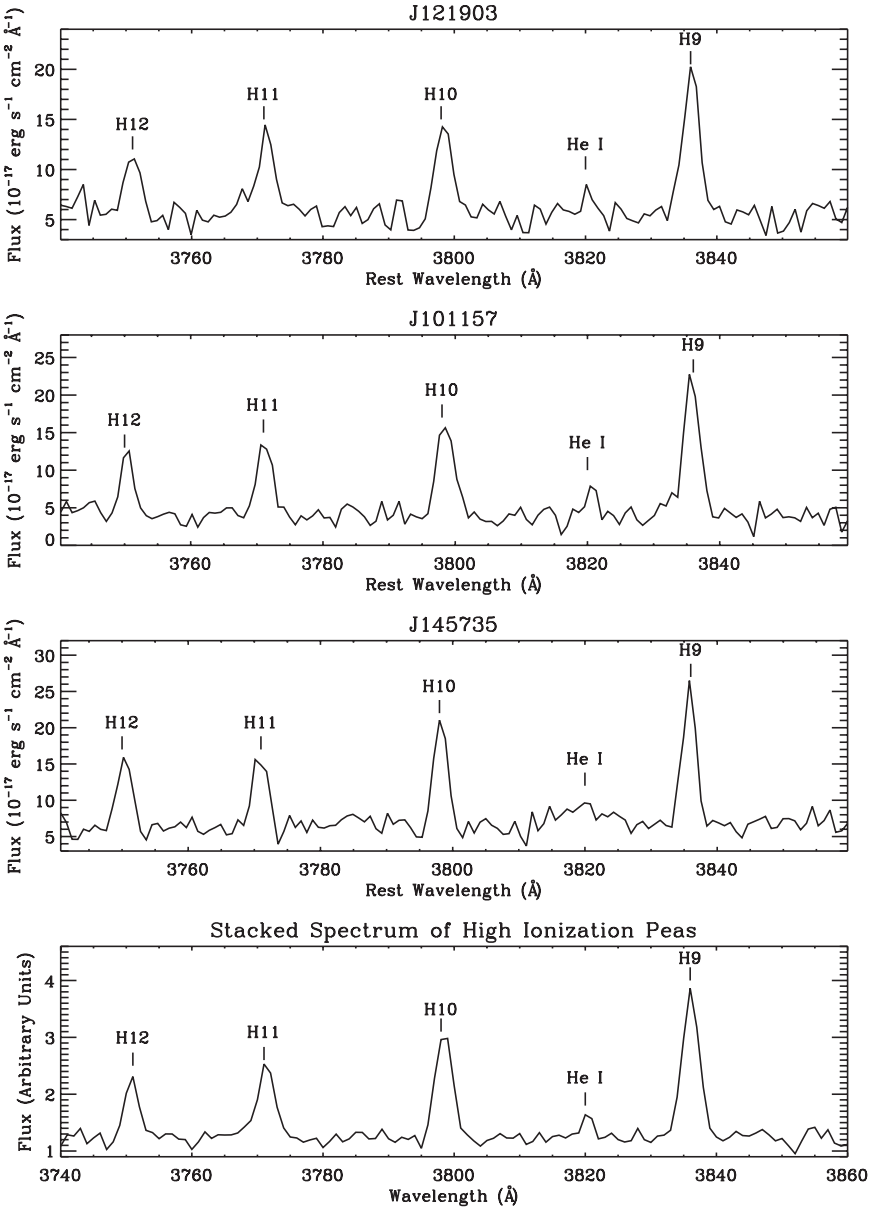

Figure 3.2: The top three panels show the 3740-3860 Å region for GPs J1219+15, J1012+13, and J1457+22. J1012+13 and J1457+22 have detections of the weak He I λ3819 line in emission, and He I λ3819 may be present in J1219+15 as well. The bottom panel shows the same region for the stacked spectrum of the 15 GPs with the highest [O III]/[O II] ratios.

Table 3.5: Ages of the Extreme GPs (Continuous Star Formation)

Galaxy	Hα		Hβ		He I λ3819	
	EW[a] (Å)	Age[b] (Myr)	EW[a] (Å)	Age[b] (Myr)	EW[a] (Å)	Age[c] (Myr)
J0816+22	845	≤ 37.4	196	≤ 16.0	...	...
J1219+15	1304	≤ 13.5	206	≤ 13.9	...	...
J1012+13	1550	≤ 9.7	293	≤ 7.5	1.91	< 3
J1457+22	1008	≤ 25.5	199	≤ 15.3	1.99	< 3
J1009+29	889	≤ 33.4	151	≤ 31.9	...	...
J0303-08	697	≤ 59.3	121	≤ 58.6	...	...

[a]Redshift-corrected.
[b]Age assuming the continuous star formation Starburst99 model.
[c]Age from the González Delgado et al. (1999) continuous star formation model.

Q(H) to an Hα luminosity using the Balmer line ratios, Case B emissivities, and Case B recombination coefficients at 15,000 K from Storey & Hummer (1995). We calculate the starburst mass twice: once assuming an age of 3 Myr, as suggested by the He I λ3819 emission, and once with the instantaneous burst age from the Hβ EW. Since the Hα luminosity is roughly constant for the first 3 Myr, the burst mass corresponding to an age of 3 Myr should also be valid for younger ages. As shown in Table 3.4, the derived burst masses range from 14-171 million $M_\odot$. Using the GPs' total stellar masses from the optical spectral fits of Izotov et al. (2011) and the 3 Myr ages, the bursts account for 2-26% of the total stellar mass of the GPs. If the older ages of 4-5 Myr are adopted, the fraction of the total mass increases. While the burst fractions for four of the extreme GPs remain in the 2-26% range, GPs J1219+15 and J1009+29 have burst fractions of 76% and 87% if the older ages are used. Such high fractions are unlikely, however, especially since the GPs' metallicities of $\sim$0.2 $Z_\odot$ imply enrichment from preceding stellar generations. Furthermore, given the detection of He I λ3819 emission in J1219+15, the younger age and lower burst fraction are preferable.

We next compute the number of O stars in the GPs by comparing the observed Hα luminosities to the ionizing photon rates in the Starburst99 models. We determine how many 10^6 $M_\odot$ bursts would generate the observed Hα luminosities and scale the number of O stars in the Starburst99 models accordingly. We note that this approach

accounts for the WR contribution to the Hα emission. As before, we use both the Hβ EW-derived ages and an age of 3 Myr and record the estimated O star population in Table 3.4.

In either case, continuous or instantaneous star formation, the GPs are evidently young and powerful starbursts. We now turn to the question of the different ionizing sources that may be present in these objects and whether they can explain the observed emission. The GPs themselves may span a range of ages, and different sources may dominate the ionization in individual galaxies.

3.3 High Ionization Lines and Possible Origins

The GPs have [O III] $\lambda\lambda$5007,4959/[O II] λ3727 ratios ranging from 1.5 to as high as 13.7 (Figure 3.1), which may indicate an extremely high ionization parameter and/or a low optical depth. Several of the GPs show other high ionization lines in their spectra, with strong [Ne III] λ3869 emission as well as detectable [Ar IV] λ4712, [Ar IV] λ4740, and He II λ4686. In particular, we detect He II emission in 5 of the 6 most extreme (i.e., highest [O III]/[O II] ratio) GPs. The presence of these weak, high ionization lines suggests the existence of a hard ionizing radiation field, such as that produced by WR stars. Interestingly, while the high-ionization lines show up clearly in the stacked spectra of the GPs (Figure 3.3), no stellar WR features are visible. In particular, the blue bump at 4640-4650 Å, red bump at 5808 Å, and broad He II λ4686 component are absent. Instead, the He II emission line appears narrow, suggesting a nebular origin. In the GPs' individual spectra, the S/N is lower, but WR features are tentatively present in three of the extreme GPs (Figure 3.4). Given the low S/N of these features, they may be spurious detections or narrow, nebular lines, rather than genuine WR features. Their absence from the stacked spectra suggests they may not be real; however, if only a minority of objects have WR features, the features may not appear in the stacked spectra.

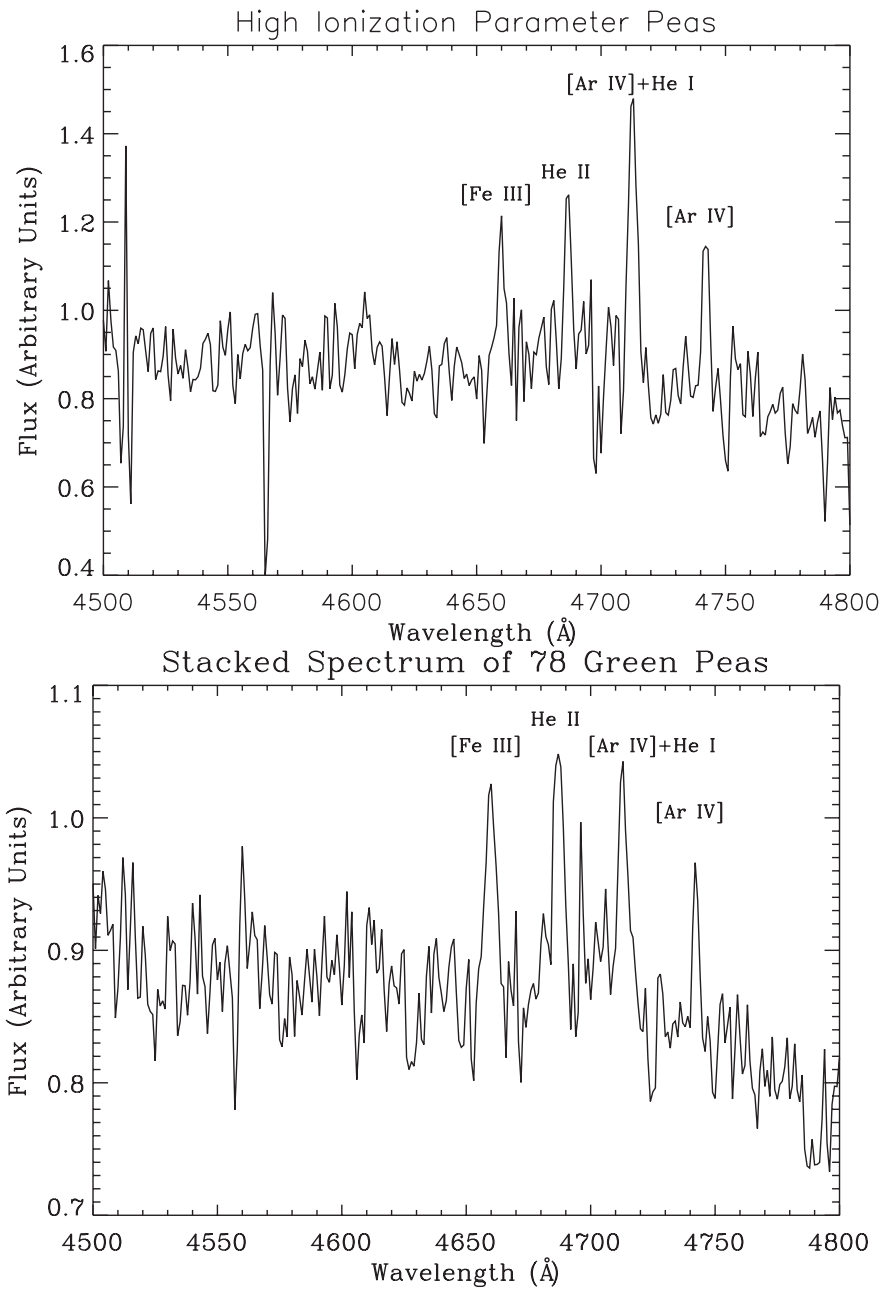

Figure 3.3: The upper panel shows the 4500-4800 Å region of the stacked spectrum for the 15 GPs with the highest [O III]/[O II] ratios. The lower panel displays the same region for a stacked spectrum of all 78 star-forming GPs. The nebular [Fe III] λ4658, He II λ4686, [Ar IV]+He I λ4713, and [Ar IV] λ4740 lines are labelled. No broad WR features are visible.

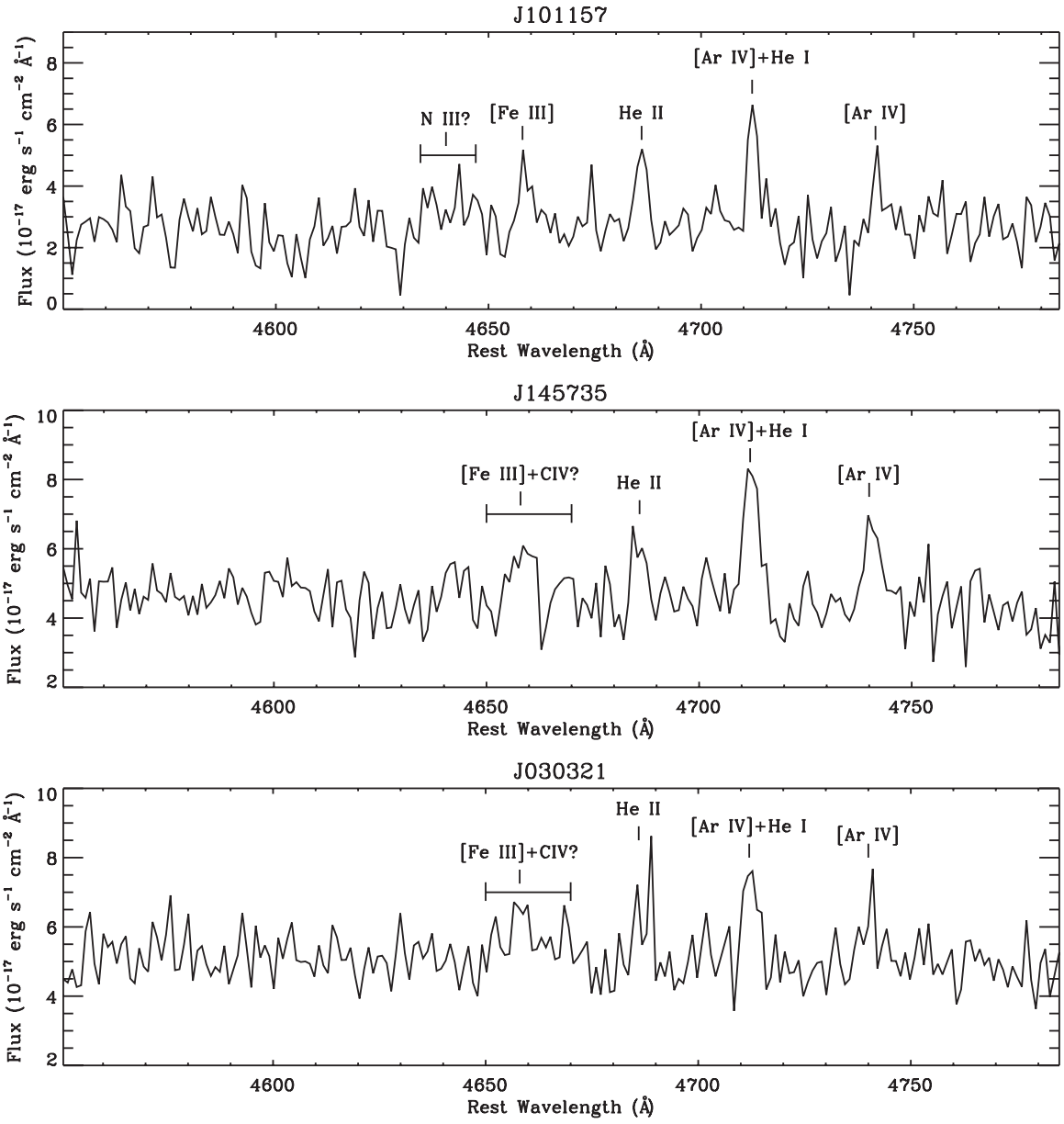

Figure 3.4: The WR blue bump and He II emission for the three GPs which may have WR features.

Some or all of the GPs may therefore fall into a mysterious class of galaxies with He II emission but no WR features (Guseva et al., 2000; Thuan & Izotov, 2005; Shirazi & Brinchmann, 2012). Shirazi & Brinchmann (2012) have recently analyzed 2865 He II-emitting galaxies in SDSS. They find that the fraction of He II-emitters without WR features systematically increases with decreasing metallicity (Shirazi & Brinchmann, 2012). Possible origins for the He II emission include WR stars with weak stellar lines, chemically homogeneous massive stars, AGN, high-mass X-ray binaries (HMXBs), and fast, radiative shocks (Shirazi & Brinchmann, 2012). The precise cause of the He II emission may vary from galaxy to galaxy, however. Here, we specifically evaluate these proposed ionizing sources for the six extreme GPs. We note that if the GPs are indeed optically thin, their low optical depths would further enhance their He II/Hβ ratios by decreasing the observed Hβ emission. We therefore use both density-bounded and radiation-bounded models to evaluate the possible explanations for the He II emission and line ratios observed in the most extreme GPs.

In Table 3.6, we list the He II luminosities and the WR blue bump luminosities or 1σ limits for the 6 extreme GPs. We calculate the 1σ blue bump and He II detection limits using Equation 3.2, correcting for reddening, and assuming rest-frame line widths of 75 Å and 7.07 Å, respectively. The He II width of 7.07 Å is the average rest-frame width of the detected λ4686 lines. The adopted blue bump width corresponds to the maximum extent of the blue bump seen in the composite WN spectra of Crowther & Hadfield (2006). As the actual extent of the blue bump may be less than this value (see e.g., Fernandes et al., 2004), these limits are likely overestimates. In addition, we calculate the detection limits for the WR Si III λ4565 line by assuming it has the same width as the He II line. Any proposed explanation for the high ionization emission must be consistent with the ages and starburst masses of the galaxies and these constraints on the WR and He II emission.

Table 3.6: He II and WR Emission in the Extreme GPs

Galaxy	$L(\mathrm{H}\alpha)^a$	$L(\mathrm{He\,II})^a$	He II λ4686/Hβ	Blue Bump L(N III λ4640)	$L(\mathrm{Si\,III}\ \lambda4565)^{a,b}$	$L(\mathrm{C\,IV}\ \lambda4658)^{a,c}$
J0816+22	910	5.87	0.018	$\leq 4.77^a$	≤ 1.45	...
J1219+15	3910	28.7	0.020	$\leq 11.2^a$	≤ 3.41	...
J1012+13	1790	7.13	0.011	9.79 ± 2.82	≤ 1.98	...
J1457+22	2460	6.64	0.008	$\leq 7.03^a$	≤ 2.14	9.32 ± 2.37
J1009+29	1120	$\leq 4.12^a$	$\leq 0.010^a$	$\leq 13.4^a$	≤ 4.08	...
J0303-08	1870	8.24	0.012	$\leq 5.79^a$	≤ 1.76	20.8 ± 3.7

[a] In $10^3 9$ ergs s^{-1} .
[b] 1σ limit.
[c] May include nebular [Fe III] emission.

3.3.1 Stellar WR Feature

Although the narrow width of the observed He II λ4686 line seems to indicate a nebular origin, a narrow stellar line could contribute some portion of the emission. In particular, while most WR stars have broad He II emission lines, the WN9 subtype has a He II λ4686 full width at half maximum (FWHM) of only 6 ± 2Å (Chandar et al., 2003). Our observed He II FWHMs range from $\sim 3-5$ Å, slightly lower than the WN9 FWHMs. For comparison, the SDSS spectral resolution at these wavelengths is $\sim 2-3$ Å, which suggests these lines are unresolved and not stellar in origin. Given the low S/N of the He II line and the uncertainty in the WN9 FWHM, however, we cannot rule out the WN9 stellar line hypothesis. Furthermore, observations suggest that late-type WR stars may have weaker or narrower lines at lower metallicities (Conti et al., 1989; Crowther & Hadfield, 2006).

Assuming the He II is purely stellar in origin, we derive the number of WN9 stars necessary to produce the observed He II line luminosities. We adopt the λ4686 luminosities for late-type WN (WNL) stars given in Brinchmann et al. (2008): $L(\lambda4686) = 4.3 \times 10^{35}\,\mathrm{ergs\,s^{-1}}$ for $Z < 0.2\,\mathrm{Z}_\odot$ and $L(\lambda4686) = 2.47 \times 10^{36}\,\mathrm{ergs\,s^{-1}}$ for $Z \geq 0.2\,\mathrm{Z}_\odot$. Since the GPs have average metallicities of $\sim 0.2\,\mathrm{Z}_\odot$, we calculate the number of WNL stars using both luminosities and list the derived numbers in Table 3.7. Brinchmann et al. derived the λ4686 luminosities from WN5-WN6 stars, which are more well studied than WN9 stars. However, WN5-6 stars generally have stronger He II emission

Table 3.7: Constraints on WN9 Stars in the GPs

Galaxy	N(WN9 stars)[a] from He II λ4686		N(WN9 stars)[b] from N III λ4640		N(WN9 stars)[c] from Si III λ4565	WN9/O from He II λ4686	
	$Z < 0.2\,Z_\odot$	$Z \geq 0.2\,Z_\odot$	$Z < 0.2\,Z_\odot$	$Z \geq 0.2\,Z_\odot$		$Z < 0.2\,Z_\odot$	$Z \geq 0.2\,Z_\odot$
J0816+22	13600	2380	$\leq 11900^d$	$\leq 7570^d$	≤ 2200	0.12-0.30	0.02-0.05
J1219+15	66700	11600	$\leq 28000^d$	$\leq 17800^d$	≤ 5170	0.14-0.34	0.02-0.06
J1012+13	16600	2890	24500	15500	≤ 3000	0.13-0.19	0.02-0.03
J1457+22	15400	2690	$\leq 17600^d$	$\leq 11200^d$	≤ 3240	0.05-0.13	0.009-0.02
J0303-08	19200	3340	$\leq 14500^d$	$\leq 9190^d$	≤ 2670	0.06-0.21	0.01-0.04

[a]Number of stars needed to produce the observed He II luminosity.
[b]Limit on the WN9 population from N III λ4640.
[c]1σ limits on the WN9 population from Si III λ4565.
[d]From the 1σ limit.

than WN9 stars (e.g., Crowther & Hadfield, 2006). The mean He II λ4686 luminosity of WN5-WN6 stars in the Large Magellanic Cloud (LMC) is a factor of 2.4 greater than that of WN7-WN9 stars (Crowther & Hadfield, 2006). We therefore note that the required number of WN9 stars may be underestimated.

In addition to the blue bump emission at λ4640 from N III, WN9 stars show Si III λ4565 emission (Guseva et al., 2000). Based on the blue bump and Si III luminosities or 1σ detection limits (Table 3.6), we calculate the number of WN9 stars that could be present and list these values in Table 3.7. We adopt the WNL blue bump luminosities of Brinchmann et al. (2008), which are 4.0×10^{35} ergs s^{-1} for $Z < 0.2\,Z_\odot$ and 6.3×10^{35} ergs s^{-1} for $Z \geq 0.2\,Z_\odot$. Schaerer & Vacca (1998) list WNL star blue bump luminosities of $\sim 2 \times 10^{36}$ ergs s^{-1}. Adopting these higher values would result in significantly lower estimates of the number of WNL stars present. For the Si III λ4565 luminosity, we adopt $L(\lambda4565) = 6.6 \times 10^{35}$ ergs s^{-1} from Guseva et al. (2000). We note that each of these line luminosities may be uncertain by a factor of two (Crowther & Hadfield, 2006). Even within a given WN subtype, He II and blue bump luminosities span a wide range of values (Crowther & Hadfield, 2006), and Guseva et al. (2000) admit that the Si III λ4565 luminosities are poorly known.

Assuming the $Z < 0.2\,Z_\odot$ values, the extreme GPs would need to contain 13,000-68,000 WN9 stars to account for the observed λ4686 luminosities (Table 3.7). From the estimated numbers of O stars in Table 3.4, the required low-metallicity WN9

population indicates WR/O ratios of 0.05-0.34 (Table 3.7). In all but one case, these high WR/O ratios are impossible to match with either the instantaneous burst or continuous star formation Starburst99 models. Furthermore, while the blue bump limits are consistent with this number of WN9 stars at the 3σ level, the Si III limits do not allow such a large population of WN9 stars.

A population of WN9 stars with the $Z \geq 0.2\,Z_{\odot}$ luminosities is also unlikely. The GPs would need 2,000-12,000 WN9 stars, resulting in WR/O ratios of 0.01-0.06. The Starburst99 models show that these WR/O ratios occur in an instantaneous burst between 3 and 5 Myr in age, and the 1σ blue bump and Si III λ4565 detection limits are compatible with this number of WN9 stars. Nevertheless, these WR/O ratios assume that all WR stars in the GPs are in the WN9 phase, which is implausible.

The feasibility of the WN9 scenario depends strongly on the assumed emission line luminosities. To account for the observed He II emission, the WN9 stars in the GPs must have the high He II luminosities characteristic of stars with $Z \geq 0.2\,Z_{\odot}$. While the exact metallicity dependence of WNL line luminosities is not yet understood, the lower line luminosities associated with metal-poor stars are probably more appropriate for the GPs. Even these latter luminosities may be higher than is realistic, however. As discussed above, the adopted WN9 He II line luminosities may be overestimated by a factor of 2-3. Finally, none of the higher S/N stacked spectra show any evidence of WR features (Figure 3.3), although the blue bump emission in the low-metallicity case should be almost as strong as He II λ4686. Given the significant uncertainties in the WN9 luminosities and line widths (e.g., Crowther & Hadfield, 2006), we cannot definitively rule out the WN9 scenario. However, we conclude that stellar emission from WN9 stars is unlikely to be the dominant source of the observed He II emission.

3.3.2 Ionization by Hot Stars

3.3.2.1 WR Stars

The other possibility is that the He II is nebular in origin rather than stellar. The clear presence of other high-ionization nebular lines, such as [Ar IV] $\lambda\lambda$4712,4740 and strong [Ne III] λ3869, supports this scenario. If the nebular He II emission is due to photoionization from stars, the stars responsible must have sufficient emission shortward of 228 Å. Extremely hot WR stars (e.g., Smith et al., 2002) or metal-poor O stars (Kudritzki, 2002) may have spectral energy distributions hard enough to doubly ionize He.

To test this hypothesis, we create a grid of photoionization models with CLOUDY version 10.00 (Ferland et al., 1998) for nebulae around stars of different spectral types. We use the Smith et al. (2002) model grids at $Z = 0.2\,Z_{\odot}$ for main sequence O stars of spectral types O3-O6 and for WN and WC stars with core temperatures of 45,000 K-120,000 K; the WR core temperatures correspond to a stellar optical depth of 10. The grids use WM-Basic stellar atmosphere models (Pauldrach et al., 2001) for the O stars and CMFGEN models (Hillier & Miller, 1998) for the WR stars.

Since the ionization parameter is set by a combination of nebular geometry, density, and input radiation field (Equation 3.1), we vary these parameters in our models. Our input stellar spectral energy distributions are scaled to a constant hydrogen-ionizing photon rate of $Q(\mathrm{H}) = 10^{49.5}$ photons s^{-1}, which is the Q(H) value of an O3 V star at $0.2\,Z_{\odot}$ (Smith et al., 2002). We have run additional models with $Q(\mathrm{H}) = 10^{50}$ photons s^{-1}; this change does not affect our results. For each spectral type, we vary the inner radius (r_{in}) of the nebula from 0.5 pc to 8 pc and the hydrogen density from 0.01 to 1000 cm^{-3}. These inner radii correspond to a wide range of morphologies; r_{in} ranges from 0.2% to 99.9% of the outer radius of the ionized gas (r_{out}). Morphologies with $r_{\mathrm{in}}/r_{\mathrm{out}} < 5\%$ only appear in models with $n_{\mathrm{H}} \leq 10$ cm^{-3}. Extremely thin shell

morphologies, with $r_{\rm in}/r_{\rm out} > 95\%$, appear in some of the high density models and are marked with open circles in the figures.

The gas phase metallicities match the stellar metallicities in each model run. We use element abundances from McGaugh (1991), interpolating between $Z = 0.15\,{\rm Z}_{\odot}$ and $Z = 0.30\,{\rm Z}_{\odot}$ to the GPs' metallicities of 0.2 ${\rm Z}_{\odot}$. For the abundances of all other elements, we use the CLOUDY gas-phase ISM abundances (Cowie & Songaila, 1986; Savage & Sembach, 1996) and scale the abundances of the α-elements to the O abundance from McGaugh (1991). We set the turbulence to 4 ${\rm km\,s^{-1}}$ and the grain abundances to 20% of the CLOUDY ISM value (Mathis et al., 1977). Changing the turbulence to 40 ${\rm km\,s^{-1}}$ does not affect our results.

We analyze the resulting line emission from both radiation-bounded and density-bounded scenarios by examining the cumulative line fluxes at different radii within the nebulae. The fluxes at low radii correspond to optically thin scenarios, since the gas has not fully absorbed all the ionizing photons at that radius. To evaluate the models, we compare the predicted and observed line ratios for [O II] λ3727/Hβ, [Ne III] λ3869/Hβ, He II λ4686/Hβ, [Ar IV] λ4740/[Ar III] λ7135, [O III] $\lambda\lambda$5007,4959/[O II] λ3727, and He I λ5876/Hβ. We focus on [Ar IV] λ4740 rather than the stronger [Ar IV] λ4711 line due to contamination from He I λ4713. While [O III]/[O II] and [Ar IV]/[Ar III] are particularly sensitive to the ionization parameter or optical depth, He II/Hβ sets strong constraints on the temperature of the ionizing source. As shown in Figure 3.5, even though both WR and O star models can match the other line ratios, only the hottest, early-type WR stars, with core temperatures greater than 70,000 K, can produce the observed He II/Hβ ratios. Higher density models are also more successful at reproducing the observed [O III]/[O II] ratios.

Using the He^{+}-ionizing photon rates from Smith et al. (2002) for the hottest WN and WC stars, we calculate the number of extreme early-type WR stars necessary to account for the observed He II luminosities. We use the helium emissivities and

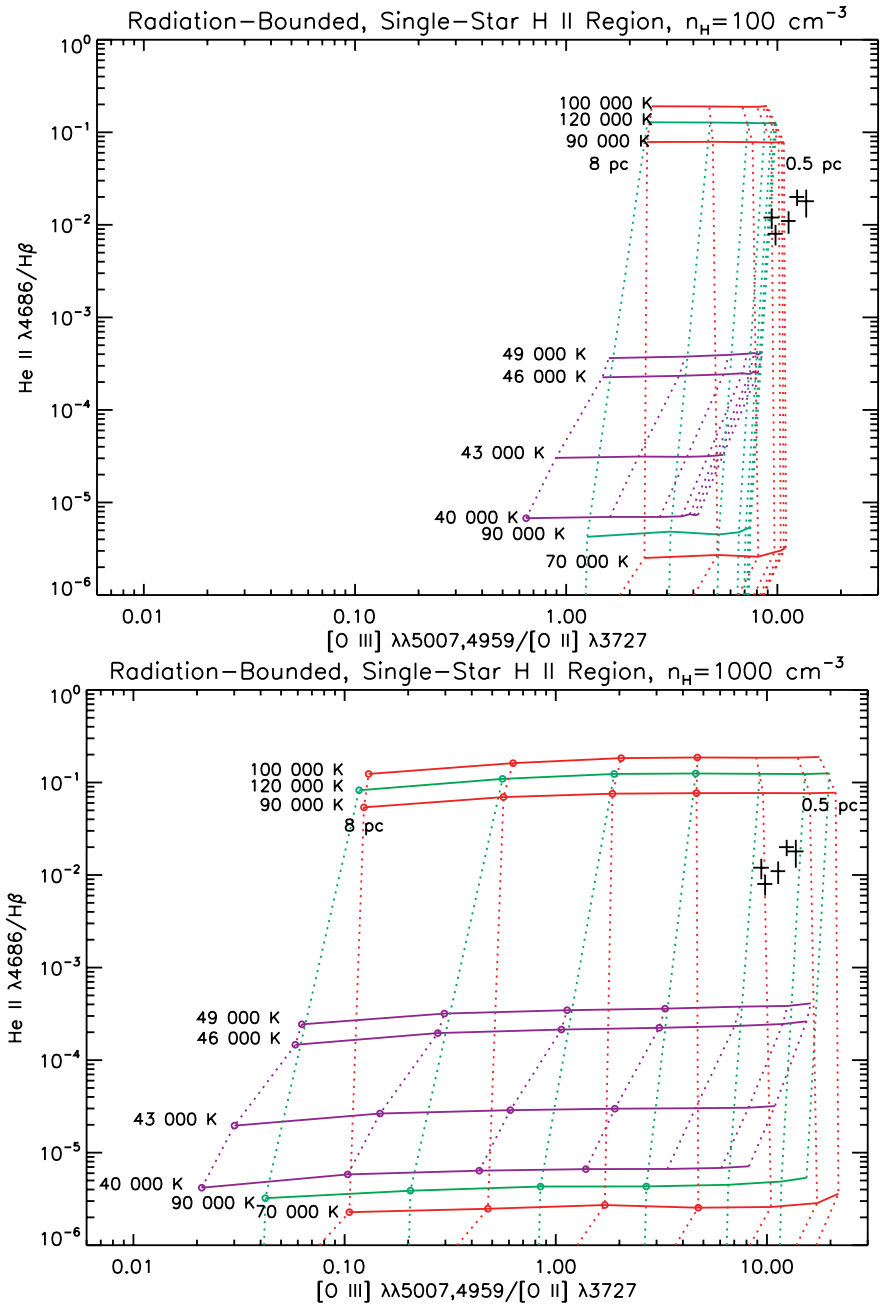

Figure 3.5: Radiation-bounded (optically thick) CLOUDY photoionization model grids for single-star H II regions at densities of $n_{\rm H} = 100$ cm^{-3} (top) and $n_{\rm H} = 1000$ cm^{-3} (bottom). The black crosses show the positions of the five high-ionization GPs with He II detections and the 1σ errors. The red grid corresponds to the WN star photoionization models, green corresponds to WC stars, and purple corresponds to main sequence O stars. Solid lines indicate constant stellar temperature; the O star effective temperatures and WR star core temperatures are labelled. Dotted lines indicate constant values of the inner nebular radius, from 0.5 pc to 8 pc. Thin shell models, where $r_{\rm in}/r_{\rm out} > 95\%$, are marked with open circles. Only the hottest WR stars match the observed line ratios.

Table 3.8: Constraints on WNE Stars in the Green Peas

Galaxy	N(WNE stars)[a] from He II λ4686	N(WNE stars)[b] from N V $\lambda\lambda$4603-20		WNE/O from He II λ4686
		$Z < 0.2\,Z_\odot$	$Z \geq 0.2\,Z_\odot$	
J0816+22	2100	$\leq$ 200000	$\leq$ 30000	0.02-0.05
J1219+15	10000	$\leq$ 470000	$\leq$ 70000	0.02-0.05
J1012+13	2600	$\leq$ 270000	$\leq$ 41000	0.02-0.03
J1457+22	2400	$\leq$ 290000	$\leq$ 44000	0.008-0.02
J0303-08	3000	$\leq$ 240000	$\leq$ 36000	0.009-0.03

[a]Number of stars needed to produce the observed He II luminosity.
[b]1σ limit on the WNE population from N V $\lambda\lambda$4603-4620, using the WNE star N V luminosities of Brinchmann et al. (2008).

Table 3.9: Constraints on WCE Stars in the Green Peas

Galaxy	N(WCE stars)[a] from He II λ4686	N(WCE stars)[b] from C III+C IV $\lambda\lambda$4650-4658	WCE/O from He II λ4686
J0816+22	1100	...	0.009-0.02
J1219+15	5200	...	0.01-0.03
J1012+13	1300	1200	0.01
J1457+22	1200	1900	0.004-0.01
J0303-08	1500	1400	0.004-0.02

[a]Number of stars needed to produce the observed He II luminosity.
[b]Inferred WCE population from C III+C IV $\lambda\lambda$4650-4658, using the WCE star C III and C IV luminosities of Crowther & Hadfield (2006). The C III+C IV emission may be contaminated by nebular [Fe III].

recombination coefficients from Storey & Hummer (1995) for $n_e = 100$ cm^{-3} and $T_e = 15,000$ K. Tables 3.8 and 3.9 list the numbers of early-type WN (WNE) and WC (WCE) stars. The resulting WR/O ratios, calculated as in §3.3.1, are a few percent, which matches the expected value for a 3-4 Myr old instantaneous burst. However, if the star formation is continuous, the Starburst99 models show that the WR/O ratios should never increase above 0.016 due to the continued production of new O stars.

While the WR/O ratios are reasonable, at least for an instantaneous burst, we also consider whether the constraints on WR stellar features are consistent with this number of WR stars. The blue bump emission of WNE stars comes from N V λ4603-4620, and the WNE stars have weaker blue bump luminosities than the WNL stars (Brinchmann et al., 2008). Thus, the required population of 2000-9000 WNE stars could easily go unnoticed in the GPs' spectra (see Table 3.8). WNE stars do have strong and broad He II λ4686 emission, however. Adopting the $Z < 0.2\,Z_\odot$and $Z \geq 0.2\,Z_\odot$ WNE λ4686 luminosities of Brinchmann et al. (2008), we find that the broad

component should be 6%-30% the strength of the nebular component, respectively. Although we do not see any broad He II component in the stacked spectra, we cannot rule out the presence of WNE stars, particularly if the lower metallicity luminosities are valid.

The WCE stars should also have broad He II emission, blended with C III λ4650 and C IV λ4658 (e.g., Crowther & Hadfield, 2006). From the WCE λ4686 and λ4650 luminosities of Crowther & Hadfield (2006), the broad He II component should be 89% as strong as the nebular emission. The lack of this broad emission in the stacked spectra (Figure 3.3) indicates that thousands of WCE stars are unlikely to be present in most GPs. One GP that might plausibly have WCE stars is J0303-08, which appears to have broad $\lambda\lambda$4650-4670 emission (Figure 3.4). The strength of this emission is consistent with the number of WCE stars required to produce the observed He II. As with the WNE stars, Starburst99 models can match the inferred WC/O ratios with an instantaneous burst but not with continuous star formation.

The above calculations show that photoionization by early-type WR stars is possible. In reality, the nebular gas in the GPs is likely photoionized by stars of many different spectral types. Consequently, we ran CLOUDY photoionization models with the $10^6\,M_\odot$ Starburst99 instantaneous burst model (§3.2.1) as the input ionizing spectrum. The nebular model parameters are the same as described for the single-star models, except for the inner radius, which we varied from 20-81 pc, and the hydrogen-ionizing photon rate, $Q(\mathrm{H})$, which varies as a function of the age of the starburst. As before, these models occasionally produce thin shell nebulae, where $r_{\rm in}/r_{\rm out} > 95\%$. We denote radiation-bounded, thin shell models by open circles in the figures. The other optically thick models have $r_{\rm in}/r_{\rm out}$ between 8.6% and 95%. The thin shell models may be valid if dense filaments dominate the GPs' nebular emission.

We plot the CLOUDY and Starburst99 results for several emission line ratios in Figures 3.6-3.9. Ages of $\sim$ 4-5 Myr, when the burst contains a high fraction of

WR stars, do the best job of fitting the observed He II/Hβ ratios. At all ages, the models have difficulty matching the observed [O II]/Hβ ratios. Part of this discrepancy arises from the modeled nebular morphology. The models treat the ionized gas as a shell surrounding an inner cavity. While this is an appropriate model for a single superbubble, the ionized gas in the GPs is likely much less homogeneous. By adding a filling factor and treating the ionized gas as dense clumps in a lower density medium, we obtain an improved fit to the [O II]/Hβ emission (Figures 3.8 and 3.9; see also Zastrow et al. 2013). We adopt filling factors of 1, 0.1, and 0.01, where the filling factor indicates the volume of the gas occupied by clumps of a given density. The remaining volume is treated as a vacuum. The filling factor models are still offset to lower [O III]/[O II] ratios than we observe, which may indicate a need for higher temperature sources. As we discuss in the next section, unusually hot massive stars could explain this discrepancy.

The CLOUDY models support both optically thick and optically thin scenarios, depending on the nebular parameters. In general, the models with higher densities and larger inner radii imply lower optical depths. For densities $n < 1000$ cm^{-3}, the strength of the [O II]/Hβ ratio implies a high optical depth, while the combination of [Ne III]/Hβ and [Ar IV]/[Ar III] ratios suggests a low optical depth. For the $n = 1000$ cm^{-3} models, applicable to J1219+15, the [O II]/Hβ ratio supports a low optical depth if the inner radius is larger than 50 pc or if the filling factor is 0.01. The other line ratios generally favor low optical depths for $n = 1000$ cm^{-3} and an inner radius larger than 30 pc and high optical depths in the other models. We discuss the optical depth further in §4.3.

Photoionization by WR stars is a viable explanation for the GPs' line ratios, as long as the starbursts are old enough to have a sizeable WR population. The clear detection of the He I λ3819 line in GPs J1219+15, J1012+13, and J1457+22 (see §3.2.1) calls this interpretation into question. In addition, the WR hypothesis depends

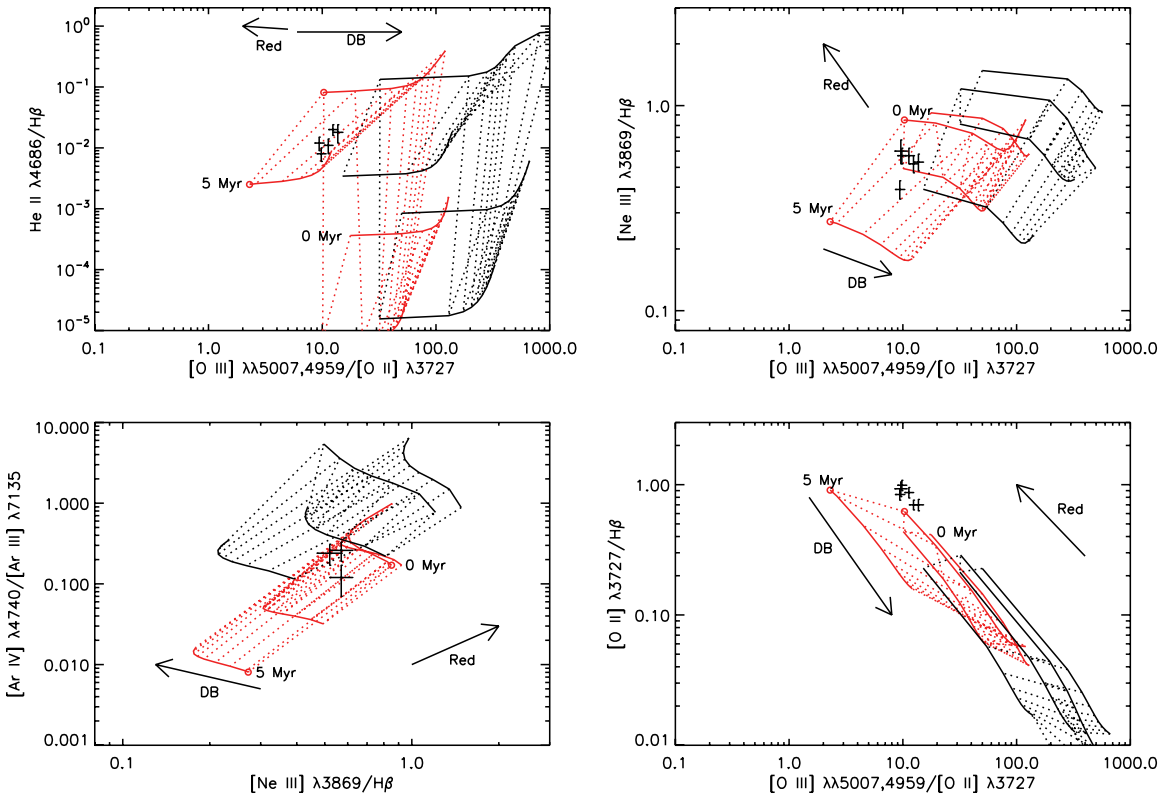

Figure 3.6: CLOUDY grids with a $10^6\,M_\odot$ ionizing cluster and a nebular density of $n_H = 100$ cm^{-3}. The high-ionization GPs are marked with black crosses indicating the 1σ errors for the line ratios. The black grids have an inner radius of 20 pc, while the red grids have an inner radius of 81 pc. Solid lines indicate the age of the cluster and correspond to ages of 0, 3, 4, and 5 Myr. The arrow labeled 'DB' indicates the direction of decreasing optical depth (increasing density-bounding). Constant values of the optical depth are indicated by the dashed lines in each grid. The dashed lines show the emission as the nebular size is decreased from its full ionized extent to 20% of its original thickness, corresponding to a decrease in the optical depth. The arrow labeled 'Red' indicates the reddening vector; the plotted points would move parallel to this vector as the reddening correction is increased. Open circles mark thin shell models with $r_{in}/r_{out} > 95\%$, where r_{out} is the outer radius of nebula for the radiation-bounded case.

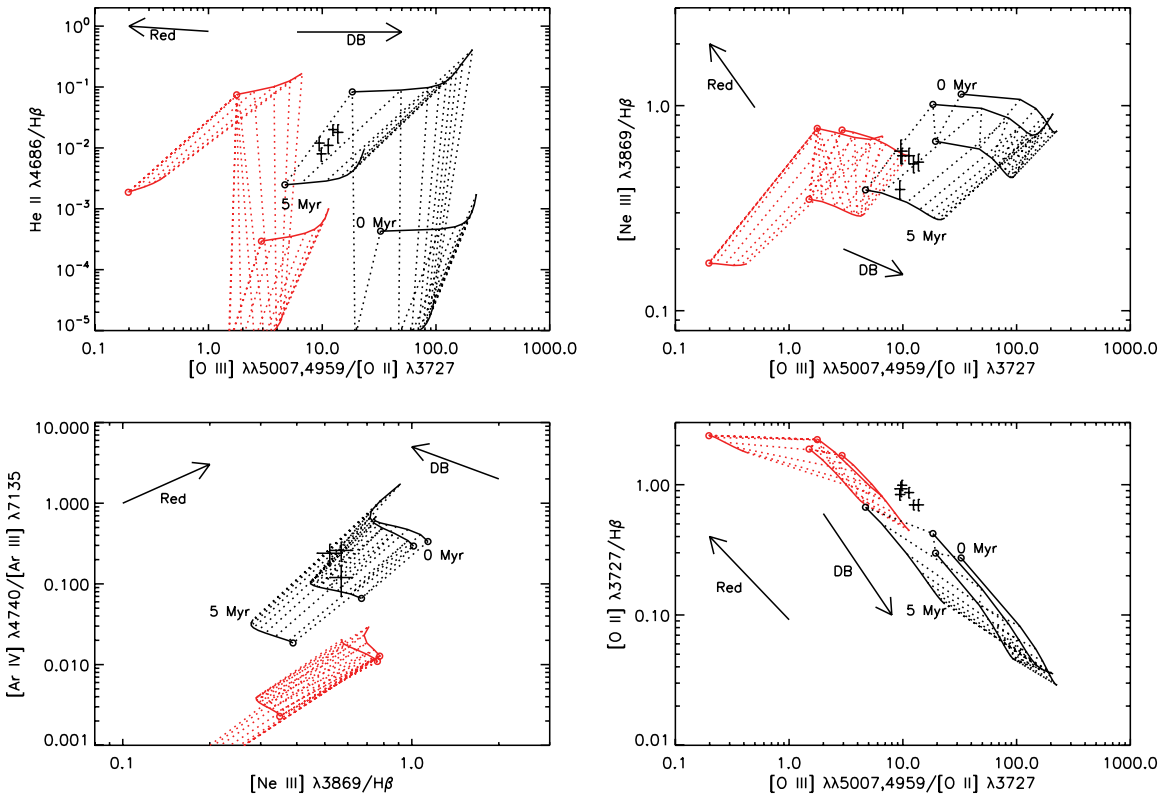

Figure 3.7: CLOUDY and Starburst99 grids for $n_{\rm H} = 1000$ cm^{-3}. Colors and symbols are described in Figure 3.6.

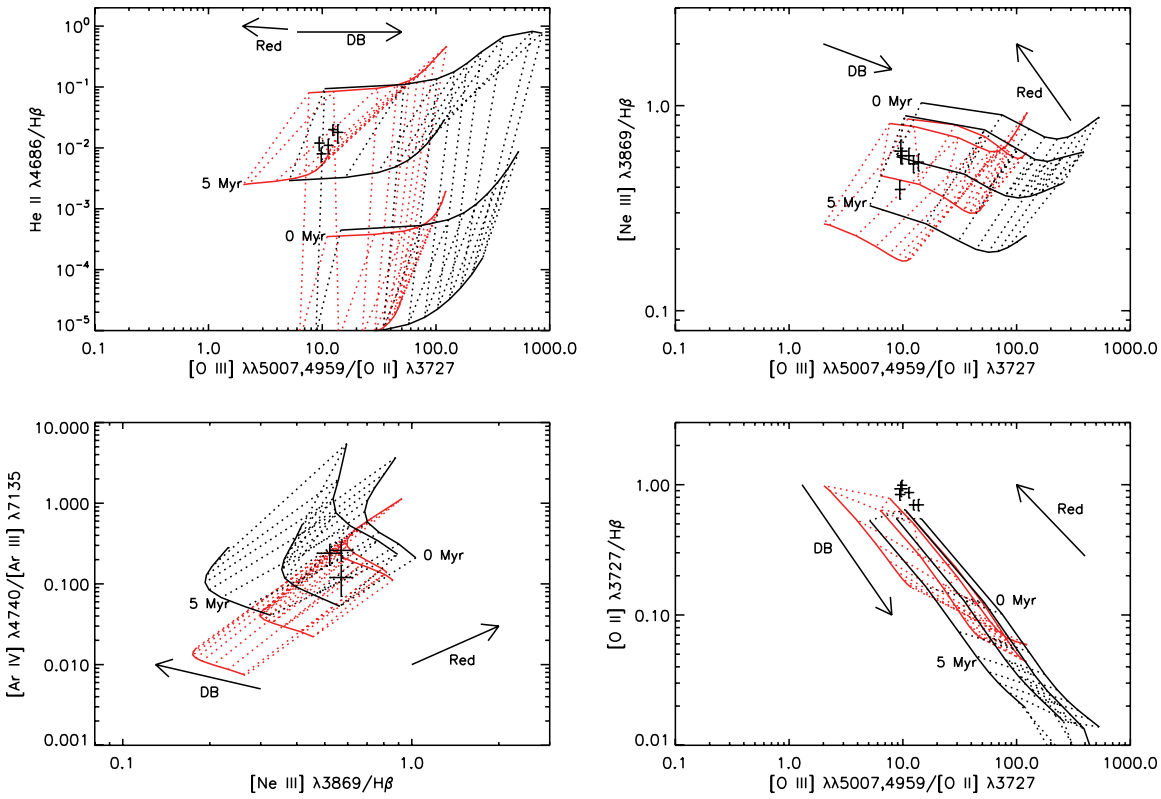

Figure 3.8: CLOUDY and Starburst99 grids for $n_{\rm H} = 100$ cm^{-3} and a filling factor of 0.1. Colors and symbols are described in Figure 3.6.

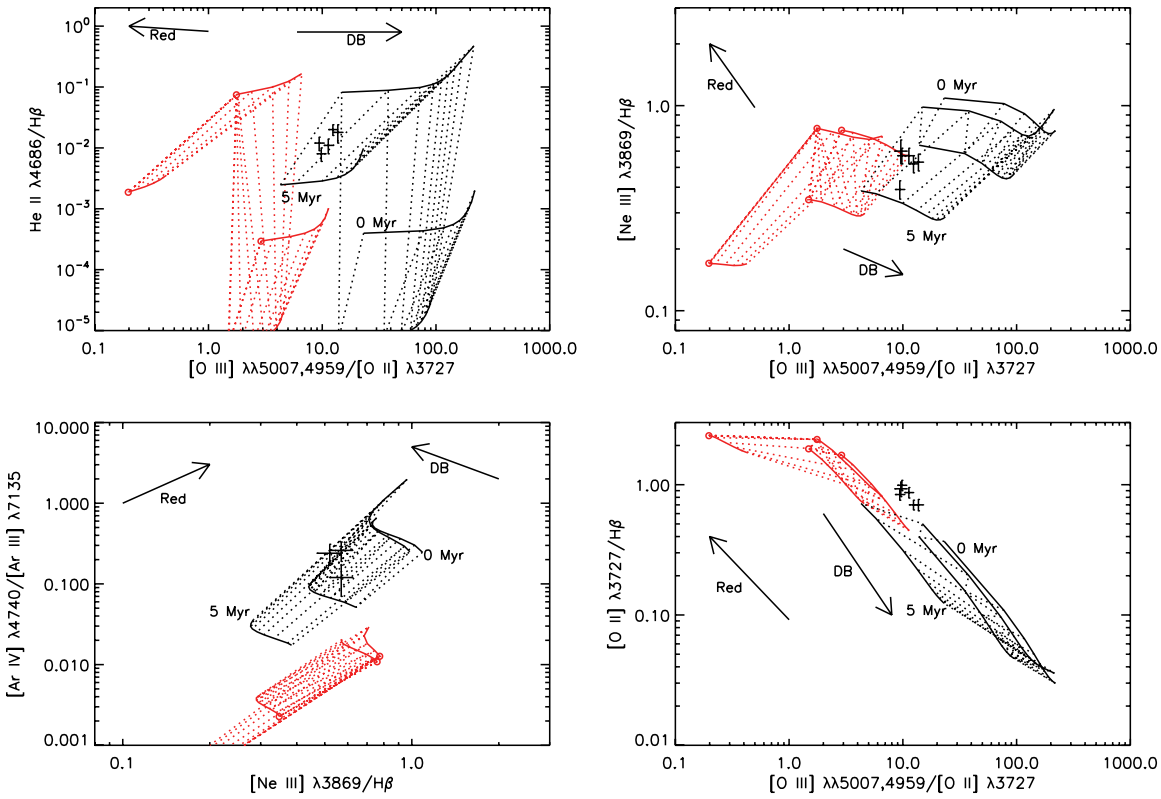

Figure 3.9: CLOUDY and Starburst99 grids for $n_{\rm H} = 1000$ cm^{-3} and a filling factor of 0.1. Colors and symbols are described in Figure 3.6.

strongly on our choice of WR line luminosities. While hot WR stars may account for part of the He II emission in the high-ionization GPs, additional causes of the emission may be required for the youngest GPs.

3.3.2.2 Homogeneously-Evolved O Stars

If WR stars are not present, hot, low-metallicity O stars could perhaps be the source of the hard ionizing photons. In the past few decades, studies have increasingly recognized that massive, rotating stars at low metallicity can achieve much higher effective temperatures than ordinary O stars. At low metallicity, weaker stellar winds make it difficult for stars to lose angular momentum (Langer, 1998), and as a result, stars can maintain high rotational velocities. The associated rotational mixing may then result in chemically homogeneous or quasi-homogeneous evolution (e.g., Maeder, 1987; Yoon et al., 2006). Chemically homogeneous O stars may have effective temperatures much higher than expected for their mass. Brott et al. (2011a) show that, at the metallicity of the LMC, stars more massive than 20 $M_\odot$ may reach temperatures as high as 60,000-70,000 K. The highest mass stars are the most likely to evolve homogeneously and reach such high temperatures (e.g., Brott et al., 2011a). These stars also evolve more quickly than lower mass O stars and could be present in young starbursts. For instance, the models of Brott et al. (2011a) show that 60 $M_\odot$ stars at Small Magellanic Cloud (SMC) metallicity can reach 60,000 K within 3.4 Myr. As discussed in §3.3.2.1, high temperature stars are necessary to reproduce the observed He II/Hβ ratios. These high temperature O stars may be plentiful in low-metallicity starbursts and could provide the necessary high-energy photons for the GPs' He II emission.

As a test, we consider the 60,000 K O star models of Kudritzki (2002). We ran a single-star H II region CLOUDY model as described in §3.3.2.1 for the $T_{\rm eff} = 60,000$ K, $\log(L/\,L_\odot) = 7.03$ luminosity O star model. Figure 3.10 shows that a 60,000 K

Table 3.10: Hot O Stars in the Green Peas

Galaxy	N(60,000 K O stars) from He II λ4686	60,000 K O Stars / Total O Stars
J0816+22	1200	0.01-0.03
J1219+15	5800	0.01-0.03
J1012+13	1500	0.01-0.02
J1457+22	1400	0.004-0.01
J0303-08	1700	0.005-0.02

O star continues the trend of increasing He II/Hβ with effective temperature. The 60,000 K O star model still under-predicts the observed He II/Hβ ratio. However, O stars with temperatures above 60,000 K could result in higher He II/Hβ ratios.

To determine the number of hot O stars needed to generate the observed He II luminosities, we use the ionizing photon rates from Kudritzki (2002) for the $\log(L/\,\mathrm{L}_\odot) = 7.03$, 60,000 K star (see Figure 11 of Kudritzki, 2002) and emissivities and recombination rates for $T_e = 15,000$ K and $n_\mathrm{H} = 100$ cm^{-3} (Storey & Hummer, 1995). Table 3.10 lists the calculated numbers of hot O stars. The number of 60,000 K O stars required to explain the GPs' emission represent 0.4-3% of their total O star populations. For comparison, at ages less than 3 Myr, the instantaneous burst Starburst99 model shows that 8-18% of O stars have spectral types earlier than O4. Therefore, if the earliest spectral types evolve homogeneously, this population could account for the high ionization lines observed in the GPs. Nevertheless, we caution that the existence of chemically homogeneous massive stars has not yet been confirmed, even in local, low-metallicity galaxies (e.g., Brott et al., 2011b). More research is necessary to establish whether homogeneous stars are present in the GPs.

3.3.3 Active Galactic Nuclei

Although the BPT diagram indicates the GPs are star-forming, many of the galaxies lie close to the maximum starburst line of Kewley et al. (2001), which marks a theoretical separation between starbursts and AGN. Given their proximity to this line, the GPs could have some AGN contribution to their emission (Figure 3.11). Shirazi & Brinchmann (2012) show that a plot of He II λ4686/Hβ versus [N II] λ6584/Hα results

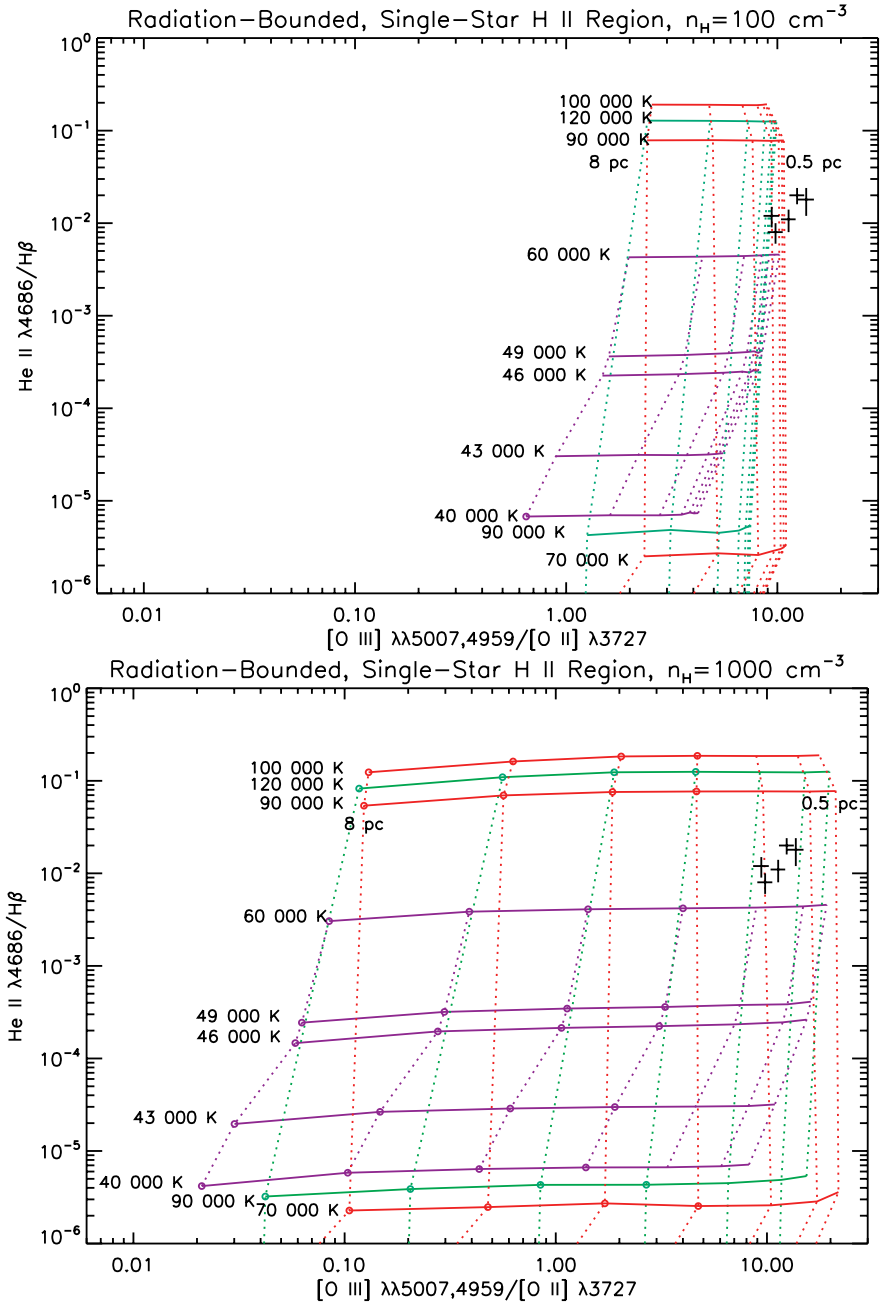

Figure 3.10: As in Figure 3.5, with the inclusion of the 60,000 K O star model of Kudritzki (2002).

in a much cleaner separation between AGN and star-forming galaxies. Figure 3.11 shows the Shirazi & Brinchmann (2012) diagnostic for the GPs with He II λ4686 detections. The line indicates the region where AGN contribute 10% of the observed He II flux. All the observed He II fluxes lie below this line, solidly in the star-forming regime, confirming that AGN activity contributes negligibly to the high ionization emission in the GPs.

3.3.4 High-Mass X-ray Binaries

Following a starburst event, HMXBs could be a significant source of hard photons. In addition, HMXB luminosities may be higher at the low metallicities characteristic of the GPs. Given the increase of X-ray heating with metallicity, black holes may be able to accrete more gas at low metallicity (Thuan et al., 2004). Alternatively, the weaker winds and lower mass loss rates of low metallicity stars may lead to the formation of higher mass black holes (Thuan & Izotov, 2005; Fragos et al., 2013). In three low-metallicity blue compact dwarf (BCD) galaxies, Kaaret et al. (2011) find X-ray luminosities an order of magnitude higher than expected from the SFR. The metallicities of these sources are lower than the GPs, however, with $Z < 0.07\,Z_{\odot}$; HMXB luminosities at $0.2\,Z_{\odot}$ might not show such a dramatic increase.

While an HMXB scenario is appealing, it faces a number of problems when applied to the GPs. The GPs' young ages may be at odds with the HMXB interpretation, as the formation of HMXBs requires both the formation of a compact object and additional time for the evolution of the companion star (Ghosh & White, 2001). The first HMXBs appear 4 Myr after a burst of star formation (Linden et al., 2010), which is inconsistent with the upper age limits for at least one of the GPs. In addition, the simulations of Linden et al. (2010) show that HMXB numbers and luminosities have a complex dependence on metallicity. In fact, at 5 Myr after a burst, high-metallicity galaxies have a greater number of luminous HMXBs than low-metallicity galaxies.

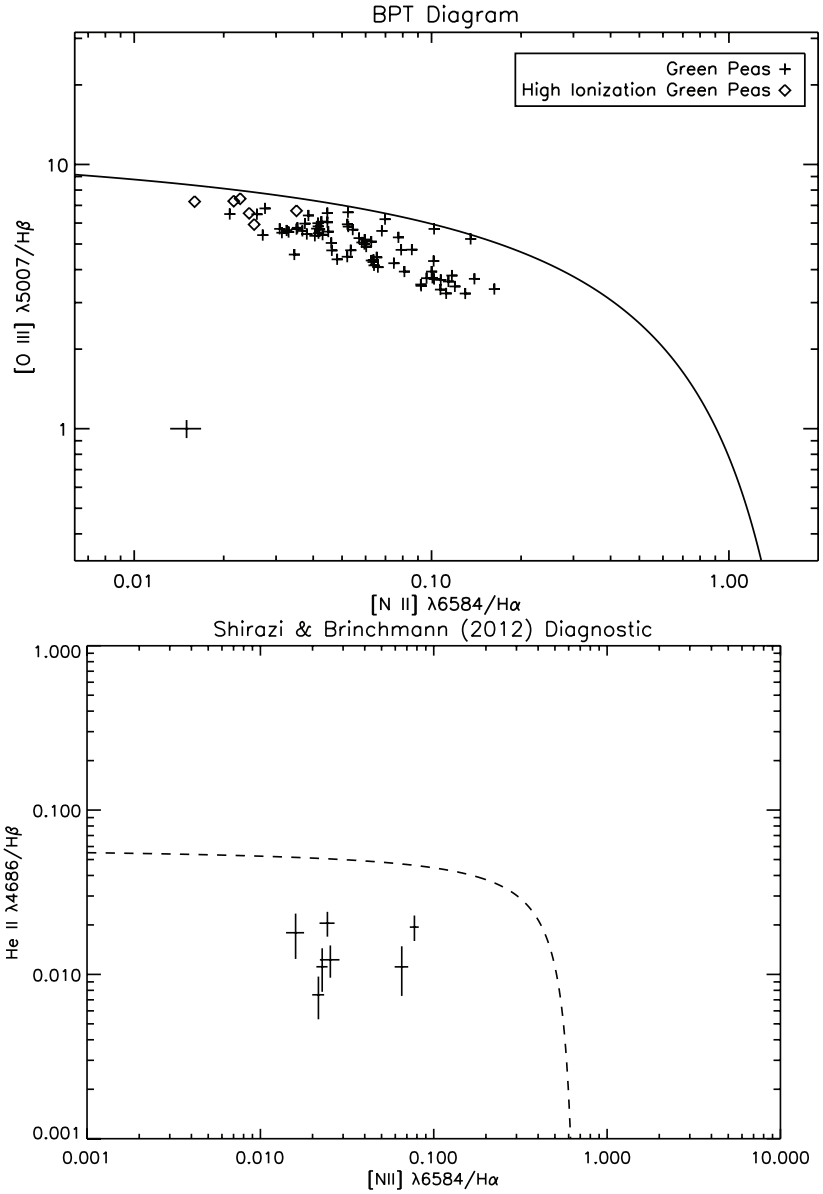

Figure 3.11: The top panel shows the GPs' positions on the BPT diagram (Baldwin et al., 1981). The solid line indicates the Kewley et al. (2001) extreme starburst line. The GPs lie close to the dividing line between starbursts and AGN. Representative 1σ errors for the extreme GPs are shown by the black cross in the lower left. The bottom panel shows the AGN diagnostic of Shirazi & Brinchmann (2012) for the GPs with He II λ4686 detections; the line indicates the point at which an AGN contributes 10% of the He II emission. In this diagram, the GPs are clearly separate from the AGN regime.

At a burst age of 4-5 Myr and $Z = 0.2\,Z_\odot$, Linden et al. (2010) predict the formation of 5 HMXBs with X-ray luminosities greater than $10^{36}\,\mathrm{ergs\,s^{-1}}$ per $10^6\,M_\odot$ burst. Four of these HMXBs would qualify as ultra-luminous X-ray sources (ULXs) with X-ray luminosities above $10^{39}\,\mathrm{ergs\,s^{-1}}$. The ULX population peaks at this age, while the HMXB population reaches its peak a few Myr later (Linden et al., 2010). Scaling these numbers to the calculated burst masses of the GPs, we would expect 68-854 luminous HMXBs and 54-683 ULXs at an age of 4-5 Myr. Kaaret et al. (2004) report the detection of strong He II λ4686 emission, with a luminosity of $2.7 \times 10^{36}\,\mathrm{ergs\,s^{-1}}$, around a ULX nebula in Holmberg II; the galaxy has a metallicity near $0.2\,Z_\odot$(Moustakas et al., 2010). Adopting this luminosity for the He II emission produced by a ULX, the extreme GPs would need 2100-11,000 ULXs to account for their He II luminosities. Even if the GPs are old enough to have an HMXB population, this number of ULXs is more than an order of magnitude larger than expected. The Grimm et al. (2003) relation between the SFR and the number of luminous HMXBs results in an even worse discrepancy, with only 20-89 HMXBs expected in the GPs. We conclude that HMXBs are an unlikely source of the observed He II emission.

3.3.5 Shocks

Guseva et al. (2000) and Thuan & Izotov (2005) propose fast, radiative shocks as a means of generating He II emission in galaxies without WR stars. In a study of BCDs, Thuan & Izotov (2005) observe emission from Ne^{4+} and Fe^{4+}, which have ionization potentials even higher than He^+. Radiative shocks can naturally account for the existence of these highly ionized emission lines. In addition, the [O III] $\lambda\lambda$4959,5007 and Hβ lines in the BCDs exhibit broad wings indicative of high velocity gas (Thuan & Izotov, 2005). Observations of the BCD SBS 0335-052E show that the He II and [Ne V] emission originate in a separate region from the [Ar IV] and [O III] emission (Izotov et al., 2006). The latter emission lines are likely photoionized by the youngest

clusters in the galaxy. The He II emission, on the other hand, is associated with older clusters, which supports an interpretation of supernova remnant (SNR) shock ionization (Izotov et al., 2006), as in the aged starburst hypothesis of Overzier et al. (2009). Thuan & Izotov (2005) argue that fast, radiative shocks are most effective in dense, low-metallicity, super star clusters, conditions which likely characterize the star-forming environments of the GPs.

Supernovae, galactic outflows, or mergers could lead to fast shocks (Shirazi & Brinchmann, 2012), and the GPs show evidence for these processes. Broad emission-line wings and multiple velocity components indicate high-velocity inflows and outflows in the GPs (Amorín et al., 2012b). The GPs' offset in the mass-metallicity relation likewise suggests the presence of low-metallicity gas inflows or metallicity-dependent, supernova-driven outflows (Amorín et al., 2010). Merger-induced shocks may also be present, as shown by the disturbed morphologies and presence of companion galaxies in *HST* images of the GPs (Overzier et al., 2008; Cardamone et al., 2009).

We detect emission from [O I] λ6300 and [N I] λ5200, which are characteristic of shocks. Weak [N I] emission is visible in J1012+13's spectrum as well as in the stacked spectra. We do not detect the [Ne V] or [Fe V] lines discussed by Thuan & Izotov (2005), but their data show that these lines are substantially weaker than He II. Another non-detected shock line is [Mg I] λ4571. The Mappings III shock models of Allen et al. (2008) show that low ratios of [Mg I]/He II can only be obtained for high magnetic field strengths, $\gtrsim$10μG. Magnetic field strengths of 20-50μG have been observed in starburst galaxies (e.g., Klein et al., 1988; Chyży & Beck, 2004), and radio observations indicate that the GPs have similar magnetic field strengths of $> 30\mu$G (Chakraborti et al., 2012), consistent with the non-detection of [Mg I]. Figure 3.12 shows the detected and non-detected shock lines in the stacked spectrum of the high ionization GPs.

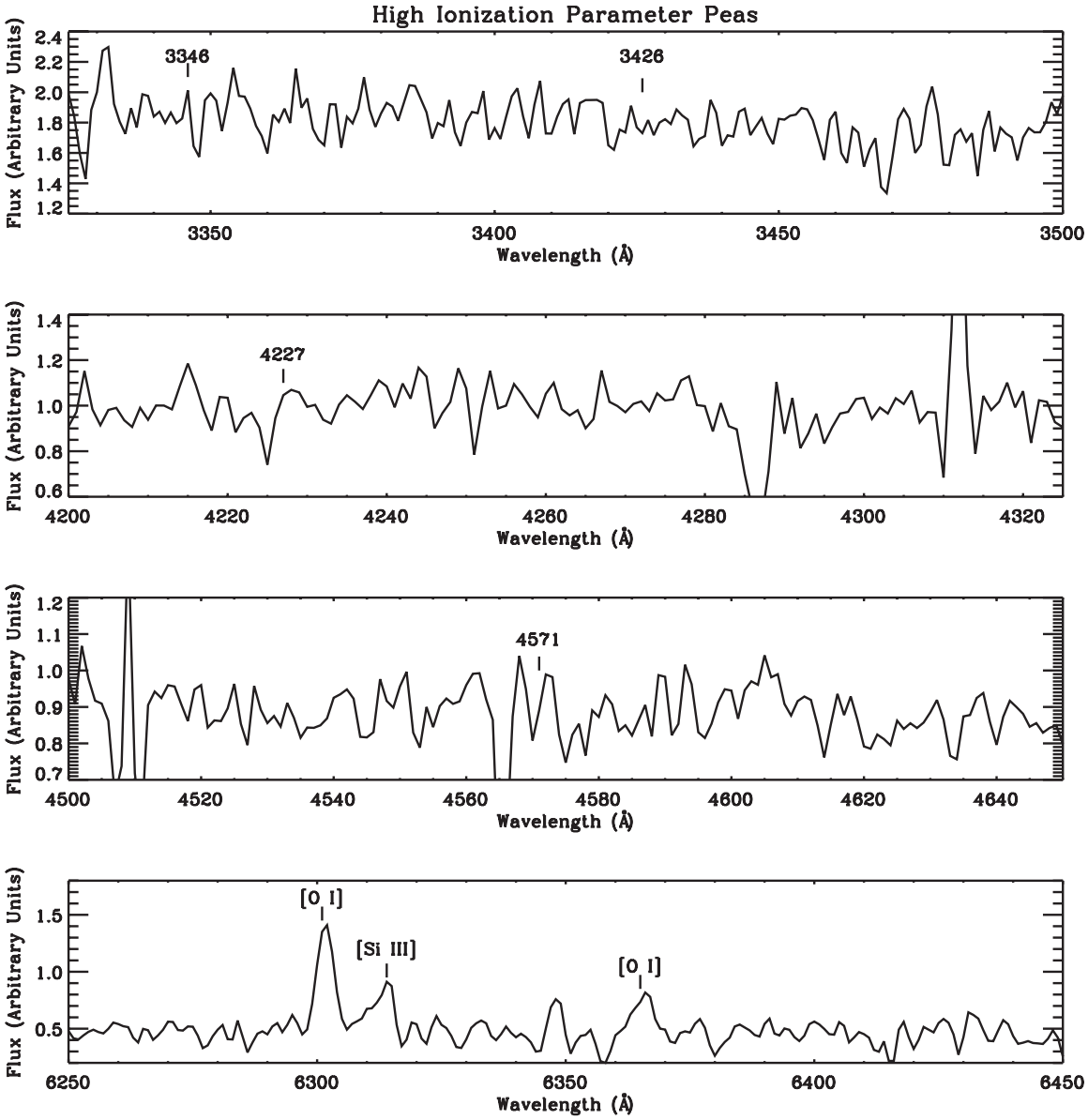

Figure 3.12: The panels show the stacked spectrum of the high [O III]/[O II] ratio GPs for the spectral regions near shock lines. [Ne V] λ3346, [Ne V] λ3426, [Fe V] λ4227, and [Mg I] λ4571 are not detected. The positions of these wavelengths are indicated. [O I] λ6300 is shown in the bottom panel.

From the Mappings III shock model grids (Allen et al., 2008), the observed He II/[O I] ratios in the extreme GPs support shock velocities between $\sim$ 200 and $\sim$ 700 $\mathrm{km\,s^{-1}}$. The observed Hα full-width-at-zero-intensity values show that the GPs do have gas moving at these velocities. In the extreme GPs, these broad wings range from $\sim \pm$400-800 $\mathrm{km\,s^{-1}}$, similar to the velocities observed by Thuan & Izotov (2005). We do not detect any significant velocity shift in the centers of the He II or [O I] lines, and their FWHM values are similar to the Hα FWHM. Higher resolution observations are necessary to determine whether the He II emission has any unusual velocity components.

Both shocks and photoionization may contribute to the observed nebular emission. To analyze the ionizing spectrum and the optical depth, therefore, we need to subtract the shock contribution. We use the Allen et al. (2008) Mappings III models at SMC and LMC metallicity and assume that all the observed He II λ4686 emission comes from shocks. We include emission from the shock's precursor, pre-shock gas that is photoionized by UV and X-ray emission produced in the shock (Allen et al., 2008). We then derive the intrinsic photoionized line ratios using

$$\frac{A}{H} = \frac{A_0 - A_s}{H_0 - H_s} = \frac{\frac{A_0}{H_0}X - \frac{A_s}{H_s}}{X - 1}, \tag{3.4}$$

where

$$X = \frac{\left(\frac{\mathrm{HeII}\lambda 4686}{H}\right)_s}{\left(\frac{\mathrm{HeII}\lambda 4686}{H}\right)_o} \tag{3.5}$$

and

$$\mathrm{HeII}\lambda 4686_o = \mathrm{HeII}\lambda 4686_s. \tag{3.6}$$

In the above equations, A is the emission line flux of interest, H is the Hβ line flux, the subscript o indicates observed values, and the subscript s indicates the modeled shock values. In addition to the two metallicities, we use the modeled shock values for magnetic field strengths of 0.5-10 μG and velocities from 300-1000 $\mathrm{km\,s^{-1}}$.

Figures 3.13 and 3.14 compare the corrected photoionized line ratios for the two youngest GPs with the Starburst99 and CLOUDY models described in §3.3.2.1. We have omitted the other GPs from these figures for clarity; the other extreme GPs exhibit similar trends.

The models show that when the additional flux contribution of shocks is taken into account, the optical depth implied by the nebular line ratios decreases. As the shock contribution to lower ionization lines, such as [O II], increases, the intrinsic photoionized [O III]/[O II] ratio increases, and the GPs move into the density-bounded, optically thin regime. Furthermore, the presence of shocks can raise the Hα/Hβ ratio, leading to an overestimate of the dust extinction (Nakajima et al., 2013). If the dust abundance is overestimated, the GPs' [O II]/Hβ ratios should be lower, and their [O III]/[O II] ratios should be higher. This change would also move the GPs farther into the optically thin regime, in a direction opposite to the reddening arrow in Figures 3.6-3.9 and 3.13-3.14. The inferred optical depth of the GPs depends strongly on the inner nebular radius and shock properties assumed, however. In particular, lower velocity shocks have a larger effect on the inferred optical depth. The shock emission also depends on the density, which may differ from the density of the photoionized gas. The SMC and LMC shock models of Allen et al. (2008) have a fixed density of 1 cm^{-3}. The Mappings III solar metallicity models indicate that higher density shocks may have less effect on the GPs' observed line ratios. If the density of the shock-heated gas is greater than 1 cm^{-3}, the inferred optical depth would be greater than that implied by Figures 3.13-3.14. An additional uncertainty comes from the modeled magnetic field strength, which is somewhat weaker than the GPs' magnetic fields.

Although the presence of shocks shifts the GPs toward lower optical depths, the galaxies' line ratios still appear offset to higher [O II]/Hβ ratios and/or lower [O III]/[O II] ratios by factors of $\sim$1.5-2 relative to the $n < 1000$ cm^{-3} model grids

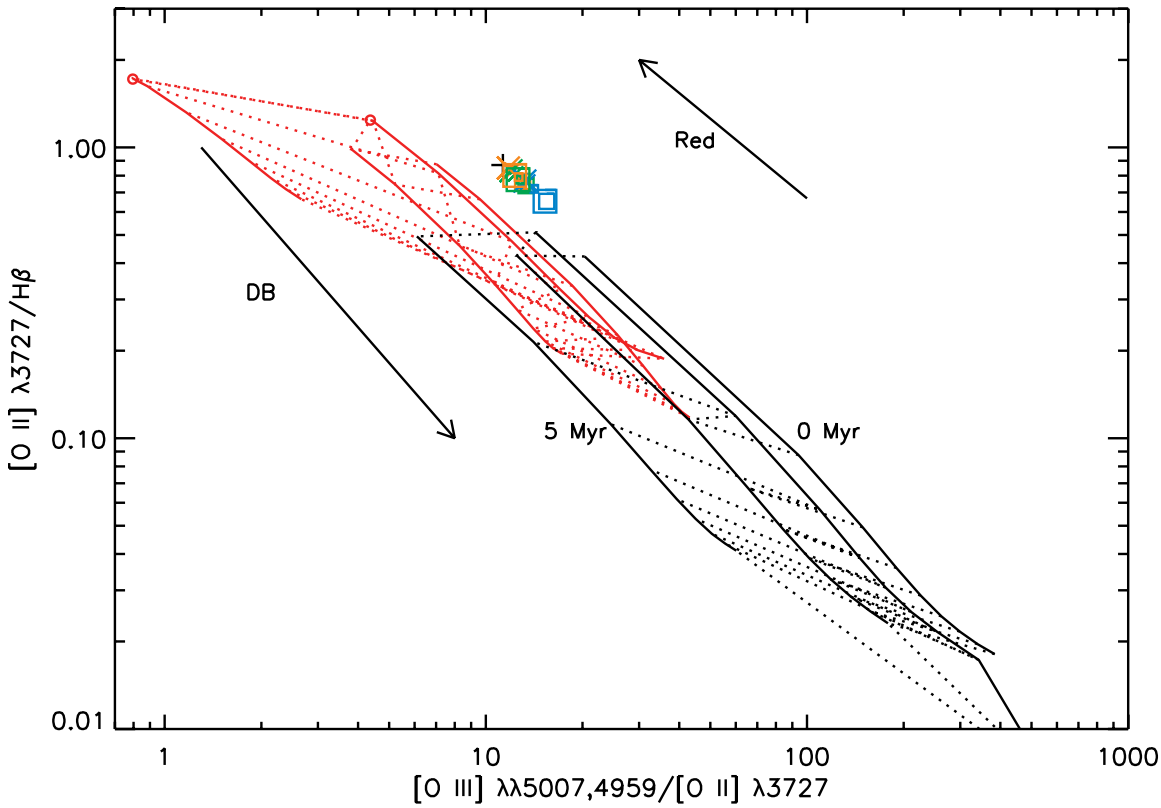

Figure 3.13: The grid is described in Figure 3.6. The figure shows the CLOUDY and Starburst99 grids for $n_{\rm H} = 300$ cm^{-3} and a filling factor of 0.1. The black cross indicates the observed ratios of J1012+13 and the associated 1σ errors. The squares and X's indicate the line ratios with the shock contribution subtracted. The squares correspond to shock models at LMC metallicity, and the X's indicate SMC metallicity. The symbol size indicates the magnetic field strength; large symbols correspond to 10 μG models, intermediate-size symbols correspond to 3.23 μG, and small symbols correspond to 0.5 μG. Symbol colors denote shock velocity: blue for 300 km s^{-1} models, green for 500 km s^{-1} models, and orange for 1000 km s^{-1} models. Accounting for a shock contribution to the GPs' emission decreases their inferred optical depth.

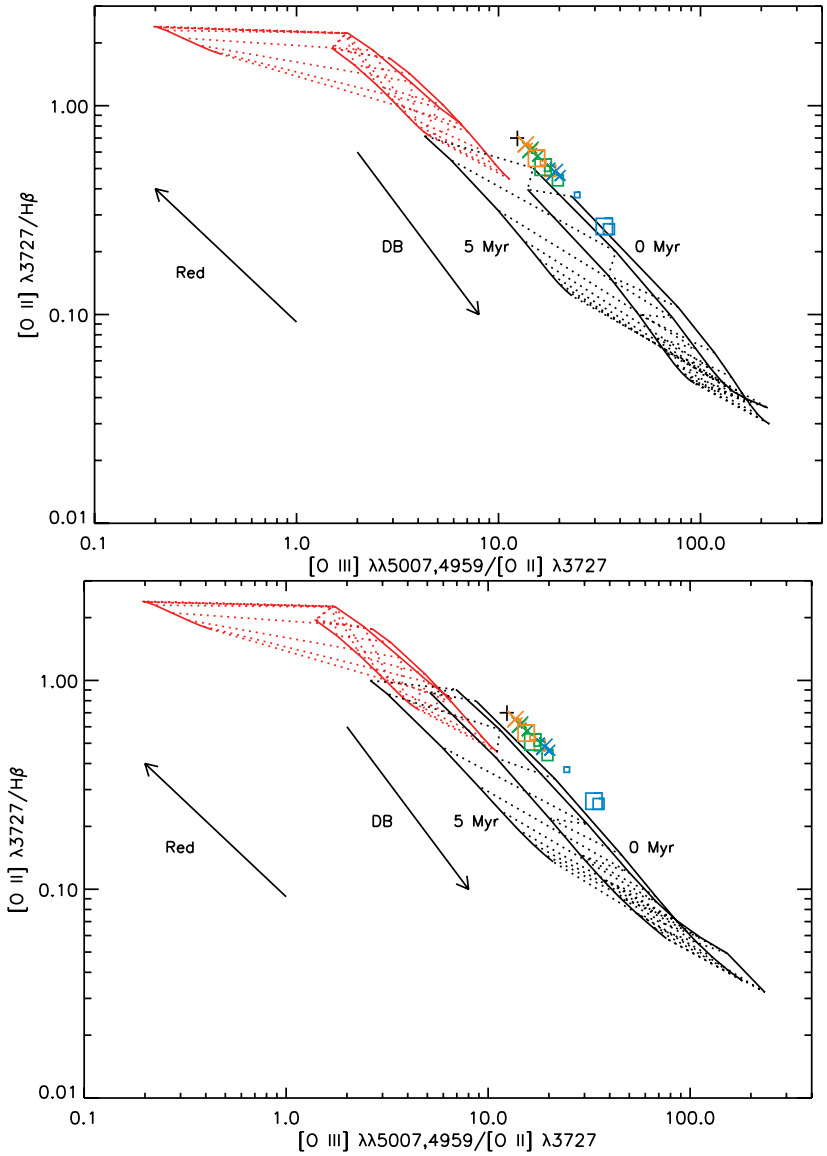

Figure 3.14: The grid is described in Figure 3.6, and the symbols are described in Figure 3.13. Both panels show the CLOUDY and Starburst99 grids for $n_{\rm H}$=1000 cm^{-3}. The model in the top panel uses a filling factor of 0.1, and the bottom panel uses a filling factor of 0.01. The black cross indicates the observed ratios of J1219+15.

(see e.g., Figure 3.13). One possible explanation for this offset is that higher density models are more appropriate for the extreme GPs. If shocks are indeed present, they may contribute a substantial fraction of the observed [S II] emission, which may lead to incorrect density estimates (§3.2). The existence of lower ionization nebulae within the GPs may also resolve the discrepancy. If low ionization nebulae contribute a fraction of the observed [O II] emission, they could account for the higher [O II]/Hβ and lower [O III]/[O II] ratios relative to the grids. Adopting lower reddening corrections or higher metallicities for the GPs could also lessen the offset; however, the uncertainties in these quantities are too low to completely explain the disagreement. Finally, as mentioned in §3.3.2, a population of hot, low-metallicity stars could provide an additional means of increasing the [O III]/[O II] ratio. Given the current lack of evidence for such stars, however, we conclude that the presence of multiple nebulae and higher densities in the star-forming regions are the more likely explanations.

Despite these uncertainties, the CLOUDY models show that including shock emission lowers the inferred optical depths of the GPs. If the shocks are due to SN activity, the GPs must be old enough for such events to take place. As a test, we consider Pea J1012+13, the highest EW Pea and potentially the youngest. Our results for the other extreme GPs are comparable. From the observed He II luminosity and the modeled He II/Hα ratios, we estimate how many SNe are necessary to account for the He II emission. Assuming all the He II is due to shocks, the modeled He II/Hα ratios imply that shocks provide 5.6×10^{40}-4.5×10^{41} ergs s^{-1} of Pea J1012+13's Hα luminosity. The Hα luminosities of SNRs range from $\sim 10^{36}$ to $\sim 10^{38}$ ergs s^{-1} (de Grijs et al., 2000). If we assume an intermediate SNR luminosity of 10^{37} ergs s^{-1}, then Pea J1012+13 would need 5600-45,000 SNe ($\sim$4-50% of its O stars) to reach the necessary He II and Hα luminosities. While the former value could be reached in less than 4 Myr following an instantaneous burst, the latter value requires more than 6 Myr. However, if the SNRs are extremely bright (10^{38} ergs s^{-1}), as might be

expected for a young burst, than the required number of SNe drops to only 560-4500, 0.4-5% of Pea J1012+13's O stars. The first SNe at ∼3.5-4 Myr could provide the necessary Hα and He II luminosities. The ages for the continuous star formation case are similar; 5000 SNe would go off within the first 5 Myr.

One example of a Pea-like galaxy that may have shock-induced He II emission is II Zw 40, a nearby BCD that shares many properties with the GPs. It has a metallicity of 0.2 $Z_{\odot}$and an Hβ EW of 272Å (Guseva et al., 2000), suggesting a similar age to the GPs. In addition, II Zw 40 has detectable WR features, including the blue bump and Si III λ4565, but the blue bump is dominated by the much stronger nebular emission of He II, [Fe III], and [Ar IV] (Guseva et al., 2000). The much weaker strength of the WR features compared to the nebular emission shows that these features could easily be below our detection limits. Based on the similarities between He II-emitting galaxies with and without WR features, Guseva et al. (2000) suggest that shocks generate some of the nebular He II emission, even in WR galaxies. The presence of weak [Fe V] λ4227 emission and high-velocity emission-line wings in II Zw 40 supports the shock hypothesis (Thuan & Izotov, 2005). Although II Zw 40 is unlikely to be optically thin (e.g., Joy & Lester, 1988; Beck et al., 2002), it shows that shock ionization of He II is feasible at the GPs' metallicities and ages. Thus, even if WR stars are present in the GPs, shock heating may still be the primary origin of the high ionization nebular lines.

The above analysis demonstrates that shock-heating from the earliest SNe could account for the observed He II emission. In addition, shocks due to a galaxy merger or gas infall could occur even earlier, and younger ages for the GPs could be possible. If shocks are present, the GPs' high [O III]/[O II] ratios may indicate a low optical depth.

3.4 Consequences for the Optical Depth

The source of the high ionization emission in the extreme GPs could be WN9 stars, photoionization from early-type WR stars or chemically homogeneous O stars, shocks, or some combination of these sources. Each of these sources has different implications for the escape of ionizing radiation, which we now discuss.

If the He II emission is a stellar feature or due to stellar photoionization, the GPs' optical depth is ambiguous. Low density models, with $n < 100$ cm^{-3} indicate a high optical depth. At higher densities, consistent with the GPs' [S II] ratios, whether or not the GPs are optically thin depends on the inner nebular radius and the filling factor. For instance, decreasing the filling factor of the dense gas decreases the inferred optical depth (see Figures 3.6 and 3.8).

Increasing the inner radius lowers the ionization parameter; the high [O III]/[O II] ratios we observe would then have to be due to a low optical depth. Unlike the CLOUDY models, the emission from the GPs is not likely to originate from a single H II region. However, if the emission is dominated by one cluster or several similar clusters, we can estimate which CLOUDY model geometries may be most reasonable.

The stellar winds of WR stars may blow cavities of 50 pc or more in the ISM (e.g., Oey, 1996), and SN explosions will expand the superbubble cavity further. The broad wings in the GPs' Hα emission may already indicate that stellar feedback is evacuating gas around the star clusters and driving galactic winds (Amorín et al., 2012b). Strickland & Stevens (1999) simulate a superbubble around a 10^5 M$_\odot$ cluster at 0.25 Z$_\odot$, expanding into an ambient medium with density $n = 100$ cm^{-3}. The superbubble cavity reaches a radius of 50 pc within 3.5 Myr and expands to 70 pc within 4.5 Myr. The radius scales with cluster mass as $R \propto (M/n)^{1/5}$ (Castor et al., 1975; Strickland & Stevens, 1999), so for our 10^6 M$_\odot$ Starburst99 simulation, the cavity radii should be 79 and 111 pc, respectively. If we increase the density by a factor of 10, as appropriate for Pea J1219+15, the radii remain 50-70 pc. Therefore,

for our $10^6\,M_\odot$ starburst CLOUDY models, the models with inner radii greater than 50 pc may have the most realistic geometries. Models with these inner radii and $n > 100$ cm^{-3} generally indicate a low optical depth (see Figure 3.9).

The exact optical depth of the GPs also depends on their age and the resulting ionizing spectrum. For instance, Figure 3.6 shows that for a given inner radius, a 5 Myr-old model gives a slightly lower optical depth than a 4 Myr-old model. The ionizing spectrum of chemically homogeneous O stars is highly uncertain, and the existence of 60,000 K homogeneous stars has not been observationally confirmed. We cannot determine the optical depth of the GPs if their ionization is due to a chemically homogeneous population. Thus, while we cannot assess the precise optical depth of the extreme GPs, a low optical depth remains plausible, particularly for the GPs with the highest densities.

As discussed in §3.3.5, including a shock contribution to the GPs' line fluxes decreases estimates of their optical depth. This same situation is apparent in the spectra of DEM L301, an LMC superbubble. Oey et al. (2000) show that a combination of shock-heating and density-bounding explain DEM L301's emission, although at first glance, the line ratios appear to indicate radiation-bounding. Voges et al. (2008) confirm that DEM L301 is indeed optically thin.

Not only do SNe affect the nebular emission, but they may actually promote a low optical depth. As SN-driven bubbles expand in the ISM and eventually blow out of the galaxy, they create low-density passages that aid photon escape (Clarke & Oey, 2002). Like Lyman-break galaxies, the GPs have large SFRs and spatially distributed star formation, which enhance the ISM porosity (Clarke & Oey, 2002). In addition, with their young ages, the GPs may be at the optimal time for the escape of Lyman-continuum radiation; they are old enough for SNe and stellar winds to begin to reshape the ISM, but young enough to possess large numbers of UV-luminous massive O or WR stars.

The CLOUDY models for the WR and shock-heating scenarios at $n = 100$ cm^{-3} are generally optically thick or borderline optically thin. Models at higher densities favor lower optical depths but could still be consistent with optically thin nebulae if the inner radii are sufficiently small and shocks are negligible. Nevertheless, at all densities, the GPs may be more optically thin than the models suggest. For instance, optically thick clumps tend to dilute the signature of density-bounding (e.g., Oey et al., 2000; Giammanco et al., 2005). The CLOUDY models further assume that the emission originates from a single nebular region or identical nebulae. In reality, the emission is the sum of the emission from multiple nebulae, which may have different levels of ionization. Low-ionization emission from other nebulae or a companion galaxy could lower the observed [O III]/[O II] ratios and cause the gas to appear more optically thick than it actually is.

The extreme GPs may therefore have high escape fractions for ionizing radiation. However, further observations are needed to diagnose their optical depths and distinguish among the potential ionizing sources. We are obtaining deeper spectra of the extreme GPs to confirm or refute the existence of shocks and to constrain the WR population. Observations of massive stars in low-metallicity galaxies are also critical to understand homogeneous stellar evolution and the stellar spectra of low-metallicity O and WR stars.

3.5 Summary

The Green Peas (GPs) are a rare class of compact, emission-line galaxies at $z = 0.1 - 0.3$ with unusually powerful [O III] emission and the potential for a high escape fraction. Through their high ionization emission, extreme star-formation intensities, and clumpy morphologies, the GPs provide a glimpse of massive star feedback and ionizing photon propagation in high redshift galaxies. While the large [O III]/[O II] ratios of the GPs may indicate a low optical depth, high ionization lines

such as He II and [Ar IV] in the SDSS spectra show evidence for strong, high-energy emission. Using stellar population and nebular photoionization models, we have investigated the ionizing sources and optical depths for six of the highest ionization GPs.

The six extreme GPs are young and powerful starbursts, with high electron temperatures of $\sim 15,000$ K and densities of 100-1000 cm^{-3}. Their high Balmer-line EWs indicate young ages of 3.7-5.1 Myr, according to Starburst99 instantaneous burst models. We detect the He I λ3819 line in emission in several objects and in stacked spectra, which corroborates the young ages. The λ3819 line sets an upper limit of 3 Myr on the ages for an instantaneous burst and 10 Myr for continuous star formation (González Delgado et al., 1999).

The GPs' young ages and the presence of He II λ4686 emission set strong constraints on the possible ionizing sources in the GPs. No WR features are visible in stacked spectra of the GPs. However, we tentatively detect WR features in GPs J1012+13, J1457+22, and J0303-08. The narrow FWHMs (3-5 Å) of the He II emission suggest a nebular origin or a narrow WNL stellar feature.

Using the WNL line luminosities of Brinchmann et al. (2008) and Guseva et al. (2000), we calculate the number of WNL stars necessary to produce the observed λ4686 emission as a stellar feature. The high resulting WR/O ratios and the 3σ Si III λ4565 detection limits rule out the required WNL population for the $Z < 0.2\,Z_\odot$ case, but not the $Z \geq 0.2\,Z_\odot$ case. However, the implied numbers of WNL stars are unrealistically high, and the higher-metallicity WNL population is inconsistent with the GPs' low measured metallicities.

Alternatively, the observed He II may result from photoionization by hot stars. CLOUDY photoionization models (Ferland et al., 1998) of single-star H II regions demonstrate that ordinary O stars are not hot enough to provide the necessary He^+-ionizing flux. CLOUDY models using early-type WR stars, with core temperatures

above 70,000 K, fit most of the observed line ratios. From the ionizing photon rates of Smith et al. (2002), we estimate the number of WNE and WCE stars needed to produce the observed He II. The resulting WR/O ratios are consistent with Starburst99 instantaneous burst models, but the lack of broad He II emission in most objects eliminates the WCE stars as the dominant cause of the emission. Starburst99 and CLOUDY models likewise show that only 4-5 Myr starbursts, which contain a substantial WR population, can simultaneously match the GPs' [O III]/[O II] and He II emission.

Putative chemically homogeneous O stars could explain He II emission in galaxies without WR features (Shirazi & Brinchmann, 2012). These stars may form at low metallicity (e.g., Maeder, 1987; Yoon et al., 2006) and can theoretically reach effective temperatures much higher than ordinary O stars (Brott et al., 2011a). CLOUDY single-star H II region models with the 60,000 K stellar model of Kudritzki (2002) demonstrate that such hot O stars could account for the observed He II. In addition, the presence of extremely hot O stars may be necessary to match the observed [O II]/Hβ and [O III]/[O II] ratios of the GPs. More research is needed to determine whether homogeneous O stars exist, however, and how many ionizing photons they produce.

We rule out an AGN contribution to the He II emission at the 10% level, using the diagnostic diagram of Shirazi & Brinchmann (2012). Likewise, we find that HMXBs cannot be the source of the He II ionization. Using the models of Linden et al. (2010), we calculate the expected number of luminous HMXBs in the GPs. Even assuming that each HMXB is a ULX, with the high nebular He II λ4686 luminosity of Holmberg II X-1 (Kaaret et al., 2004), the resulting emission is an order of magnitude too low.

Fast, radiative shocks are an alternative mechanism for the production of He II (Guseva et al., 2000; Thuan & Izotov, 2005), and the existence of fast shocks is supported by the high velocity Balmer-line wings (Amorín et al., 2012b) and [O I] and [N I] emis-

sion in the GPs. To account for the contribution of shocks to the observed emission, we use the line emission predictions of the Mappings III shock models (Allen et al., 2008) for different magnetic field strengths and velocities. Assuming shocks generate all of the He II emission, we subtract the shock contribution from the observed line ratios. After correcting for shock emission, the nebular line ratios indicate a lower optical depth, particularly for slower shocks. Based on the Hα luminosities from the shock models, the first SNe, exploding 3.5-4 Myr after an instantaneous burst, could produce the observed He II emission. Younger ages could be possible if infalling gas or mergers are the cause of the shocks.

Although the precise origin of the He II emission is still uncertain, the CLOUDY models show that the GPs may be optically thin. Models with higher densities and larger inner radii imply lower optical depths. If the He II is due to WR stars, models with inner radii ≥ 50 pc and densities ~ 100 cm^{-3} support both optically thick and optically thin scenarios, while models with the same inner radii and $n = 1000$ cm^{-3} support a low optical depth. Including the effects of shocks lowers the estimated optical depth further, and the presence of density inhomogeneities or emission from multiple nebulae may also lead us to overestimate the optical depth.

The low levels of extinction, intense star formation, and young ages of the GPs make them ideal candidates for escaping ionizing radiation. The nebular emission of the GPs with the highest [O III]/[O II] ratios, their high densities, and the likely presence of shocks in these objects suggest that they may be leaking ionizing photons into the IGM, and their ages may optimize photon escape. In these 3-4 Myr starbursts, stellar feedback is likely beginning to carve out passages in the ISM for the escape of ionizing photons, while large numbers of massive stars are still available to produce Lyman-continuum photons. However, the data are still inconclusive, and future observations are necessary to establish the escape fraction of the GPs. These galaxies offer a rare opportunity to study high-redshift star formation conditions, the

effects of stellar feedback on the ISM, and the propagation of ionizing photons from star clusters to the IGM.

CHAPTER IV

Linking Lyα, Low-Ionization Transitions, and Optical Depth in Extreme Starbursts

4.1 Introduction

Lyman continuum (LyC) radiation from star-forming galaxies likely caused the reionization of the universe (e.g., Bouwens et al., 2012), but to date, studies have identified few galaxies that are LyC emitters (LCEs; e.g., Leitherer et al., 1995; Heckman et al., 2001; Leitet et al., 2013; Nestor et al., 2013). At low redshift, the Green Pea (GP) galaxies, starbursts characterized by intense [O III] λ5007 emission, have emerged as LCE candidates (Jaskot & Oey, 2013; Verhamme et al., 2014, hereafter V14). The high [O III]λ5007/[O II]λ3727 ratios of the GPs imply an enormous ionization parameter. However, since optically thin nebulae should underproduce [O II] (e.g., Giammanco et al., 2005; Pellegrini et al., 2012), these high ratios may also indicate a low LyC optical depth. Notably, the $z < 0.3$ GPs share several properties with Lyα emitters (LAEs) at $z > 2$, including high specific star formation rates, compact sizes, low extinction, and elevated [O III]/[O II] ratios (e.g., Hagen et al., 2014; Malhotra et al., 2012; Gawiser et al., 2007; Nakajima & Ouchi, 2014). Thus, the GPs may be outstanding analogs of both high-redshift LyC-emitting and Lyα-emitting galaxies.

Some LAEs are known LCEs (e.g., Iwata et al., 2009; Nestor et al., 2013) and several studies have proposed a connection between Lyα emission and a low LyC optical depth (e.g., Shapley et al. 2003; Nakajima & Ouchi 2014; V14). Due to the resonant nature of Lyα, most galaxies have low Lyα escape fractions (e.g., Hayes et al., 2011). The geometry and kinematics of the neutral interstellar medium (ISM) appear to control the Lyα escape fraction (e.g., Giavalisco et al., 1996; Thuan & Izotov, 1997; Kunth et al., 1998), with low neutral gas covering fractions and strong outflows enabling Lyα escape (e.g., Shapley et al., 2003; Kornei et al., 2010). While many numerical models have considered the effects of strong scattering through the ISM or outflows on Lyα line profiles (e.g., Ahn et al., 2000; Zheng & Miralda-Escudé, 2002; Verhamme et al., 2006; Orsi et al., 2012), recent studies have focused on Lyα radiative transfer through an optically thin medium (Behrens et al. 2014; V14). By driving outflows and ionizing the surrounding ISM and circumgalactic medium, feedback from the intense star formation in some galaxies, like the GPs, may create optically thin conditions that enable LyC and Lyα escape.

In this Chapter, we suggest that LyC optical depth and outflow geometry link the Lyα profiles, C II absorption, and C II* emission observed in high-redshift galaxies. We demonstrate this connection using *Hubble Space Telescope (HST)* Cosmic Origins Spectrograph (COS) observations of four of the most extreme GPs, galaxies that closely resemble high-redshift LAEs. We report the detection of Lyα emission in all four GPs. Three GPs show P-Cygni Lyα line profiles; the profile shapes and equivalent widths (EWs) $>$ 70Å in two GPs imply a relatively low optical depth. We also suggest that the enigmatic non-resonant emission in C II* and Si II* that is observed to correlate with Lyα emission from starbursts is consistent with the geometry, optical depth, and viewing orientation associated with the GPs' galactic outflows. We will show that the Lyα emission strengths, Lyα profile shapes, and weak interstellar absorption lines in two extreme GPs demonstrate that some starbursts

with high [O III]/[O II] may be optically thin to the LyC.

4.2 Results

We present *HST* COS spectra of two GPs (J081552.00+215623.6 and J145735.13 +223201.8) and analyze archival observations for two additional GPs (J121903.98 +152608.5 and J030321.41-075923.2). Jaskot & Oey (2013) identify these four starbursts as LCE candidates due to their high [O III]/[O II] ratios. All four GPs have similar optical nebular spectra, metallicities ($\sim 0.2\,Z_{\odot}$), extinctions ($E(B-V) = 0.06-0.11$), and young ages (Hα EW$= 700-1300$ Å), but differ markedly in their ultraviolet (UV) spectra (Figures 4.1 and 4.2 and Table 4.1). We bin the COS spectra to $0.15-0.23$ Å per pixel, the resolution for emission at the GPs' NUV half-light radii (Table 4.1), as measured from the COS acquisition images (e.g., B. James et al., in prep). Galactic Si II λ1526.71 absorption lines show that the wavelength scale is accurate to within one binned pixel. At the GPs' redshifts, the COS aperture samples 6-8 kpc and fully encompasses the detected NUV emission. However, Lyα emission may originate at larger radii (e.g., Hayes et al., 2013). Based on the GPs' NUV Petrosian radii (Petrosian, 1976) at the $\eta = 0.2$ surface brightness level and the average ratio of Lyα radii to FUV radii in Hayes et al. (2013), we expect the COS aperture to capture all of the Lyα emission. Even adopting the ratio for the most extended Lyα halo in Hayes et al. (2013), the COS aperture should probe $60-100\%$ of the Lyα Petrosian radius and recover most of the Lyα flux. We use the redshifts given in the Sloan Digital Sky Survey (SDSS) Data Release 9 (Ahn et al. 2012), which are based on the GPs' optical emission lines. We adopt a cosmology with $H_0 = 70$ km s^{-1} Mpc^{-1}, $\Omega_m = 0.3$, and $\Lambda_0 = 0.7$.

4.2.1 Lyα Emission

In the conventional scenario for Lyα emission, Lyα scatters many times before escaping, which leads to a significant broadening of the original line profile. However, the Lyα profiles in the two GPs with the highest [O III]/[O II] ratios, J0816+22 and J1219+15, do not show the predicted effects of radiative transfer at high column density. The Lyα profiles in these two GPs resemble a Gaussian with P Cygni-like absorption superimposed at the systemic velocity; both galaxies have a small separation ($<$300 km s^{-1}) of the Lyα peaks, (Figure 4.1), as expected for a neutral column density $N_{\rm HI} < 10^{18}$ cm^{-2} and optical depth at the Lyman edge $\tau \lesssim 6$ (V14). Indeed, V14 note that a density-bounded scenario could explain the Lyα profile of J1219+15.

In contrast, the Lyα profiles in the other two GPs, J0303-08 and J1457+22, are consistent with higher Lyα optical depths. J0303-08 exhibits a classic P-Cygni profile, with deeper, blue-shifted absorption, a weaker blue peak, and a greater separation of the emission peaks (Figure 4.1c and Table 4.1) than J0816+22 and J1219+15, implying a higher optical depth. This GP appears slightly more extended than the others and consists of multiple UV-emitting knots; thus, the COS aperture may miss some of the scattered emission. J1457+22 appears to have the highest line-of-sight column density, as indicated by the $\sim$750 km s^{-1} velocity separation of its emission peaks (e.g., V14) and the broad absorption component extending to either side of the Lyα emission (Figure 4.1d). The weak, double-peaked profile of J1457+22 resembles models of Lyα emission from highly inclined galaxies (Verhamme et al., 2012).

The P-Cygni Lyα profiles of J0816+22, J1219+15, and J0303-08 are strikingly similar to Hα emission line profiles observed from stellar sources, such as symbiotic binaries (e.g., Fig. 4 of Burmeister & Leedjärv 2009) and luminous blue variables (LBVs; e.g., Fig. 4 of Weis 2003). Double-peaked Hα emission lines with weakly blue-shifted absorption are particularly common in symbiotic binaries (e.g., Quiroga et al.,

2002; Burmeister & Leedjärv, 2009), which consist of a hot compact star interacting with the wind of a red giant. The Hα emission forms in the gas ionized by the hot star, while self-absorption from neutral gas in the red giant's wind may cause the central absorption dip (e.g., Ivison et al., 1994; Quiroga et al., 2002). Similar Balmer line profiles arise in LBVs (e.g., Nota et al., 1997; Weis, 2003) and proto-planetary nebulae (e.g., Balick, 1989; Sánchez Contreras et al., 2008). In each of these cases, photons from an expanding ionized region or bipolar outflow encounter cooler surrounding material, often ejected by the central object.

The narrow line profiles of J0816+22 and J1219+15 suggest a lower-than-expected Lyα optical depth and possible LyC escape. In addition, the Lyα profiles' resemblance to the Balmer line profiles of stellar sources indicates that they may originate from a similar geometry, with a thin layer of neutral hydrogen obscuring a compact ionizing source. As a resonant transition, Lyα photons generally experience numerous scatterings. In contrast, the similarity of the GPs' Lyα to emission profiles from a *non-resonant* transition argues that Lyα is escaping relatively unimpeded from these objects, with a reduced number of scatterings.

To illustrate this point, we estimate the intrinsic Lyα profiles of J0816+22 and J1219+15 from their SDSS Hα profiles (Figure 4.3) scaled by the Case B Lyα/Hα ratio of 8.7 (Brocklehurst, 1971). The Lyα emission wings extend beyond the estimated intrinsic profiles, suggesting scattered emission. Similarly, scattering likely causes the broad Hα wings in symbiotic star spectra (e.g., Lee, 2000). The Lyα profile still preserves the signature of the intrinsic emission, however, and the Lyα peaks are located near or within the intrinsic profile. In Figure 4.4, we neglect the central absorption and fit the Lyα emission of J0816+22 and J1219+15 with a sum of two Gaussian functions or with a Voigt profile. Based on the adjusted R^2 goodness-of-fit statistic, these models are preferable to a single Gaussian fit, although the improvement is marginal for J0816+22. The narrow components of the double-Gaussian fits have

FWHM values of 280 $\mathrm{km\,s^{-1}}$ for J0816+22 and 220 $\mathrm{km\,s^{-1}}$ for J1219+15 and the Gaussian components of the Voigt fits have FWHM=230 $\mathrm{km\,s^{-1}}$ and 100 $\mathrm{km\,s^{-1}}$ respectively. These velocities are similar to the FWHM of the Hα profiles: 180 $\mathrm{km\,s^{-1}}$ for J0816+22 and 150 $\mathrm{km\,s^{-1}}$ for J1219+15 although these widths are uncertain given the $\sim$150 $\mathrm{km\,s^{-1}}$ SDSS spectral resolution. The narrow peak separations and presence of narrow emission components suggest that Lyα photons do not need to scatter to high velocities in order to escape. In addition, the strength of the blue peak indicates that this escape is due to a low column density rather than a high velocity outflow (V14).

A low line-of-sight optical depth is consistent with the high strength of the Lyα emission in J0816+22 and J1219+15. These two GPs have rest-frame EWs of $\sim$70 Å and 150 Å and Lyα escape fractions of 19% and 37%, with our assumed Lyα/Hα ratio of 8.7. Such high EWs are rare at low redshift (e.g., Finkelstein et al., 2009; Cowie et al., 2010), but fall in the range for LAEs at $z = 3$ (e.g., Ciardullo et al., 2012). J0303-08 has weaker Lyα emission with an EW of $\sim$ 10 Å and Lyα escape fraction of 2%, consistent with its higher optical depth. As expected, the Lyα emission of J1457+22 is the weakest, with an escape fraction of $< 1\%$.

4.2.2 Interstellar Absorption and Emission Lines

In stacked spectra of $z > 2$ LAEs, the strength of non-resonant emission lines such as Si II* and C II* appears to correlate with Lyα strength (e.g., Shapley et al., 2003; Berry et al., 2012). The origin of these lines is debated (e.g., Shapley et al., 2003; Erb et al., 2010; Berry et al., 2012), but here, we suggest that they probe the neutral ISM optical depth and geometry. In particular, for the GPs, the behavior of this emission supports the optical depths suggested by the Lyα profiles.

The non-resonant C II* λ1335.7 and Si II* λ1264.7 emission lines form when an electron in an excited state decays to the first fine-structure level above the ground

state. These lines share the same ^{2}D upper state as the C II λ1334.5 and Si II λ1260.4 resonant transitions, which generally appear in absorption in stacked LAE spectra (e.g., Shapley et al., 2003). Since these absorption lines arise in the neutral ISM, their optical depths are related to the LyC optical depth and the ISM metallicity (e.g., Heckman et al., 2001), and they offer an indirect diagnostic of the line-of-sight optical depth.

J0816+22 and J1219+15 show no detectable C II or Si II absorption, consistent with a low optical depth (Figure 4.2). As seen in spectra of high-redshift LAEs, both GPs show C II* and possible Si II* emission. In contrast, J0303-08 and J1457+22 have clear absorption in C II and Si II. The absorption in J0303-08 is broad and blueshifted, implying the presence of an outflow, while the narrow emission in J1457+22 originates from a relatively static absorbing column. The width of the absorption lines in J0303-08 is not due to a lower spectral resolution, since the C II and Si II absorption lines are four times wider than the observed Milky Way Si II absorption. J0303-08 also has the lowest metallicity of the four galaxies (Izotov et al., 2011), which implies that the relative absorption strengths in the GPs do not result solely from metallicity effects. J0303-08 and J1457+22 do differ in their C II* emission, however. While J0303-08 does not have clear C II* emission, J1457+22 exhibits the strongest C II* emission of the four GPs. We summarize the spectral line strengths of the GPs in Table 4.1. In the following discussion, we refer only to C II, but the results are equally applicable to Si II.

The Prochaska et al. (2011) models for Fe II transitions suggest an interpretation of the C II* emission that is entirely consistent with the geometries and optical depths implied by the GPs' Lyα emission and ISM absorption lines. In a cool gas outflow, each C II absorption should be balanced by C II or C II* emission into a random direction. We will therefore observe the wind component along our line of sight (LOS) in C II absorption, with weaker C II* emission. However, neutral gas outside

our LOS will also absorb far-UV photons from the central starburst and emit some of the resulting C II and C II* photons into our LOS. This emission from other parts of the wind should partially fill in the C II absorption and strengthen the C II* emission. *Therefore, the C II absorption and fluorescent C II* emission probe the outflow geometry and optical depth.*

The lack of C II absorption and the presence of C II* emission in J0816+22 and J1219+15 resemble the Prochaska et al. (2011) model for an unobscured UV emission source. In this case, neutral gas located *outside* the LOS absorbs UV radiation and emits C II* photons *into* our LOS. C II λ1334.5 emission should be weaker than C II* λ1335.7 due to its higher chance of absorption or its lower transition probability. As discussed previously, the Lyα profiles of J0816+22 and J1219+15 also suggest minimal absorption along the LOS, as expected for a mostly unobscured source, and possible scattered emission from neutral gas outside the LOS.

J0303-08 shows broad, blue-shifted C II absorption, but no C II* emission, similar to expectations for a collimated neutral outflow aligned with the LOS (Prochaska et al., 2011). Neutral, outflowing gas in front of the UV emission source will cause strong C II absorption. This gas will also produce C II* emission, but as the gas will emit isotropically, most of the emission will be directed away from our LOS. The weakness of the C II* emission in J0303-08 would then imply a lack of neutral material outside of the outflow. A high dust optical depth could also suppress the C II* emission (Prochaska et al., 2011), but the Balmer decrement implies a low extinction in this object (Jaskot & Oey, 2013). Alternatively, given the larger spatial extent of J0303-08, the C II*-emitting material may be located at large radii. The COS aperture might not encompass this emission, or the lower resolution at large radii may weaken its detectability. Imaging observations may determine whether neutral gas exists outside our LOS. Regardless, the C II absorption, deep, blue-shifted Lyα absorption trough, and weak Lyα emission in J0303-08 are consistent with an optically thick, neutral

outflow along the LOS.

While the strongest LAEs (J0816+22 and J1219+15) show C II* emission, the strongest non-resonant emission lines appear in the weakest LAE, J1457+22. This C II* detection is unexpected, given the trends with C II* and Lyα strength in stacked spectra, and demonstrates that stacked spectra may not match the real spectra of individual objects. A dense ISM component along the LOS will produce strong C II absorption and C II* emission near the systemic velocity (Prochaska et al., 2011), as seen in J1457+22. This scenario fits with our earlier conjecture that J1457+22 is highly inclined to our LOS. The high column density of the absorbing material results in a high optical depth to C II photons, suppressing their emission, while producing a large supply of C II* photons that escape. This deep column of neutral gas naturally explains the broad Lyα absorption, while the weak, superimposed Lyα emission may escape from scattering in a bipolar outflow.

4.3 Discussion

The geometry of the neutral ISM and its line-of-sight optical depth lead to a close connection between Lyα emission, C II and Si II absorption, and C II* and Si II* emission. Previous studies of stacked spectra of LAEs have found that higher Lyα EWs correlate with weaker interstellar absorption lines and stronger Si II* emission (e.g., Shapley et al., 2003; Berry et al., 2012). The weak absorption lines may indicate that stronger LAEs have lower LyC optical depths (Shapley et al., 2003). In our spectra of individual GPs, we likewise find that the two GPs with the strongest Lyα emission may be optically thin to the LyC. Since most of their neutral gas is not located along the LOS to the central starburst, we observe fluorescent C II* and Si II* emission with no accompanying C II and Si II absorption. This geometry may account for the similar Si II* emission observed in stacked LAE spectra. The two GPs with weaker Lyα emission do appear to have significant neutral gas in front of the starburst, but they differ

in their inclinations and geometry. As a result, while both galaxies have C II and Si II absorption, only the more inclined GP shows strong C II* and Si II* emission. J0303-08 either lacks neutral material to the side, has high extinction, or has neutral material only at large radii. A highly extended geometry would also reduce the Lyα emission in J0303-08. If strong C II absorption is ubiquitous in weak LAEs, but C II* emission depends on geometry, dust extinction, and inclination, C II absorption may appear in a stacked spectrum while the C II* emission is weakened. On the other hand, the wavelength of C II absorption depends on outflow velocity, whereas C II* emission should occur near the systemic velocity.

The Lyα emission and C II absorption in the GPs demonstrate that some galaxies with high [O III]/[O II] may be LCEs. Two of the four GPs have weak C II absorption, strong Lyα emission, and Lyα profiles that resemble Balmer emission from circumstellar ejecta. These properties are consistent with a low optical depth along the LOS. The presence of fluorescent C II* emission suggests that these GPs do have excited neutral gas outside the LOS. Therefore, LyC emission may escape anisotropically, and identifying optically thin galaxies will depend on viewing orientation (e.g., Nestor et al., 2011; Zastrow et al., 2011). J1457+22, which appears highly inclined and optically thick along the line of sight, may be optically thin in other directions; emission-line imaging may determine its transverse optical depth (e.g., Zastrow et al., 2011).

Lyα emission may be an effective diagnostic of LyC optical depth, as suggested by V14. A low LyC optical depth should facilitate Lyα escape, resulting in higher Lyα EWs and Lyα line profiles that are less affected by scattering. Five of the eight $z \sim 2-3$ LAEs studied by Hashimoto et al. (2013) have peak velocities within 200 $\mathrm{km\,s^{-1}}$ of the systemic velocity, similar to J0816+22 and J1219+15, and suggestive of a low column density. The strong Lyα emission and indications of a relatively low optical depth in two GPs suggest that these galaxies are low-redshift analogs of

high-redshift LAEs and LCEs.

Some high-redshift starbursts, particularly strong LAEs, may have low neutral column densities. As a result, these LAEs may show Lyα profiles similar to Balmer line emission from stellar sources, indicating a reduced optical depth. C II absorption and C II* emission can probe the orientation and optical depth of neutral outflows in LAEs and, along with Lyα profile shape, can be used to identify candidate LCEs.

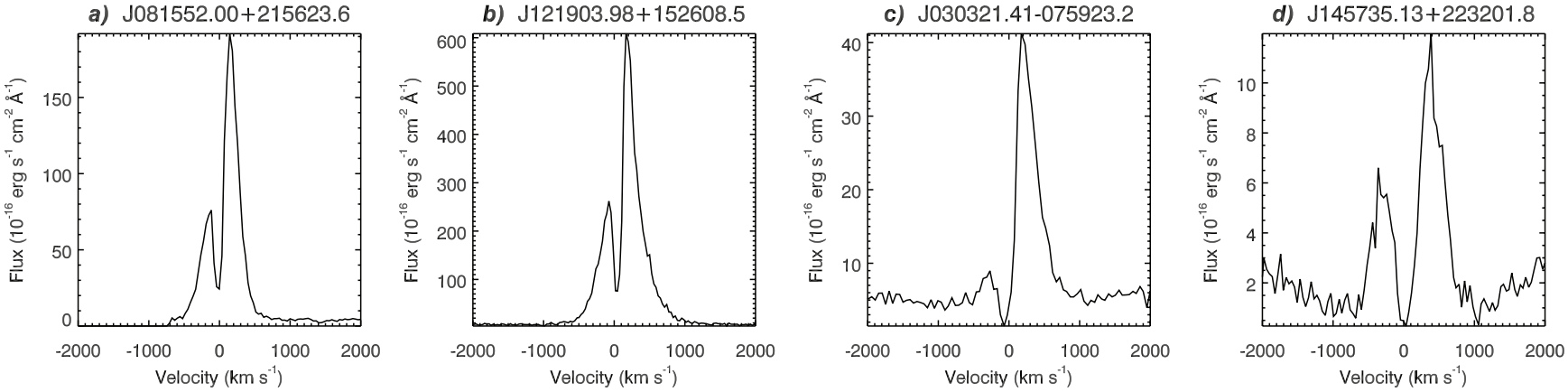

Figure 4.1: *HST* COS Lyα emission in the four GPs.

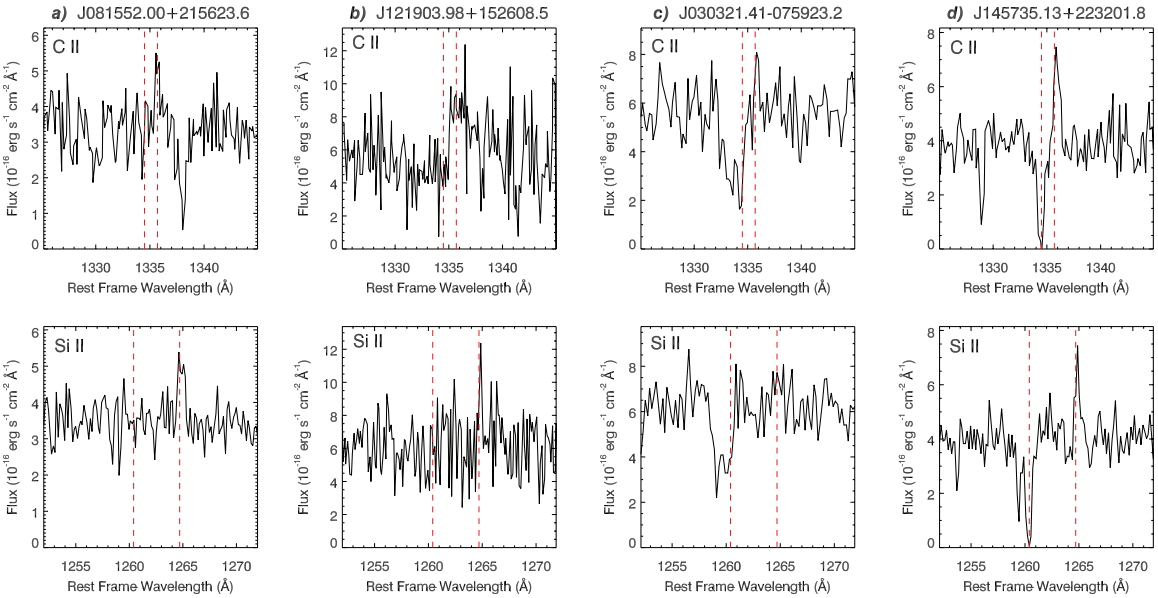

Figure 4.2: Top panels: C II λ1334.5 absorption and C II* λ1335.7 emission in the GPs. Bottom panels: Si II λ1260.4 absorption and Si II* λ1264.7 emission. Red dashed lines indicate the expected positions of these transitions from the SDSS redshifts.

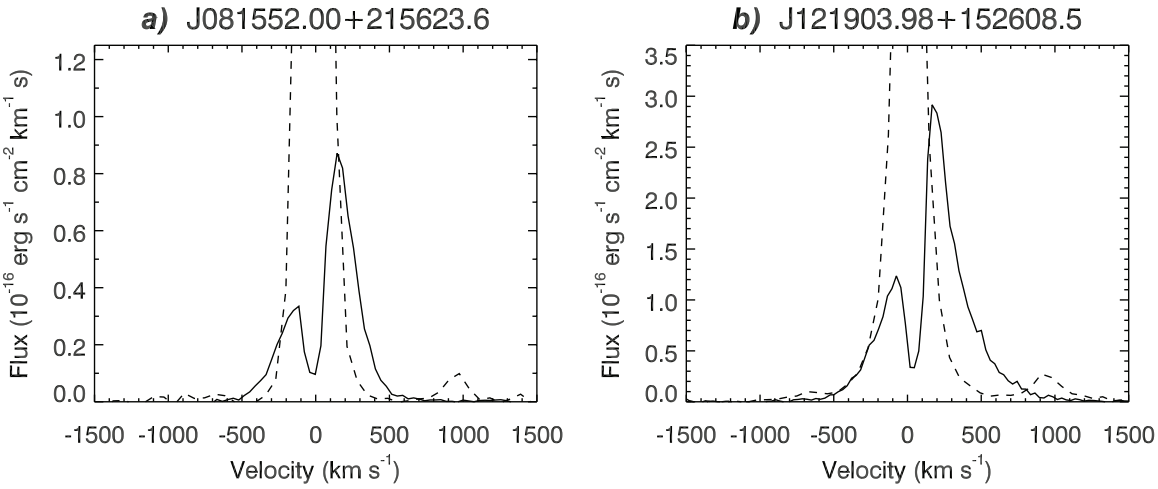

Figure 4.3: Solid lines show the Lyα emission for J0816+22 and J1219+15. Dashed lines show the Hα profiles from the SDSS spectra, scaled by a factor of 8.7 to approximate the intrinsic Lyα profiles. The [N II] lines appear as bumps near -700 and +1000 km s^{-1}.

Table 4.1: UV Spectral Lines in the GPs

SDSS ID	z	$\frac{[\mathrm{O\,III}]}{[\mathrm{O\,II}]}$ [a]	r_{50}^{b} (kpc)	Binning (Å pix^{-1})	Lyα EW (Å)	$\Delta v_{\mathrm{peak}}^{c}$ (km s^{-1})	C II EW[d] (Å)	C II* EW[d] (Å)	Si II EW[d] (Å)	Si II* EW[d] (Å)
J081552.00 +215623.6	0.1410	13.7	0.4	0.17	71 ± 11	260	...	0.2	...	0.5
J121903.98 +152608.5	0.1956	12.4	0.5	0.15	149 ± 30	270	...	1.4	...	0.3
J030321.41 -075923.2	0.1648	9.4	0.8	0.23	9 ± 3	440	-1.3	...	-1.0	...
J145735.13 -075923.2	0.1487	9.8	0.5	0.18	-6 ± 7	750	-0.9	0.7	-0.9	0.3

[a] [O III] $\lambda\lambda$5007,4959/[O II] λ3727 from Jaskot & Oey (2013).
[b] NUV half-light radius.
[c] Separation of the Lyα peaks.
[d] Based on Gaussian fits.

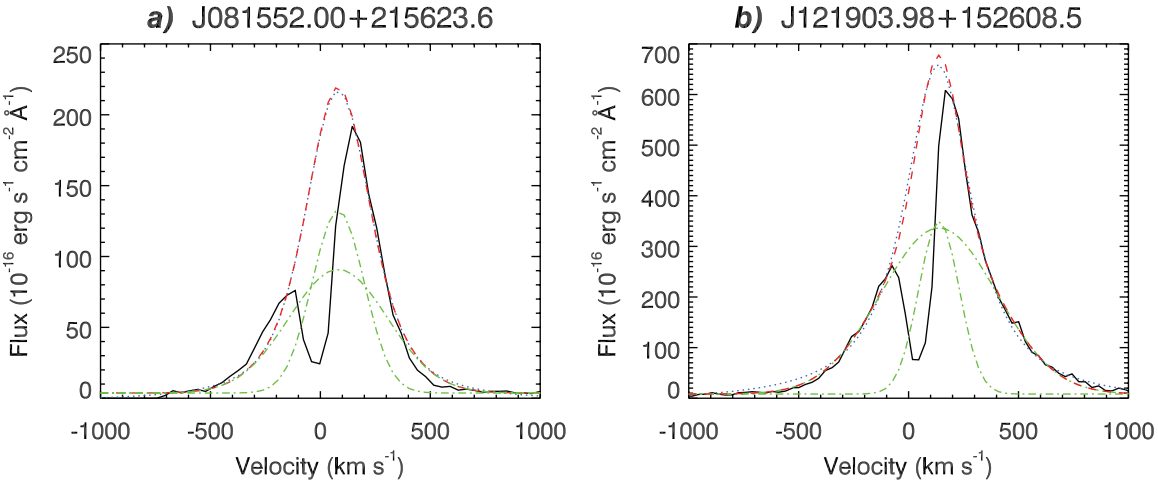

Figure 4.4: Solid lines show observed Lyα emission. Blue dotted lines indicate a Voigt fit, and red dashed lines indicate fits using two Gaussian components. The two Gaussians are shown separately with green dash-dotted lines.

CHAPTER V

Conclusion

This work reveals the interactions between atomic gas and extreme star formation in low-redshift starbursts. Using multiwavelength data ranging from the H I 21 cm line to UV Lyα emission, we investigate the H I gas content, geometry, and optical depth in two samples of starburst galaxies. Our analysis of the ALFALFA-Hα galaxies illustrates how low-redshift starbursts are triggered, the role of H I in fueling star formation, and the effects of feedback on the H I gas supply. With the rare Green Pea (GP) galaxies, some of the most extreme starbursts at low redshift, we investigate the origin of highly ionized gas and the propagation of LyC radiation through the neutral ISM. In particular, we propose that extreme emission-line galaxies like the GPs may have low optical depths to LyC radiation and suggest a new way of probing their neutral gas geometry and optical depth using UV spectra.

5.1 H I and Star Formation

The ALFALFA-Hα survey represents the first opportunity to compare the properties of starbursts and non-starbursts within a statistically uniform H I-selected sample. In Chapter 2, we analyze the H I gas fractions, H I depletion times, H I kinematics, and optical morphologies of eight starbursts within the 565 galaxies that make up the "fall-sky" ALFALFA-Hα sample. The ALFALFA-Hα galaxies confirm previous

observations that at a given stellar mass, more H I-rich galaxies typically have higher SFRs (Catinella et al., 2010; Huang et al., 2012). Since higher H I gas fractions may indicate the presence of recently accreted gas (e.g., Moran et al., 2012), this trend suggests that H I accretion actively fuels star formation in low-redshift galaxies. Nevertheless, the scatter in the $M_{\rm HI}$/SFR ratio at a constant stellar mass shows that additional factors affect the ability of galaxies to access fresh H I fuel and efficiently convert it to H_2. In particular, the starbursts all show high star formation efficiencies (i.e., short H I depletion times) compared to similar mass galaxies. We find that the starbursts' H I gas fractions are not unusually elevated for their stellar mass, despite their much higher SFRs. Therefore, a high efficiency of H I to H_2 conversion, rather than a large influx of gas, is generating their high levels of star formation. Dynamical disturbances are a likely cause of this enhanced efficiency, allowing the starbursts to transport H I gas inward and generate high gas column densities more easily than non-starbursts.

5.1.1 The Link Between H I and Dust

For the ALFALFA-Hα sample as a whole, we find that galaxies' sSFRs and H I gas fractions are only weakly correlated. This result contrasts with the strong observed correlation between galaxy color and H I gas fraction identified in previous studies (e.g., Kannappan, 2004; Zhang et al., 2009; Catinella et al., 2010; Huang et al., 2012) which suggests that galaxy sSFRs are linked to their H I content (e.g., Zhang et al., 2009; Huang et al., 2012). We likewise observe a tight correlation between H I gas fraction and $g-r$ color. For our sample of gas-rich galaxies, we demonstrate that dust extinction, rather than star formation, drives the tight trend between H I and color.

In essence, therefore, the H I and color relation is a manifestation of the well-known galaxy mass-metallicity relation. Bothwell et al. (2013) suggest that H I mass may

be a key third parameter in setting galaxy metallicities; in this model, $M_{\rm HI}/M_*$ and metallicity should anti-correlate. Since more metal-rich galaxies have higher dust content, we would therefore expect galaxies with high $M_{\rm HI}/M_*$ to have less dust extinction and bluer colors. Several processes could produce the proposed relation between galaxy stellar mass, H I content, and metallicity. Over their lifetimes, galaxies with higher stellar masses will have both consumed more H I gas and produced more metals via star formation. In addition, the higher potential wells of more massive galaxies should allow them to retain more metals (e.g., Davé et al., 2011a). At a given stellar mass, galaxies that have experienced a recent inflow of metal-poor gas from the IGM should have lower overall metallicities as well as higher H I content. Finally, we note that the elevated dust content of metal-rich galaxies will allow them to convert their H I gas to H_2 more efficiently by shielding molecular gas from UV radiation (e.g., Krumholz et al., 2009), thereby reducing their H I fractions further. This newly identified connection between H I content and dust extinction provides a natural explanation for the observed relation between H I gas fraction and color. H I inflows and outflows are fundamentally important to the evolution of galaxy metallicities, while galaxy metallicity may also influence the H I supply by promoting H_2 formation.

5.1.2 Galaxy Structure and H I Conversion

Another factor that may enhance the conversion of H I-to-H_2 is galaxy structure. We find that the H I depletion time in disk-dominated systems anti-correlates with stellar surface density. This relation may indicate that higher disk mid-plane pressure aids the formation of molecular clouds and increases the H_2/H I ratio, as proposed by Blitz & Rosolowsky (2006). However, alternate theories of H_2 formation based on self-shielding (e.g., Krumholz et al., 2009) may result in a similar stellar surface density scaling relation (Fu et al., 2010). Early supernova feedback in low-mass galaxies may lead to the delayed infall of H I gas, resulting in an increased H I content and longer

depletion time at the present day (Fu et al., 2010). By suppressing past star formation episodes, this efficient feedback should also lead to lower present-day stellar surface densities.

We only observe this correlation between H I depletion time and stellar surface density in disk galaxies, however. We show that high-mass, early-type galaxies from the COLD GASS sample (Saintonge et al., 2012) do not follow a similar relation. Within this early-type sample, we find no correlation between H I depletion time and morphology, which suggests that bulge strength is not affecting the current star formation efficiency in these galaxies. Instead, we suggest that the scatter in star formation efficiency results from differences in the spatial distribution and surface density of the H I gas.

5.1.3 Mergers and H I Conversion

For many of the starbursts, major mergers may induce their high SFRs and high H I to H_2 conversion efficiencies. During interactions, tidal torques propel gas toward the center of galaxies, thereby raising the gas column density (e.g., Barnes & Hernquist, 1991) and allowing galaxies to access their external H I supply. Furthermore, turbulent motions during the merger may compress gas clouds (Elmegreen et al., 1993), leading to a higher fraction of dense gas and a higher H_2/H I ratio (Powell et al., 2013). Starbursts also appear to form stars from H_2 more efficiently than non-starbursts (e.g., Daddi et al., 2010), perhaps due to the higher mean density and shorter free-fall time in their ISM (Krumholz et al., 2012). A merger scenario could therefore explain the moderate H I but high SFRs of the ALFALFA-Hα starbursts.

Evidence of morphological and kinematical disturbances support a merger origin for the starbursts. We find that the starbursts' optical morphologies are more asymmetric and their H I velocity profiles have wider wings than most of the non-starbursts. Merger simulations predict that the peak star formation activity should occur near

coalescence (e.g., Mihos & Hernquist, 1994; Cox et al., 2008; Lotz et al., 2010b), consistent with the starbursts' morphologies. The highest asymmetries, however, should appear shortly before coalescence. Interestingly, our two most asymmetric starbursts, which appear to be in this merger stage, also have higher-than-average H I gas fractions for their stellar mass. Their high H I gas fractions suggest that H I conversion may be an ongoing process during merger-driven star formation (e.g., Hibbard & van Gorkom, 1996).

Due to the unresolved nature of the Arecibo H I observations, we do not know the surface density of the H I gas in the ALFALFA-Hα starbursts. However, we find that they have above-average ratios of $M_{\rm HI}$ to the galaxy optical area. Therefore, either they lie closer to the maximum column density threshold for H I, which would aid H_2 formation, or their H I is significantly more extended than the optical disk. For instance, extended H I tidal tails may contain a large fraction of the H I gas in merging galaxies (e.g., Hibbard & van Gorkom, 1996).

The evidence for mergers among the lowest mass starbursts is less clear, in part due to their lower S/N optical images and H I spectra. Their H I velocity profiles do not noticeably differ from the profiles of low-mass non-starbursts, which may indicate a lack of kinematical disturbances. However, if the dwarf starbursts experience periodic bursts, any initial disturbance may no longer be evident (e.g., Verbeke et al., 2014). We observe an increased scatter in SFE at the low-mass end of our sample, which supports this scenario of episodic bursts in dwarf galaxies. Supernova feedback may have a stronger effect in the low potential wells of dwarf galaxies, leading to temporary quenching and a renewed burst of star formation as neutral gas falls back into the galaxy (e.g., Lee et al., 2007; Verbeke et al., 2014). Higher resolution imaging and H I spectral observations will be necessary to determine whether or not the dwarf starbursts are merging systems.

5.1.4 H I Cycles in Starbursts

We therefore propose the following picture for the cycling of H I and star formation throughout the starburst episode. In the higher mass starbursts, a gas-rich major merger triggers the star formation. As the two galaxies approach coalescence, the total stellar mass of the system increases. Since the two individual galaxies have H I gas fractions typical of lower mass galaxies, the combined system appears to have a higher H I mass than other galaxies of a similar stellar mass. Strong tidal torques drive H I gas outward to form tidal tails and inward to fuel star formation. The system also appears progressively more morphologically disturbed, and the increased gas flows and turbulence create kinematically disturbed H I profiles. As the H I gas flows inward, turbulence and gas compression efficiently convert H I to H_2 and increase the SFR. Although the gas flows bring H I inward, star formation is not necessarily restricted to the nuclear region, consistent with recent simulations (e.g., Powell et al., 2013). Turbulent, dense clumps may arise throughout the disk, and the precise merger configuration affects the spatial distribution of star formation. The influx of H I gas raises the ISM column density, and the star formation rate increases to the point where supernova-driven turbulence supports the enhanced weight of the ISM (Ostriker & Shetty, 2011). Peak star formation occurs near final coalescence, as the morphological disturbances are fading (e.g., Lotz et al., 2010b). However, at the time of the peak SFR, the turbulent motions driving star formation are still high (Powell et al., 2013) and the H I kinematics should still show higher velocities, as we observe. The H I content also begins to drop, due to the enhanced H_2 fraction and photoionization. Nevertheless, the starbursts still maintain a large H I supply, comparable to similar mass galaxies. Radiative feedback does not completely ionize the starbursts' H I reservoirs and may only ionize the H I gas near the starburst region (e.g., Hanish et al., 2010). In addition, H_2 photodissociation may compensate for the ionization of H I in the inner regions. Ultimately, gas consumption or feedback terminates the

starburst, and the merged galaxy exhibits a higher stellar mass, higher metallicity, and lower H I gas fraction than its progenitors.

Lower mass galaxies may experience recurrent starbursts. They may accumulate H I from the IGM until a dynamical disturbance initiates strong star formation. For instance, this initial trigger could be a merger with another galaxy, as in the case of the higher-mass starbursts, an interaction with a dark matter subhalo (Helmi et al., 2012), or a merger with a gas cloud. In the case of a gas cloud merger, the initial interaction should raise the H I content and disturb the H I kinematics, but may not trigger an immediate starburst (Verbeke et al., 2014). Subsequent infall from the gas cloud or enhanced turbulence may then induce a later starburst. The morphology of the star formation should vary depending on the nature of the interaction and the gas cloud trajectory. Regardless of the cause of the initial burst, supernova feedback rapidly quenches the initial starburst due to the low potential well of the galaxy (e.g., Dekel & Silk, 1986; Stinson et al., 2007; Hopkins et al., 2013). This feedback may increase the H I velocity dispersion, but these kinematic disturbances should lag the peak star formation (Verbeke et al., 2014). After the starburst dies down, the re-accretion of previously expelled gas may trigger a series of subsequent starbursts (e.g., Lee et al., 2007; Stinson et al., 2007). In addition, massive star clusters formed in a prior burst may generate torques that continue to drive H I gas inward (e.g., Elmegreen et al., 2012) to fuel future starbursts. These starburst cycles may gradually reduce a dwarf galaxy's H I reservoir but are unlikely to deplete it entirely, given the starbursts' high H I gas fractions. As with the more massive starbursts, photoionization may not affect the outer H I gas and may be balanced by photodissociation near the starburst. By quickly quenching star formation, the high feedback efficiencies in the dwarf starbursts may prevent rapid increases in metallicity or stellar mass. This scenario is consistent with the flat star formation histories and relatively inefficient star formation inferred for dwarf galaxies (e.g., Behroozi et al., 2013).

The dwarf starbursts' periodic star formation mode may be particularly relevant to high-redshift star formation. Milky Way progenitors at $z \approx 2$ may accrete gas from the IGM in discrete episodes that trigger enhanced star formation (Woods et al., 2014). However, as with the dwarf starbursts, feedback efficiently expels the gas and delays its consumption (e.g., Woods et al., 2014). As a result, these galaxies may have variable SFRs and may maintain an elevated H I content that fuels later star formation (e.g., Hopkins et al., 2013). However, unlike $z = 0$ galaxies, $z = 2$ galaxies experience higher accretion rates from the IGM (e.g., Kereš et al., 2005). As a result, high-redshift galaxies may have higher average SFRs and larger gas reservoirs than we observe for the ALFALFA-Hα sample. Feedback and variable SFRs in low-mass galaxies also have important implications for the reionization of the IGM. Wyithe & Loeb (2013) argue that by suppressing star formation, efficient feedback may reduce the contribution of the lowest mass galaxies to reionization. Constraining the starburst duty cycle in dwarf galaxies is therefore important to understand both galaxy star formation histories and reionization.

5.2 The GPs: New LCE Candidates

The LyC radiation produced in extreme starbursts may ionize the H I gas near the star-forming clusters, even if it does not reach the outer H I reservoir. Depending on the column density and spatial distribution of the H I gas near the starburst, this ionizing radiation may escape into the IGM. In Chapters 3 and 4, we investigate the LyC optical depths of some of the most extreme low-redshift starbursts, the GPs (Cardamone et al., 2009). The GPs have unusually high [O III]/[O II] ratios, which imply a high ionization parameter or a low LyC optical depth (e.g., Giammanco et al., 2005; Pellegrini et al., 2012). The Hα EWs of the GPs are significantly higher than the EWs of the ALFALFA-Hα starbursts, which implies that the starbursts in the GPs are younger and more powerful. Radiative feedback may therefore have

stronger effects on the H I gas in the GPs.

5.2.1 Ionizing Sources and LyC Optical Depths

We detect He II λ4686 emission in the SDSS spectra of the GPs with the highest [O III]/[O II] ratios, which implies that hard ionizing sources must be present in these extreme starbursts. Our analysis of the possible ionizing sources in Chapter 3 indicates that hot stellar sources or shocks generate the observed He II. The observed spectral line ratios and inferred ages of the GPs eliminate AGN and HMXBs as the main sources of ionization. CLOUDY models with a WR-dominated starburst or unusually hot O stars can reproduce the observed [O III]/[O II] ratios even in optically thick gas. However, we observe no WR features in individual or stacked spectra of the GPs. Although chemically homogeneous, rapidly rotating O stars could potentially produce the necessary hard ionizing photons (e.g., Maeder, 1987; Yoon et al., 2006; Brott et al., 2011a), such stars may not exist and their spectral properties are unknown. This possibility highlights the need for more study of the effects of rotation in low-metallicity stellar populations. While we find no convincing evidence of large populations of WR stars or rapidly rotating O stars in the GPs, several lines of evidence suggest that shocks are present; high-velocity Balmer line emission, the ages of the GPs, and the detection of [O I] emission all support the shock-emission scenario. We therefore conclude that shocks may be the most likely source of the He II emission.

The presence of shock emission would both imply a low optical depth and suggest a possible cause of the LyC escape in the GPs. In addition to He II, shocks should produce [O II] emission, and the observed [O III]/[O II] ratios would therefore underestimate the true [O III]/[O II] ratios of the photoionized gas in the GPs. Such high [O III]/[O II] ratios are a clear indication of optically thin emission. By altering the observed line ratio diagnostics, shock emission may dramatically change the inferred

ionization parameters and optical depths in starburst galaxies. As illustrated by the ALFALFA-Hα starbursts, gas flows caused by galaxy interactions or supernova feedback are important processes in starburst galaxies; these gas motions could induce shocks in the GPs. In fact, observations of merging systems suggest that shocks may contribute significantly to the nebular line emission (e.g., Rich et al., 2014; Krabbe et al., 2014). Future analyses of nebular line emission in starbursts should therefore consider the possible effects of shock emission.

In the GPs, supernova feedback may both account for the observed shock emission and aid LyC escape by carving low-density passages in the ISM. The GPs' ages of 3-5 Myr may optimize LyC escape (e.g., Zastrow et al., 2013b), as the first SNe disrupt the neutral ISM, while massive stars are still available to provide LyC photons. We suggest that the GPs may therefore be rare, low-redshift LyC emitters (LCEs) and that starburst age may control the LyC escape fraction.

5.2.2 Insights from UV Spectral Lines

In Chapter 4, using *HST* COS spectra of four extreme GPs, we demonstrate that some GPs are indeed likely LCEs. Furthermore, the neutral ISM of these GPs appear inhomogeneous, possibly due to the restructuring of the ISM by SNe. We develop a simple, physical picture of the neutral gas geometry and optical depth in the GPs that simultaneously relates their Lyα emission, C II and Si II absorption lines, and C II* and Si II* emission lines. Our new interpretation elucidates the origin of the previously enigmatic C II* and Si II* emission in starburst galaxies.

Differences in feedback efficiency and inclination probably explain the variations in the inferred line-of-sight optical depths of the four GPs in our UV sample. The two most promising LCE candidates, J0816+22 and J1219+15, display strong, narrow Lyα emission, which suggests that the Lyα optical depth is lower than in many LAEs. Furthermore, the similarities of these GPs' Lyα profiles to the Balmer line

emission profiles from stellar ejecta suggest that the Lyα emission originates from a neutral gas shell with a reduced optical depth. These same GPs show no detectable C II or Si II absorption, implying a low line-of-sight optical depth, although they do exhibit fluorescent C II* and Si II* emission. Based on the neutral outflow models of Prochaska et al. (2011), we argue that neutral gas outside the line of sight is absorbing UV photons and emitting C II* and Si II* photons into the line of sight. Supernova feedback may have reduced the line-of-sight H I column density, permitting LyC escape, while denser neutral material still survives outside the line of sight.

Supernova feedback does not appear to have succeeded in clearing away the neutral gas in the GP J0303-08, however. The Lyα profile shape and broad, blue-shifted C II absorption in J0303-08 suggest an optically thick neutral outflow. J0303-08 has the lowest [O III]/[O II] ratio of the six extreme GPs discussed in Chapter 3, consistent with its higher inferred optical depth. The detected outflow supports the supernova shock scenario, but the strong absorption suggests a high optical depth. Even after accounting for shock emission, therefore, the [O III]/[O II] ratios of J0303-08 should not fall in the optically thin regime, which limits the possible shock models for this galaxy. J0303-08 has a slightly higher stellar mass (Izotov et al., 2011), a lower Hα EW, and a more extended morphology than the other GPs. The feedback in J0303-08 may therefore be weaker than in the other GPs and may not have been sufficient to expel significant H I.

A high inclination to the line of sight may cause the large optical depth of the final GP, J1457+22. Its weak, double-peaked Lyα profile has a large velocity separation and lies within a wide absorption trough, indicative of a high optical depth and consistent with simulations of Lyα radiative transfer in inclined galaxies (Verhamme et al., 2012). Deep C II absorption and strong C II* emission likewise suggest a large neutral ISM component along the line of sight. If J1457+22 is inclined, it may still have a low optical depth in the perpendicular direction. Upcoming emission-line

imaging observations should reveal the transverse optical depth of J1457+22.

With these UV spectra of four GPs, we explain the previously puzzling correlation observed between Lyα emission, C II and Si II absorption, and C II* and Si II* emission in high-redshift LAEs. We show that these lines provide a coherent picture of the optical depth and geometry in starbursts, and we propose that strong, narrow Lyα emission with C II* and Si II* emission and no accompanying absorption is a hallmark of low optical depth starbursts. These diagnostics are applicable to the rest-frame UV spectra of high-redshift LAEs and may reveal the neutral gas configuration and optical depth of these distant galaxies.

5.3 Implications for LyC Escape

The neutral gas properties of the ALFALFA-Hα and GP starbursts reveal the possible factors that may enhance LyC escape in low-redshift starbursts. The high H I gas fractions of the ALFALFA-Hα galaxies suggest that radiative feedback in these starbursts is unable to ionize significant fractions of the H I. However, SNe in the lowest mass ALFALFA-Hα galaxies may temporarily expel their H I supply, leading to successive bursts of star formation as gas is expelled and re-accreted. In this cyclical model, LyC radiation may escape along the channels evacuated during a previous burst or during the short time period following the ejection of the H I. Simulations also indicate that efficient supernova feedback in low-mass halos and the reshaping of the ISM from previous SNe may lead to high LyC escape fractions (e.g., Razoumov & Sommer-Larsen, 2010; Wise & Cen, 2009), although the efficient quenching of star formation may also reduce the overall contribution of low-mass galaxies to reionization (Wyithe & Loeb, 2013). The confirmed LCE Haro 11 may be an example of LyC escape due to the effects of previous star formation. The starburst phase in Haro 11 may have lasted for 40 Myr (Adamo et al., 2010), and the suspected LyC-leaking region may have had both past and ongoing star formation

(Adamo et al., 2010; Leitet et al., 2013). The low neutral gas covering fraction of this region (Leitet et al., 2013) may be the product of a previous episode of stellar feedback.

Unlike the ALFALFA-Hα starbursts, the more extreme, compact GPs may be able to ionize large fractions of their surrounding H I gas. The GPs' Lyα emission profiles, weak C II absorption, and high [O III]/[O II] ratios all suggest a low H I column density. The higher inferred column densities of two GPs illustrate the importance of inclination angle, burst strength, and the spatial distribution of star formation in LyC escape. Again, starburst age and SNe may be crucial in permitting LyC escape. The young burst ages of the GPs, < 5 Myr, and their high [O III]/[O II] ratios may be similar to the second known low-redshift LCE, Tol 1247-232 (Leitet et al., 2013). As we suggested in Chapter 3, the first SNe in the GPs may be clearing away gas from the central starburst. Only a narrow age range may be conducive to LyC escape. Early starburst stages may have the highest H I gas fractions (see Chapter 2), which may fully absorb the LyC radiation. As the starburst ages, stellar winds and SNe begin to uncover the starburst, but at the same time, the starburst ages and produces fewer LyC photons. Young, powerful starbursts at the time of their first SNe may therefore be LCE candidates.

The H I gas fractions of most starbursts may remain approximately constant throughout the burst, and only the most extreme starbursts at low redshift may significantly disrupt their H I gas. Such intense starbursts may be more common at high redshift and may provide the necessary photons for cosmic reionization. LyC may preferentially escape along lower column density lines of sight cleared out by SNe, and the relative spatial locations of young stellar clusters and neutral gas should affect the LyC escape fraction (e.g., Gnedin et al., 2008; Pellegrini et al., 2012). Starburst age may also be a critical parameter in setting LyC escape fractions. The LyC escape fractions of both low- and high-redshift starbursts may fluctuate with starburst age,

and brief phases of elevated emission may dominate the LyC flux into the IGM.

5.4 Future Work

Future observations will constrain the H I properties of a larger sample of starbursts, reveal how the spatial distribution of H I evolves during a starburst, confirm the nature of the GPs, and extend these studies to higher redshift. The upcoming analysis of the "spring-sky" ALFALFA-Hα galaxies will almost triple the sample size of this uniform survey. The larger sample will provide more robust statistics on the H I properties of starbursts and may include more extreme, rarer, or higher-mass starbursts. These additional galaxies may reveal additional starburst triggering mechanisms and will test whether H I content changes as a function of merger stage. Spatially resolved H I observations may uncover the triggering mechanism of low-redshift starbursts by highlighting previously hidden morphological disturbances. Resolved observations will also show how feedback affects the H I over the course of a starburst by revealing possible outflows, inflows, and depleted regions. H I mapping of the lowest redshift GPs may provide evidence of the low column density channels that promote LyC escape. The mapping of low optical depth regions and their relation to observed stellar clusters will illustrate the role of past or present supernova feedback in promoting LyC escape.

We are planning to continue our study of the GPs to establish their LyC escape fractions and starburst properties. With deeper spectral observations from the Magellan telescopes, we will detect faint WR features or shock lines to confirm the ionizing sources in the GPs and the origin of the He II emission. While our *HST* COS observations probed the line-of-sight optical depth of the GPs, with upcoming ACS emission-line imaging observations, we will map the ionization structure of the GPs to determine where LyC radiation is likely to escape. More detailed modeling of the Lyα profiles will also provide quantitative estimates of the line-of-sight

H I column density, and future UV observations may definitively determine the GPs' optical depths through the direct detection of LyC. In addition, with larger samples of emission-line galaxies, we will examine how ionization source and burst age affect the [O III]/[O II] ratios and optical depths of starbursts. A larger sample will determine whether GP-like galaxies are a heterogeneous class of galaxies and whether their properties evolve with redshift.

The next generation of telescopes will extend our knowledge of H I cycles in starbursts to earlier cosmic times. The planned Square Kilometer Array will detect H I 21 cm emission in star-forming galaxies out to $z = 2$. These observations will demonstrate whether episodic bursts and relatively constant H I gas fractions characterize higher redshift starbursts. Future telescopes will also apply our newfound relation between Lyα, low-ionization transitions, and neutral gas geometry to higher redshift galaxies. Optical or near-infrared observations with 30 m telescopes may detect faint C II and Si II lines in individual LAEs at $z > 2$. These observations will test the correlation between Lyα and low-ionization lines and will establish the neutral gas configuration in LAEs. The upcoming *James Webb Space Telescope* will probe the UV emission of even higher redshift galaxies and will reveal the cosmic evolution of Lyα profiles, optical depth, and neutral gas geometry in starbursts. These new observations will place our study of low-redshift starbursts in a cosmic context and reveal the evolution of starburst H I cycles and optical depths over the universe's history.

BIBLIOGRAPHY

BIBLIOGRAPHY

Abazajian, K., et al. 2004, *AJ*, 128, 502

Abazajian, K. N., et al. 2009, *ApJS*, 182, 543

Adamo, A., Östlin, G., Zackrisson, E., Hayes, M., Cumming, R. J., & Micheva, G. 2010, *MNRAS*, 407, 870

Ahn, C. P., et al. 2012, *ApJS*, 203, 21

Ahn, S.-H., Lee, H.-W., & Lee, H. M. 2000, Journal of Korean Astronomical Society, 33, 29

Alavi, A., et al. 2014, *ApJ*, 780, 143

Allen, M. G., Groves, B. A., Dopita, M. A., Sutherland, R. S., & Kewley, L. J. 2008, *ApJS*, 178, 20

Allen, R. J., Atherton, P. D., & Tilanus, R. P. J. 1986, *Nature*, 319, 296

Allende Prieto, C., Lambert, D. L., & Asplund, M. 2001, *ApJ*, 556, L63

Amorín, R., Pérez-Montero, E., Vílchez, J. M., & Papaderos, P. 2012a, *ApJ*, 749, 185

Amorín, R., Vílchez, J. M., Hägele, G. F., Firpo, V., Pérez-Montero, E., & Papaderos, P. 2012b, *ApJ*, 754, L22

Amorín, R. O., Pérez-Montero, E., & Vílchez, J. M. 2010, *ApJ*, 715, L128

Atek, H., et al. 2014, *ApJ*, 789, 96

Baldwin, J. A., Phillips, M. M., & Terlevich, R. 1981, *PASP*, 93, 5

Balick, B. 1989, *AJ*, 97, 476

Barnes, J. E., & Hernquist, L. E. 1991, *ApJ*, 370, L65

Bauermeister, A., et al. 2013, *ApJ*, 768, 132

Beck, S. C., Turner, J. L., Langland-Shula, L. E., Meier, D. S., Crosthwaite, L. P., & Gorjian, V. 2002, *AJ*, 124, 2516

Behrens, C., Dijkstra, M., & Niemeyer, J. C. 2014, *A&A*, 563, A77

Behroozi, P. S., Wechsler, R. H., & Conroy, C. 2013, *ApJ*, 770, 57

Bell, E. F., & de Jong, R. S. 2001, *ApJ*, 550, 212

Bell, E. F., McIntosh, D. H., Katz, N., & Weinberg, M. D. 2003, *ApJS*, 149, 289

Berry, M., et al. 2012, *ApJ*, 749, 4

Bianchi, S. 2007, *A&A*, 471, 765

Bigiel, F., Leroy, A., Walter, F., Brinks, E., de Blok, W. J. G., Madore, B., & Thornley, M. D. 2008, *AJ*, 136, 2846

Blitz, L., & Rosolowsky, E. 2004, *ApJ*, 612, L29

—. 2006, *ApJ*, 650, 933

Bolatto, A. D., et al. 2011, *ApJ*, 741, 12

Bolton, J. S., Haehnelt, M. G., Viel, M., & Springel, V. 2005, *MNRAS*, 357, 1178

Boone, F., Schaerer, D., Pelló, R., Combes, F., & Egami, E. 2007, *A&A*, 475, 513

Bothwell, M. S., Kennicutt, R. C., & Lee, J. C. 2009, *MNRAS*, 400, 154

Bothwell, M. S., Maiolino, R., Kennicutt, R., Cresci, G., Mannucci, F., Marconi, A., & Cicone, C. 2013, *MNRAS*, 433, 1425

Bouché, N., et al. 2007, *ApJ*, 671, 303

Bournaud, F., Powell, L. C., Chapon, D., & Teyssier, R. 2011, in IAU Symposium, Vol. 271, IAU Symposium, ed. N. H. Brummell, A. S. Brun, M. S. Miesch, & Y. Ponty, 160–169

Bouwens, R. J., et al. 2010, *ApJ*, 709, L133

—. 2012, *ApJ*, 752, L5

Bravo-Alfaro, H., Brinks, E., Baker, A. J., Walter, F., & Kunth, D. 2004, *AJ*, 127, 264

Bressan, A., Fagotto, F., Bertelli, G., & Chiosi, C. 1993, *A&AS*, 100, 647

Brinchmann, J., Charlot, S., White, S. D. M., Tremonti, C., Kauffmann, G., Heckman, T., & Brinkmann, J. 2004, *MNRAS*, 351, 1151

Brinchmann, J., Pettini, M., & Charlot, S. 2008, *MNRAS*, 385, 769

Brocklehurst, M. 1971, *MNRAS*, 153, 471

Broeils, A. H., & Rhee, M.-H. 1997, *A&A*, 324, 877

Brott, I., et al. 2011a, *A&A*, 530, A115

—. 2011b, *A&A*, 530, A116

Bruzual, G., & Charlot, S. 2003, *MNRAS*, 344, 1000

Burmeister, M., & Leedjärv, L. 2009, *A&A*, 504, 171

Calzetti, D. 1997, *AJ*, 113, 162

Calzetti, D., Armus, L., Bohlin, R. C., Kinney, A. L., Koornneef, J., & Storchi-Bergmann, T. 2000, *ApJ*, 533, 682

Cannon, J. M., et al. 2011, *ApJ*, 735, 35

Cantalupo, S. 2010, *MNRAS*, 403, L16

Cardamone, C., et al. 2009, *MNRAS*, 399, 1191

Cardelli, J. A., Clayton, G. C., & Mathis, J. S. 1989, *ApJ*, 345, 245

Castor, J., McCray, R., & Weaver, R. 1975, *ApJ*, 200, L107

Catinella, B., et al. 2012, *A&A*, 544, A65

—. 2010, *MNRAS*, 403, 683

Chabrier, G. 2003, *PASP*, 115, 763

Chakraborti, S., Yadav, N., Cardamone, C., & Ray, A. 2012, *ApJ*, 746, L6

Chandar, R., Leitherer, C., Tremonti, C., & Calzetti, D. 2003, *ApJ*, 586, 939

Charlot, S., & Fall, S. M. 2000, *ApJ*, 539, 718

Chevalier, R. A., & Clegg, A. W. 1985, *Nature*, 317, 44

Chyży, K. T., & Beck, R. 2004, *A&A*, 417, 541

Ciardullo, R., et al. 2012, *ApJ*, 744, 110

Clarke, C., & Oey, M. S. 2002, *MNRAS*, 337, 1299

Combes, F., García-Burillo, S., Braine, J., Schinnerer, E., Walter, F., & Colina, L. 2013, *A&A*, 550, A41

Combes, F., Prugniel, P., Rampazzo, R., & Sulentic, J. W. 1994, *A&A*, 281, 725

Conselice, C. J. 2003, *ApJS*, 147, 1

Conselice, C. J., Bershady, M. A., & Gallagher, III, J. S. 2000a, *A&A*, 354, L21

Conselice, C. J., Bershady, M. A., & Jangren, A. 2000b, *ApJ*, 529, 886

Conti, P. S., Garmany, C. D., & Massey, P. 1989, *ApJ*, 341, 113

Cowie, L. L., Barger, A. J., & Hu, E. M. 2010, *ApJ*, 711, 928

Cowie, L. L., Hu, E. M., & Songaila, A. 1995, *AJ*, 110, 1576

Cowie, L. L., & Songaila, A. 1986, *ARA&A*, 24, 499

Cox, T. J., Jonsson, P., Somerville, R. S., Primack, J. R., & Dekel, A. 2008, *MNRAS*, 384, 386

Crowther, P. A., & Hadfield, L. J. 2006, *A&A*, 449, 711

Cui, J., Xia, X.-Y., Deng, Z.-G., Mao, S., & Zou, Z.-L. 2001, *AJ*, 122, 63

Cutri, R. M., & et al. 2012, VizieR Online Data Catalog, 2311, 0

Cutri, R. M., et al. 2012, Explanatory Supplement to the WISE All-Sky Data Release Products, Tech. rep.

Daddi, E., Dannerbauer, H., Elbaz, D., Dickinson, M., Morrison, G., Stern, D., & Ravindranath, S. 2008, *ApJ*, 673, L21

Daddi, E., et al. 2010, *ApJ*, 714, L118

Dalcanton, J. J. 2007, *ApJ*, 658, 941

Davé, R., Finlator, K., & Oppenheimer, B. D. 2011a, *MNRAS*, 416, 1354

Davé, R., Oppenheimer, B. D., & Finlator, K. 2011b, *MNRAS*, 415, 11

de Barros, S., Schaerer, D., & Stark, D. P. 2014, *A&A*, 563, A81

de Blok, W. J. G., et al. 2014, ArXiv e-prints

De Geyter, G., Baes, M., Camps, P., Fritz, J., De Looze, I., Hughes, T. M., Viaene, S., & Gentile, G. 2014, *MNRAS*, 441, 869

de Grijs, R., O'Connell, R. W., Becker, G. D., Chevalier, R. A., & Gallagher, III, J. S. 2000, *AJ*, 119, 681

Dekel, A., & Silk, J. 1986, *ApJ*, 303, 39

Della Ceca, R., Griffiths, R. E., Heckman, T. M., Lehnert, M. D., & Weaver, K. A. 1999, *ApJ*, 514, 772

Di Matteo, P., Combes, F., Melchior, A.-L., & Semelin, B. 2007, *A&A*, 468, 61

Dickinson, M., Papovich, C., Ferguson, H. C., & Budavári, T. 2003, *ApJ*, 587, 25

Ellison, S. L., Mendel, J. T., Patton, D. R., & Scudder, J. M. 2013, *MNRAS*, 435, 3627

Elmegreen, B. G., Kaufman, M., & Thomasson, M. 1993, *ApJ*, 412, 90

Elmegreen, B. G., & Lada, C. J. 1977, *ApJ*, 214, 725

Elmegreen, B. G., Zhang, H.-X., & Hunter, D. A. 2012, *ApJ*, 747, 105

Elmegreen, D. M., Elmegreen, B. G., Rubin, D. S., & Schaffer, M. A. 2005, *ApJ*, 631, 85

Erb, D. K., Pettini, M., Shapley, A. E., Steidel, C. C., Law, D. R., & Reddy, N. A. 2010, *ApJ*, 719, 1168

Ewen, H. I., & Purcell, E. M. 1951, *Nature*, 168, 356

Fagotto, F., Bressan, A., Bertelli, G., & Chiosi, C. 1994, *A&AS*, 105, 29

Ferland, G. J., Korista, K. T., Verner, D. A., Ferguson, J. W., Kingdon, J. B., & Verner, E. M. 1998, *PASP*, 110, 761

Fernandes, I. F., de Carvalho, R., Contini, T., & Gal, R. R. 2004, *MNRAS*, 355, 728

Fernandez, E. R., & Shull, J. M. 2011, *ApJ*, 731, 20

Ferrara, A., & Loeb, A. 2013, *MNRAS*, 431, 2826

Finkelstein, S. L., Cohen, S. H., Malhotra, S., & Rhoads, J. E. 2009, *ApJ*, 700, 276

Finkelstein, S. L., et al. 2012, *ApJ*, 756, 164

Fontanot, F., Cristiani, S., & Vanzella, E. 2012, *MNRAS*, 425, 1413

Fragos, T., et al. 2013, *ApJ*, 764, 41

Fu, J., Guo, Q., Kauffmann, G., & Krumholz, M. R. 2010, *MNRAS*, 409, 515

Fumagalli, M., et al. 2012, *ApJ*, 757, L22

Gallagher, J. S., Knapp, G. R., & Faber, S. M. 1981, *AJ*, 86, 1781

Gallazzi, A., Brinchmann, J., Charlot, S., & White, S. D. M. 2008, *MNRAS*, 383, 1439

Gavazzi, G., Pierini, D., & Boselli, A. 1996, *A&A*, 312, 397

Gawiser, E., et al. 2007, *ApJ*, 671, 278

Gerola, H., Seiden, P. E., & Schulman, L. S. 1980, *ApJ*, 242, 517

Ghosh, P., & White, N. E. 2001, *ApJ*, 559, L97

Giammanco, C., Beckman, J. E., & Cedrés, B. 2005, *A&A*, 438, 599

Giavalisco, M., Koratkar, A., & Calzetti, D. 1996, *ApJ*, 466, 831

Giovanelli, R., et al. 2005a, *AJ*, 130, 2613

—. 2005b, *AJ*, 130, 2598

Gladders, M. D., Oemler, A., Dressler, A., Poggianti, B., Vulcani, B., & Abramson, L. 2013, *ApJ*, 770, 64

Gnedin, N. Y., Kravtsov, A. V., & Chen, H.-W. 2008, *ApJ*, 672, 765

González Delgado, R. M., Leitherer, C., & Heckman, T. M. 1999, *ApJS*, 125, 489

Gordon, D., & Gottesman, S. T. 1981, *AJ*, 86, 161

Grimm, H.-J., Gilfanov, M., & Sunyaev, R. 2003, *MNRAS*, 339, 793

Guseva, N. G., Izotov, Y. I., & Thuan, T. X. 2000, *ApJ*, 531, 776

Hagen, A., et al. 2014, *ApJ*, 786, 59

Haiman, Z., Rees, M. J., & Loeb, A. 1997, *ApJ*, 476, 458

Hanish, D. J., Oey, M. S., Rigby, J. R., de Mello, D. F., & Lee, J. C. 2010, *ApJ*, 725, 2029

Hashimoto, T., Ouchi, M., Shimasaku, K., Ono, Y., Nakajima, K., Rauch, M., Lee, J., & Okamura, S. 2013, *ApJ*, 765, 70

Hawley, S. A. 2012, *PASP*, 124, 21

Hayes, M., et al. 2013, *ApJ*, 765, L27

Hayes, M., Schaerer, D., Östlin, G., Mas-Hesse, J. M., Atek, H., & Kunth, D. 2011, *ApJ*, 730, 8

Haynes, M. P., et al. 2011, *AJ*, 142, 170

Heckman, T. M., Armus, L., & Miley, G. K. 1990, *ApJS*, 74, 833

Heckman, T. M., et al. 2011, *ApJ*, 730, 5

—. 2005, *ApJ*, 619, L35

Heckman, T. M., Sembach, K. R., Meurer, G. R., Leitherer, C., Calzetti, D., & Martin, C. L. 2001, *ApJ*, 558, 56

Helmi, A., Sales, L. V., Starkenburg, E., Starkenburg, T. K., Vera-Ciro, C. A., De Lucia, G., & Li, Y.-S. 2012, *ApJ*, 758, L5

Hibbard, J. E., & van Gorkom, J. H. 1996, *AJ*, 111, 655

Hillier, D. J., & Miller, D. L. 1998, *ApJ*, 496, 407

Hopkins, A. M., & Beacom, J. F. 2006, *ApJ*, 651, 142

Hopkins, P. F., Keres, D., Onorbe, J., Faucher-Giguere, C.-A., Quataert, E., Murray, N., & Bullock, J. S. 2013, ArXiv e-prints

Huang, S., Haynes, M. P., Giovanelli, R., & Brinchmann, J. 2012, *ApJ*, 756, 113

Huchtmeier, W. K., Petrosian, A., Gopal-Krishna, & Kunth, D. 2007, *A&A*, 462, 919

Israel, F. P. 2005, *A&A*, 438, 855

Ivison, R. J., Bode, M. F., & Meaburn, J. 1994, *A&AS*, 103, 201

Iwata, I., et al. 2009, *ApJ*, 692, 1287

Izotov, Y. I., Guseva, N. G., & Thuan, T. X. 2011, *ApJ*, 728, 161

Izotov, Y. I., Schaerer, D., Blecha, A., Royer, F., Guseva, N. G., & North, P. 2006, *A&A*, 459, 71

Jarrett, T. H., et al. 2013, *AJ*, 145, 6

Jaskot, A. E., & Oey, M. S. 2013, *ApJ*, 766, 91

—. 2014, *ApJ*, 791, L19

Joy, M., & Lester, D. F. 1988, *ApJ*, 331, 145

Kaaret, P., Schmitt, J., & Gorski, M. 2011, *ApJ*, 741, 10

Kaaret, P., Ward, M. J., & Zezas, A. 2004, *MNRAS*, 351, L83

Kannappan, S. J. 2004, *ApJ*, 611, L89

Kannappan, S. J., et al. 2013, *ApJ*, 777, 42

Karim, A., et al. 2011, *ApJ*, 730, 61

Kennicutt, R. C., & Evans, N. J. 2012, *ARA&A*, 50, 531

Kennicutt, Jr., R. C. 1989, *ApJ*, 344, 685

—. 1998a, *ARA&A*, 36, 189

—. 1998b, *ApJ*, 498, 541

Kereš, D., Katz, N., Weinberg, D. H., & Davé, R. 2005, *MNRAS*, 363, 2

Kewley, L. J., & Dopita, M. A. 2002, *ApJS*, 142, 35

Kewley, L. J., Dopita, M. A., Sutherland, R. S., Heisler, C. A., & Trevena, J. 2001, *ApJ*, 556, 121

Klein, U., Wielebinski, R., & Morsi, H. W. 1988, *A&A*, 190, 41

Kobulnicky, H. A., Dickey, J. M., Sargent, A. I., Hogg, D. E., & Conti, P. S. 1995, *AJ*, 110, 116

Kornei, K. A., Shapley, A. E., Erb, D. K., Steidel, C. C., Reddy, N. A., Pettini, M., & Bogosavljević, M. 2010, *ApJ*, 711, 693

Krabbe, A. C., Rosa, D. A., Dors, O. L., Pastoriza, M. G., Winge, C., Hägele, G. F., Cardaci, M. V., & Rodrigues, I. 2014, *MNRAS*, 437, 1155

Kroupa, P. 2001, *MNRAS*, 322, 231

Krumholz, M. R., Dekel, A., & McKee, C. F. 2012, *ApJ*, 745, 69

Krumholz, M. R., Leroy, A. K., & McKee, C. F. 2011, *ApJ*, 731, 25

Krumholz, M. R., McKee, C. F., & Tumlinson, J. 2009, *ApJ*, 693, 216

Kudritzki, R. P. 2002, *ApJ*, 577, 389

Kunth, D., Mas-Hesse, J. M., Terlevich, E., Terlevich, R., Lequeux, J., & Fall, S. M. 1998, *A&A*, 334, 11

Langer, N. 1998, *A&A*, 329, 551

Larson, R. B., & Tinsley, B. M. 1978, *ApJ*, 219, 46

Lee, H.-W. 2000, *ApJ*, 541, L25

Lee, J. C., Kennicutt, R. C., Funes, José G., S. J., Sakai, S., & Akiyama, S. 2007, *ApJ*, 671, L113

Lee, J. C., Kennicutt, Jr., R. C., Funes, S. J. J. G., Sakai, S., & Akiyama, S. 2009a, *ApJ*, 692, 1305

Lee, K.-S., Giavalisco, M., Conroy, C., Wechsler, R. H., Ferguson, H. C., Somerville, R. S., Dickinson, M. E., & Urry, C. M. 2009b, *ApJ*, 695, 368

Lehner, N., et al. 2013, *ApJ*, 770, 138

Leitet, E., Bergvall, N., Hayes, M., Linné, S., & Zackrisson, E. 2013, *A&A*, 553, A106

Leitherer, C., Ferguson, H. C., Heckman, T. M., & Lowenthal, J. D. 1995, *ApJ*, 454, L19

Leitherer, C., et al. 1999, *ApJS*, 123, 3

Lilly, S. J., Carollo, C. M., Pipino, A., Renzini, A., & Peng, Y. 2013, *ApJ*, 772, 119

Linden, T., Kalogera, V., Sepinsky, J. F., Prestwich, A., Zezas, A., & Gallagher, J. S. 2010, *ApJ*, 725, 1984

López-Sánchez, Á. R., Dopita, M. A., Kewley, L. J., Zahid, H. J., Nicholls, D. C., & Scharwächter, J. 2012a, *MNRAS*, 426, 2630

López-Sánchez, Á. R., Koribalski, B. S., van Eymeren, J., Esteban, C., Kirby, E., Jerjen, H., & Lonsdale, N. 2012b, *MNRAS*, 419, 1051

Lotz, J. M., Jonsson, P., Cox, T. J., & Primack, J. R. 2010a, *MNRAS*, 404, 590

—. 2010b, *MNRAS*, 404, 575

Luo, W., Yang, X., & Zhang, Y. 2014, *ApJ*, 789, L16

Maeder, A. 1987, *A&A*, 178, 159

Malhotra, S., Rhoads, J. E., Finkelstein, S. L., Hathi, N., Nilsson, K., McLinden, E., & Pirzkal, N. 2012, *ApJ*, 750, L36

Mannucci, F., Cresci, G., Maiolino, R., Marconi, A., & Gnerucci, A. 2010, *MNRAS*, 408, 2115

Martín-Manjón, M. L., García-Vargas, M. L., Mollá, M., & Díaz, A. I. 2010, *MNRAS*, 403, 2012

Maseda, M. V., et al. 2014, *ApJ*, 791, 17

Mathis, J. S., Rumpl, W., & Nordsieck, K. H. 1977, *ApJ*, 217, 425

McCray, R., & Kafatos, M. 1987, *ApJ*, 317, 190

McGaugh, S. S. 1991, *ApJ*, 380, 140

McKee, C. F. 1989, *ApJ*, 345, 782

Meier, D. S., Turner, J. L., & Beck, S. C. 2002, *AJ*, 124, 877

Meurer, G. R., Heckman, T. M., Lehnert, M. D., Leitherer, C., & Lowenthal, J. 1997, *AJ*, 114, 54

Mihos, J. C., & Hernquist, L. 1994, *ApJ*, 431, L9

Mirabel, I. F., & Sanders, D. B. 1988, *ApJ*, 335, 104

Mitra, S., Ferrara, A., & Choudhury, T. R. 2013, *MNRAS*, 428, L1

Moran, S. M., et al. 2012, *ApJ*, 745, 66

Motte, F., Andre, P., & Neri, R. 1998, *A&A*, 336, 150

Moustakas, J., Kennicutt, Jr., R. C., Tremonti, C. A., Dale, D. A., Smith, J.-D. T., & Calzetti, D. 2010, *ApJS*, 190, 233

Muñoz, J. A., & Loeb, A. 2011, *ApJ*, 729, 99

Myers, P. C., & Benson, P. J. 1983, *ApJ*, 266, 309

Nakajima, K., & Ouchi, M. 2014, *MNRAS*, 442, 900

Nakajima, K., Ouchi, M., Shimasaku, K., Hashimoto, T., Ono, Y., & Lee, J. C. 2013, *ApJ*, 769, 3

Nestor, D. B., Shapley, A. E., Kornei, K. A., Steidel, C. C., & Siana, B. 2013, *ApJ*, 765, 47

Nestor, D. B., Shapley, A. E., Steidel, C. C., & Siana, B. 2011, *ApJ*, 736, 18

Nidever, D. L., et al. 2013, *ApJ*, 779, L15

Nota, A., Smith, L., Pasquali, A., Clampin, M., & Stroud, M. 1997, *ApJ*, 486, 338

Noterdaeme, P., Petitjean, P., Ledoux, C., & Srianand, R. 2009, *A&A*, 505, 1087

Oey, M. S. 1996, *ApJ*, 467, 666

Oey, M. S., Dopita, M. A., Shields, J. C., & Smith, R. C. 2000, *ApJS*, 128, 511

Oey, M. S., & Kennicutt, Jr., R. C. 1997, *MNRAS*, 291, 827

Oey, M. S., et al. 2007, *ApJ*, 661, 801

Orsi, A., Lacey, C. G., & Baugh, C. M. 2012, *MNRAS*, 425, 87

Osterbrock, D. E., & Ferland, G. J. 2006, Astrophysics of gaseous nebulae and active galactic nuclei

Ostriker, E. C., McKee, C. F., & Leroy, A. K. 2010, *ApJ*, 721, 975

Ostriker, E. C., & Shetty, R. 2011, *ApJ*, 731, 41

Ostriker, J. P., & Peebles, P. J. E. 1973, *ApJ*, 186, 467

Ott, J., Walter, F., Brinks, E., Van Dyk, S. D., Dirsch, B., & Klein, U. 2001, *AJ*, 122, 3070

Overzier, R. A., et al. 2008, *ApJ*, 677, 37

—. 2009, *ApJ*, 706, 203

Parravano, A., & Mantilla, J. C. 1991, *A&A*, 250, 70

Pauldrach, A. W. A., Hoffmann, T. L., & Lennon, M. 2001, *A&A*, 375, 161

Pellegrini, E. W., Oey, M. S., Winkler, P. F., Points, S. D., Smith, R. C., Jaskot, A. E., & Zastrow, J. 2012, *ApJ*, 755, 40

Petrosian, V. 1976, *ApJ*, 209, L1

Phillips, T. G., & Huggins, P. J. 1981, *ApJ*, 251, 533

Powell, L. C., Bournaud, F., Chapon, D., & Teyssier, R. 2013, *MNRAS*, 434, 1028

Prochaska, J. X., Kasen, D., & Rubin, K. 2011, *ApJ*, 734, 24

Prochaska, J. X., & Wolfe, A. M. 2009, *ApJ*, 696, 1543

Quiroga, C., Mikołajewska, J., Brandi, E., Ferrer, O., & García, L. 2002, *A&A*, 387, 139

Razoumov, A. O., & Sommer-Larsen, J. 2010, *ApJ*, 710, 1239

Reynolds, R. J. 1984, *ApJ*, 282, 191

Rich, J. A., Kewley, L. J., & Dopita, M. A. 2014, *ApJ*, 781, L12

Saintonge, A., et al. 2011a, *MNRAS*, 415, 32

—. 2011b, *MNRAS*, 415, 61

—. 2012, *ApJ*, 758, 73

Salpeter, E. E. 1955, *ApJ*, 121, 161

Salzer, J. J., et al. 2000, *AJ*, 120, 80

Salzer, J. J., Jangren, A., Gronwall, C., Werk, J. K., Chomiuk, L. B., Caperton, K. A., Melbourne, J., & McKinstry, K. 2005, *AJ*, 130, 2584

Sánchez Contreras, C., Sahai, R., Gil de Paz, A., & Goodrich, R. 2008, *ApJS*, 179, 166

Sancisi, R., Fraternali, F., Oosterloo, T., & van der Hulst, T. 2008, *A&A Rev.*, 15, 189

Sanders, D. B., Scoville, N. Z., Young, J. S., Soifer, B. T., Schloerb, F. P., Rice, W. L., & Danielson, G. E. 1986, *ApJ*, 305, L45

Sargent, W. L. W., Sancisi, R., & Lo, K. Y. 1983, *ApJ*, 265, 711

Savage, B. D., & Sembach, K. R. 1996, *ARA&A*, 34, 279

Schaerer, D., & Vacca, W. D. 1998, *ApJ*, 497, 618

Schlegel, D. J., Finkbeiner, D. P., & Davis, M. 1998, *ApJ*, 500, 525

Schmidt, M. 1959, *ApJ*, 129, 243

Schruba, A., et al. 2011, *AJ*, 142, 37

Shapley, A. E., Steidel, C. C., Pettini, M., & Adelberger, K. L. 2003, *ApJ*, 588, 65

Shapley, A. E., Steidel, C. C., Pettini, M., Adelberger, K. L., & Erb, D. K. 2006, *ApJ*, 651, 688

Shen, S., Mo, H. J., White, S. D. M., Blanton, M. R., Kauffmann, G., Voges, W., Brinkmann, J., & Csabai, I. 2003, *MNRAS*, 343, 978

Shibuya, T., et al. 2014, *ApJ*, 788, 74

Shim, H., & Chary, R.-R. 2013, *ApJ*, 765, 26

Shirazi, M., & Brinchmann, J. 2012, *MNRAS*, 421, 1043

Siana, B., et al. 2010, *ApJ*, 723, 241

Silk, J. 1997, *ApJ*, 481, 703

Simard, L., Mendel, J. T., Patton, D. R., Ellison, S. L., & McConnachie, A. W. 2011, *ApJS*, 196, 11

Smit, R., et al. 2014, *ApJ*, 784, 58

Smith, L. J., Norris, R. P. F., & Crowther, P. A. 2002, *MNRAS*, 337, 1309

Solomon, P. M., & Sage, L. J. 1988, *ApJ*, 334, 613

Stacey, G. J., Geis, N., Genzel, R., Lugten, J. B., Poglitsch, A., Sternberg, A., & Townes, C. H. 1991, *ApJ*, 373, 423

Stark, D. P., Ellis, R. S., Bunker, A., Bundy, K., Targett, T., Benson, A., & Lacy, M. 2009, *ApJ*, 697, 1493

Steidel, C. C., Pettini, M., & Adelberger, K. L. 2001, *ApJ*, 546, 665

Stil, J. M., & Israel, F. P. 2002, *A&A*, 392, 473

Stinson, G. S., Dalcanton, J. J., Quinn, T., Kaufmann, T., & Wadsley, J. 2007, *ApJ*, 667, 170

Storey, P. J., & Hummer, D. G. 1995, *MNRAS*, 272, 41

Strickland, D. K., & Heckman, T. M. 2009, *ApJ*, 697, 2030

Strickland, D. K., & Stevens, I. R. 1999, *MNRAS*, 306, 43

—. 2000, *MNRAS*, 314, 511

Swaters, R. A., van Albada, T. S., van der Hulst, J. M., & Sancisi, R. 2002, *A&A*, 390, 829

Thompson, T. A., Quataert, E., & Murray, N. 2005, *ApJ*, 630, 167

Thuan, T. X., Bauer, F. E., Papaderos, P., & Izotov, Y. I. 2004, *ApJ*, 606, 213

Thuan, T. X., & Izotov, Y. I. 1997, *ApJ*, 489, 623

—. 2005, *ApJS*, 161, 240

Tielens, A. G. G. M., Meixner, M. M., van der Werf, P. P., Bregman, J., Tauber, J. A., Stutzki, J., & Rank, D. 1993, Science, 262, 86

van de Voort, F., Schaye, J., Booth, C. M., & Dalla Vecchia, C. 2011, *MNRAS*, 415, 2782

Vanzella, E., et al. 2012, *ApJ*, 751, 70

Vanzella, E., Siana, B., Cristiani, S., & Nonino, M. 2010, *MNRAS*, 404, 1672

Vázquez, G. A., & Leitherer, C. 2005, *ApJ*, 621, 695

Verbeke, R., De Rijcke, S., Koleva, M., Cloet-Osselaer, A., Vandenbroucke, B., & Schroyen, J. 2014, *MNRAS*, 442, 1830

Verhamme, A., Dubois, Y., Blaizot, J., Garel, T., Bacon, R., Devriendt, J., Guiderdoni, B., & Slyz, A. 2012, *A&A*, 546, A111

Verhamme, A., Orlitova, I., Schaerer, D., & Hayes, M. 2014, ArXiv e-prints

Verhamme, A., Schaerer, D., & Maselli, A. 2006, *A&A*, 460, 397

Voges, E. S., Oey, M. S., Walterbos, R. A. M., & Wilkinson, T. M. 2008, *AJ*, 135, 1291

Weedman, D. W., Feldman, F. R., Balzano, V. A., Ramsey, L. W., Sramek, R. A., & Wuu, C.-C. 1981, *ApJ*, 248, 105

Weis, K. 2003, *A&A*, 408, 205

Wen, X.-Q., Wu, H., Zhu, Y.-N., Lam, M. I., Wu, C.-J., Wicker, J., Long, R. J., & Zhao, Y.-H. 2014, *MNRAS*, 438, 97

West, A. A., Garcia-Appadoo, D. A., Dalcanton, J. J., Disney, M. J., Rockosi, C. M., Ivezić, Ž., Bentz, M. C., & Brinkmann, J. 2010, *AJ*, 139, 315

Willott, C. J., et al. 2010, *AJ*, 139, 906

Wise, J. H., & Cen, R. 2009, *ApJ*, 693, 984

Wolfe, A. M., Turnshek, D. A., Smith, H. E., & Cohen, R. D. 1986, *ApJS*, 61, 249

Wong, T., & Blitz, L. 2002, *ApJ*, 569, 157

Wood, K., Hill, A. S., Joung, M. R., Mac Low, M.-M., Benjamin, R. A., Haffner, L. M., Reynolds, R. J., & Madsen, G. J. 2010, *ApJ*, 721, 1397

Woods, R. M., Wadsley, J., Couchman, H. M. P., Stinson, G., & Shen, S. 2014, *MNRAS*, 442, 732

Wright, E. L., et al. 2010, *AJ*, 140, 1868

Wyithe, J. S. B., & Loeb, A. 2013, *MNRAS*, 428, 2741

Wyithe, J. S. B., Loeb, A., & Oesch, P. A. 2014, *MNRAS*, 439, 1326

Xilouris, E. M., Byun, Y. I., Kylafis, N. D., Paleologou, E. V., & Papamastorakis, J. 1999, *A&A*, 344, 868

Yoon, S.-C., Langer, N., & Norman, C. 2006, *A&A*, 460, 199

Young, J. S., Kenney, J. D., Tacconi, L., Claussen, M. J., Huang, Y.-L., Tacconi-Garman, L., Xie, S., & Schloerb, F. P. 1986, *ApJ*, 311, L17

Yuan, H. B., Liu, X. W., & Xiang, M. S. 2013, *MNRAS*, 430, 2188

Yun, M. S., Ho, P. T. P., & Lo, K. Y. 1993, *ApJ*, 411, L17

Zastrow, J., Oey, M. S., & Pellegrini, E. W. 2013a, *ApJ*, 769, 94

Zastrow, J., Oey, M. S., Veilleux, S., & McDonald, M. 2013b, *ApJ*, 779, 76

Zastrow, J., Oey, M. S., Veilleux, S., McDonald, M., & Martin, C. L. 2011, *ApJ*, 741, L17

Zhang, W., Li, C., Kauffmann, G., Zou, H., Catinella, B., Shen, S., Guo, Q., & Chang, R. 2009, *MNRAS*, 397, 1243

Zheng, Z., & Miralda-Escudé, J. 2002, *ApJ*, 578, 33

Zheng, Z.-Y., Wang, J.-X., Malhotra, S., Rhoads, J. E., Finkelstein, S. L., & Finkelstein, K. 2014, *MNRAS*, 439, 1101

Zibetti, S., Charlot, S., & Rix, H.-W. 2009, *MNRAS*, 400, 1181